Title

Solar Radiation Transfer Through Semitransparent Scattering Media Across Length Scales

Author

BHANAWAT, ABHINAV

Publication Date

2024

Peer reviewed|Thesis/dissertation

UNIVERSITY OF CALIFORNIA

Los Angeles

Solar Radiation Transfer Through Semitransparent Scattering Media Across Length Scales

A dissertation submitted in partial satisfaction
of the requirements for the degree
Doctor of Philosophy in Mechanical Engineering

by

Abhinav Bhanawat

2024

ABSTRACT OF THE DISSERTATION

Solar Radiation Transfer Through Semitransparent Scattering Media Across Length Scales

by

Abhinav Bhanawat
Doctor of Philosophy in Mechanical Engineering
University of California, Los Angeles, 2024
Professor Laurent G. Pilon, Chair

Depleting fossil fuels and climate change have necessitated development of novel energy technologies for a sustainable future. Many of these technologies involve interaction of solar radiation with scattering particles embedded in an absorbing medium, albeit at different length scales. For example, photoelectrochemical water splitting involves direct conversion of water into H_2 and O_2 gases using semiconductor photoelectrodes exposed to sunlight. However, the gases are released in the form of bubbles of about 1 mm in diameter that scatter the incident light. Moreover, some of the near-infrared radiation is absorbed in the aqueous electrolyte, resulting in optical losses. Similarly, geoengineering entails large-scale modification of Earth's natural systems to reflect enough solar energy to counter the energy imbalance (known as "radiative forcing") caused by greenhouse gases. Notably, microbubbles entrained in ship wakes scatter sunlight, and thus can be harnessed to reflect a significant amount of solar radiation, thereby mitigating global warming. Likewise, radiative cooling is a passive cooling technology that involves radiating heat to the outer space (at 3 K) via thermal emission primarily in the long-wavelength infrared (LWIR) atmospheric transparency window between 8 to 13 µm. Mesoporous aerogels made up of silica nanoparticles around 4 nm in diameter could be promising radiative cooling materials because of their high transmittance ($> 90\%$) in the visible and near-unity LWIR emittance.

This dissertation aims to (i) systematically quantify the optical losses caused by gas

bubbles during photoelectrochemical water splitting, (ii) critically review and validate different radiative transfer models for semitransparent media containing scatterers and use the most accurate model to predict albedo of ship wakes containing microbubbles, and (iii) demonstrate the use of mesoporous silica aerogels as optically transparent radiative cooling materials.

First, state-of-the-art Monte Carlo ray-tracing models were developed to simulate interaction of solar radiation with gas bubbles attached to a large horizontal Si photoelectrode surface as well as with those dispersed in the semitransparent aqueous electrolyte. The optical losses were quantified by comparing the photoelectrode absorptance with and without the presence of bubbles for a wide range of bubble diameters, volume fractions, plume thicknesses, and contact angles. Overall, the results suggested that in order to minimize the optical losses, the bubble departure diameter D should be large, while the bubble volume fraction f_v and plume thickness H should be as small as possible. The effect of bubble contact angle θ_c on the optical losses was explained by identifying three different optical regimes based on the interplay of total internal reflection at the electrolyte/bubble interface and reflection at the bubble/photoelectrode interface. Accordingly, design guidelines were provided, such as using hydrophilic photoelectrodes to minimize the bubble contact surface area coverage and using convection to decrease bubble plume thickness.

Second, the relevant models predicting radiation transfer through semitransparent media containing scatterers were critically reviewed. A new hybrid model was proposed that predicts the effective scattering coefficient and asymmetry factor using the Lorenz–Mie theory and the effective absorption coefficient as the volume-weighted sum of the bubbles and medium absorption coefficients and solves the radiative transfer equation using the Monte Carlo method. Its predictions showed excellent agreement with those by the Monte Carlo ray-tracing method based on geometric optics for a wide range of bubble volume fractions, slab thicknesses, and medium absorption coefficients. For experimental validation, micro-computed X-ray tomography scans were performed on a fused silica sample containing bubbles to retrieve the exact locations, diameters, and total volume fraction of bubbles. Here also, predictions of the hybrid model using the retrieved data agreed well with experimen-

tal measurements of the spectral normal-hemispherical reflectance and transmittance of the sample for wavelengths between 0.4 and 3 µm when silica ranges from weakly absorbing to absorbing. Finally, simulations were performed over solar spectrum throughout the day using hybrid model to predict the albedo of ship wakes containing microbubbles for a wide range of bubble diameters and seafoam thicknesses. The results indicated that albedo as high as 0.9 could be achieved with bubble volume fraction $f_v = 74\%$, diameter $D = 20$ µm, and seafoam thickness $H = 20$ mm.

Lastly, mesoporous aerogels composed of silica nanoparticles and having porosities $\phi =$ 72.5%, 80.9%, or 87.5% and thickness around 1 mm were prepared and characterized for passive radiative cooling applications with or without aluminum substrates. The samples' normal-hemispherical reflectance over the solar spectrum and normal emittance over mid-IR wavelengths were measured experimentally using UV-Visible and FTIR spectrophotometers. Their radiative cooling power was quantified across different aerogel thicknesses by performing spectral simulations using the Transfer Matrix method. Overall, it was found that increasing the porosity of silica aerogels eliminated the characteristic decrease in emittance of silica around 9 µm, enabling significantly larger radiative cooling power.

The dissertation of Abhinav Bhanawat is approved.

Aaswath Pattabhi Raman

Adrienne G. Lavine

Vijay K. Dhir

Laurent G. Pilon, Committee Chair

University of California, Los Angeles

2024

Dedicated to my family for their constant love and support that keeps me going.

Table of Contents

List of Figures

List of Tables

Acknowledgments

First of all, I would like to thank Prof. Laurent Pilon for believing in me and providing me the opportunity to work under his supervision. His constant support and encouragement helped me outdo my own expectations. He was always ready to help, be it personally or professionally, and ensured my well-being. His extensive mentoring, even remotely during COVID, helped me build a great foundation in doing research. I could not have asked for a better guide for my PhD journey. Secondly, I would like to thank Prof. Vijay Dhir, Prof. Adrienne Lavine, and Prof. Aaswath Pattabhi Raman for serving on my doctoral committee.

This work would not have been possible without the extensive help and guidance I received from my colleagues and collaborators. I am thankful to Prof. Keyong Zhu for his help with the Monte Carlo ray-tracing model used in Chapter 2, to Prof. Shili Xu and Mikayla Tamboline for their assistance with the X-ray microcomputed tomography scans used in Chapter 4, to Prof. Daniele Visioni and Dr. Ilaria Quaglia for their guidance on using CESM climate model, and to Prof. Bruce Dunn, Prof. Sarah Tolbert, Dr. Patricia McNeil, Dr. Natalie Kashanchi, and Susan for preparing the silica aerogels used in Chapter 5. I am especially grateful to Dr. Refet Ali Yalcin for all his guidance and help with various codes and simulation tools used in this dissertation.

I thank all my current and former labmates, namely Dr. Eylul Simsek Turan, Dr. Sara Vallejo-Castano, Dr. Matevz Frajnkovic, Dr. Ali Dashti, Dr. Sun Woong Baek, Dr. Jack Hoeniges, Yucheng Zhou, Nicolas Leport, and Thomas Lee. Special shout out to my close friend Ricardo Martinez for all the memories we made hanging out in the lab as well as outside. I am also thankful to Rajesh, Shivam, Arpita, Naarendharan, Aamir, Atharva, and Arpit for making my stay in LA so memorable.

I am also grateful to the Mechanical and Aerospace Engineering department at UCLA for their support via the departmental Graduate Fellowship. This research was supported in part by the National Science Foundation NRT-INFEWS: Integrated Urban Solutions for Food, Energy, and Water Management (Grant No. DGE-1735325). I am also thankful to the National Center of Atmospheric Research's (NCAR) Computational & Information Systems

Laboratory (CISL) for an exploratory award of high performance computing resources that will be used for climate model simulations. This work used computational and storage services associated with the Hoffman2 shared cluster provided by UCLA Institute for Digital Research and Education's Research Technology Group.

I am indebted to my family for their constant love and support. Thank you to Swamiji and Dr. Anil K. Rajvanshi for inspiring me to pursue research. Although I started my PhD journey alone in the US, I am fortunate to be completing it with my lovely wife Riya by my side. Her unconditional love and care inspires me to be my best self. Just a simple conversation with her always simplifies my problems, no matter how hard they seem.

Finally, I am grateful to God for always giving me what I need.

Vita

2014–2018 B.Tech., Mechanical Engineering, Indian Institute of Technology Kanpur, India

2018–2019 M.Tech., Mechanical Engineering, Indian Institute of Technology Kanpur, India

Publications

Bhanawat, A., Zhu, K., and Pilon, L., 2022. How do bubbles affect light absorption in photoelectrodes for solar water splitting?, *Sustainable Energy & Fuels*, 6(3), pp. 910-924.

Bhanawat, A., and Pilon, L., 2023. Light transfer through bubble-filled electrolyte for solar water splitting, *Sustainable Energy & Fuels*, 7(2), pp. 448-460.

Bhanawat, A., Yalcin R.A., Martinez R., and Pilon, L., 2023. Critical review and experimental validation of radiative transfer models for semitransparent media containing large gas bubbles, *Journal of Quantitative Spectroscopy and Radiation Transfer*, 311, pp. 108781.

Martinez R., **Bhanawat, A.**, Yalcin R. A., and Pilon, L., 2024. Rigorous accounting for dependent scattering in thick and concentrated nanoemulsions, *The Journal of Physical Chemistry C*, 128(15), pp. 6419-6430.

Bhanawat, A., Yalcin R. A., Martinez R., and Pilon, L. Dependent scattering in concentrated suspensions of optically hard nanoparticles, *Applied Physics Letters* (under review).

Yalcin R.A., McNeil P.E., **Bhanawat, A.**, Martinez R., Kashanschi G.N., Tolbert S.H.,

Dunn B.S., and Pilon, L. Dependent scattering and fractal microstructure determines ambigel's transparency (under review).

Bhanawat, A., Yalcin R. A., McNeil P.E., Martinez R., Simsek E., Dashti A., Dunn B.S., and Pilon, L. Optically-clear mesoporous silica aerogels for passive radiative cooling, (writing in progress).

Ju S., Kashanschi G.N., **Bhanawat, A.**, Martinez R., Yalcin R.A., Pilon, L., and Tolbert S.H. Passive daytime radiative cooling with aerogels containing silica nanoparticles, (writing in progress).

CHAPTER 1

Introduction

1.1 Motivations

1.1.1 Photoelectrochemical water splitting

Depleting fossil fuels necessitate immediate measures to switch to renewable energy sources to sustain human activities [1]. In this context, solar energy has emerged as the most attractive option to serve the human energy needs given its immense potential compared to other renewable and non-renewable energy resources [2]. However, one of the biggest challenges associated with solar energy is its inherent intermittency. Sunlight is only available during the day, necessitating innovative solutions for energy storage to enable continuous power generation at night. A viable approach to this challenge is to utilize solar energy to produce chemicals fuels, referred to as "solar fuels" [3].

One of the most promising solar fuels is hydrogen gas (H_2) due to its high calorific value, which is more than three times that of gasoline and diesel [4]. In addition, it is a clean fuel as it releases water upon combustion or in catalytic reactions in polymer membrane fuel cells without emitting any harmful greenhouse gases. These features make hydrogen an excellent candidate to replace conventional fossil fuels.

Presently, hydrogen is primarily produced through steam methane reforming, which is a significant source of CO_2 emissions [5]. Photoelectrochemical water splitting represents a cutting-edge technology that uses solar radiation to drive the direct conversion of water into H_2 and O_2 gases. It involves the use of photoactive semiconductors, which upon absorbing photons from sunlight, generate electron-hole pairs that can directly participate in redox

reactions. The hydrogen evolution reaction (HER) takes place at the cathode while the oxygen evolution reaction (OER) takes place at the anode. These redox reactions at the photoelectrode result in the release of gaseous products in the form of bubbles at nucleation sites on the surface of the electrodes [6].

$$\text{Hydrogen evolution reaction (HER): } 4H^+ + 4e^- \longrightarrow 2H_2$$
$$\text{Oxygen evolution reaction (OER): } 2H_2O \longrightarrow O_2 + 4H^+ + 4e^-$$

Photoelectrochemical water splitting is usually achieved by three pathways: photocatalysis (PC), photoelectrochemical cell (PEC cell), and photovoltaic-driven electrocatalysis (PV-EC) [7]. Among these three technologies, PEC cell technology has been identified as the most scalable and economically viable for producing substantial amounts of H_2 gas for commercial applications [7–9]. In fact, the US Department of Energy has set the ultimate target of achieving 25% solar-to-hydrogen (STH) efficiency using concentrated illumination to bring down the cost of H_2 gas generated using PEC cell technology [10]. Such high efficiency requires generating a high photocurrent density in the PEC cell.

A typical PEC cell comprises of a semiconductor photoelectrode and a counter electrode in a two-electrode configuration, separated by an ion-exchange membrane and immersed in an aqueous electrolyte [7]. The photoelectrode is exposed to a flux of photons with energy larger than the band gap of the semiconductor photoelectrode material. Absorption of these photons results in redox reactions at the photoelectrode/electrolyte interface and in the release of gaseous products. The photoelectrode is usually made of PV grade materials such as Si and GaAs, or metal oxides including TiO_2 and $BiVO_4$, and may be used as either anode or cathode [7]. When used as a cathode, H_2 gas is released at its surface, while O2 gas is released at the anode unexposed to light. These gases are released in the form of bubbles at nucleation sites on the surface of the electrodes [6]. The gas bubbles usually remain attached to the electrode surface until they grow sufficiently large for buoyancy to overcome surface tension forces. Then, bubbles detach, rise through the electrolyte, and burst at the electrolyte free surface. However, the generated gas bubbles also scatter the incident light, inevitably causing optical losses [11].

Figure 1.1 presents photographs of typical bubble-covered Si or Pt photocathodes in (a) horizontal [12] or (b) vertical [13] orientations showing significant fraction of the photoelectrode area covered with bubbles. Figure 1.1(a) also indicates that the bubbles are approximately spherical cap-shaped for horizontal orientation. For all photoelectrode orientations, the gas bubbles attached to the photoelectrode surface as well as those dispersed in the electrolyte scatter the incident light, resulting in optical losses.

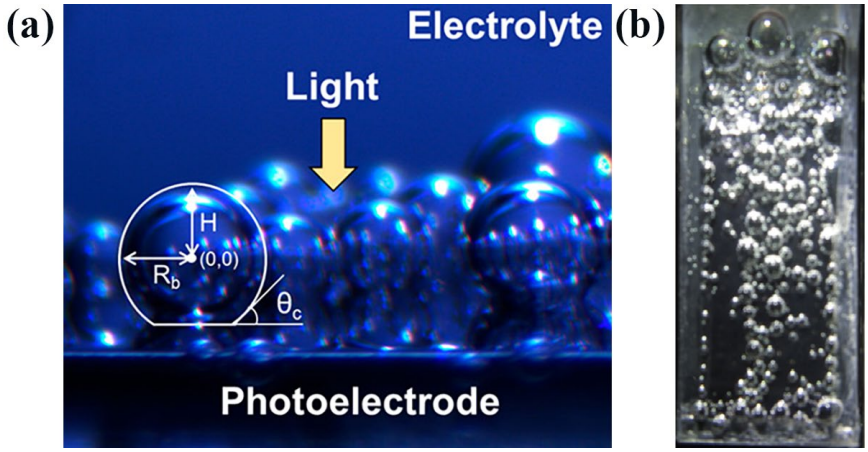

Figure 1.1: (a) Hydrogen gas bubbles obstructing the incident light on a horizontal Si photoelectrode immersed in an aqueous electrolyte (reprinted with permission from Ref. [12]. Copyright © 2017 American Chemical Society). (b) Hydrogen gas bubbles generated on a vertical Pt photoelectrode immersed in an aqueous electrolyte. (reprinted from Ref. [13], Copyright © 2019 with permission from Elsevier).

The optics gets further complicated by light absorption by the aqueous electrolyte for incident radiation of wavelength $\lambda > 900$ nm. Döscher et al. [14] performed "detailed-balance" calculations based on Shockley-Queisser's method [15, 16] to estimate that the theoretical maximum solar-to-hydrogen (STH) conversion efficiency of a tandem PEC cell decreased from 40% to 25% due to sunlight absorption by bubble-free electrolyte of thickness 20 mm. Notably, the absorption losses may further increase due to light scattering by gas bubbles which increases the photon mean free path through the absorbing electrolyte.

Overall, optical losses reduce the photocurrent density generated in the photoelectrode.

Therefore, quantifying these optical losses and identifying key bubble parameters could enable the optimization of PEC cell designs to minimize optical losses and maximize energy conversion efficiency. The latter is of utmost importance for the commercial viability and large-scale deployment of this technology.

1.1.2 Geoengineering

Global warming and climate change demand urgent mitigation measures due to the substantial risk that Earth's temperature will rise more than 1.5 °C above pre-industrial levels by 2050, a critical threshold established by the Intergovernmental Panel on Climate Change (IPCC) [17]. Anthropogenic activities have primarily driven this temperature rise, particularly the emission of greenhouse gases (GHGs) that trap infrared radiation in the atmosphere, preventing the Earth from cooling. Indeed, the amount of CO_2 in the atmosphere has risen from around 200 ppm in 1800s to about 422 ppm in 2024 [18]. In response, various sustainable practices have been proposed and implemented, including the adoption of renewable energy technologies and strategies such as carbon capture and CO_2 sequestration [19]. However, these efforts have not yet yielded significant or immediate results.

In this context, it is crucial to explore alternative measures to address global warming alongside reducing greenhouse gases (GHGs) emissions. Notably, Earth's temperature can also be regulated using solar radiation management via geoengineering techniques. The latter involves large-scale modification of atmospheric phenomena for immediate impact on climate. Several geoengineering approaches have been explored in the literature, including stratospheric aerosol injection and marine cloud brightening [20].

A particularly promising idea is to increase ocean albedo via generating seafoams. Indeed, Figure 1.2 shows that seafoams appear white because of their large reflectance and can effectively reflect sunlight and reduce solar absorption in the ocean. This is particularly significant because 71% of the Earth's surface is covered with water that absorbs a substantial portion of the solar spectrum. Therefore, enhancing the albedo of seafoam could have a considerable impact on global climate. However, generating and sustaining seafoams on a

large scale is a challenge. Large bubbles of the order of 1 mm diameter typically have a lifetime of only a few minutes since they easily rise to the free surface of the ocean and burst [21]. Stabilizing these bubbles would require large amount of surfactants, which could harm marine life. On the other hand, producing smaller bubbles is energetically demanding.

Figure 1.2: Wakes from cargo ships can extend for kilometers and have much higher albedo than bare ocean surface due to light scattering by gas bubbles entrained in the wake (credit: Ryan Hodnett [22]).

In light of these challenges, it is imperative to leverage the existing shipping channels and infrastructure. Indeed, there were over 55000 cargo ships at sea every day in the global shipping lanes, as of 2023 [23]. A typical cargo ship of width 25 to 50 m moving at a speed of about 30 km/h leaves behind a wake that is 50 to 100 m wide and extends for about 10 kilometers [24]. The ship wake albedo is around 0.15, or about three times larger than that of bare ocean surface, due to backscattering of solar radiation by gas bubbles of about 200 micron in diameter entrained in the wake [25]. However, the wakes usually have a very short lifetime of about 15 minutes. Therefore, leveraging ship wakes for geoengineering would first

require accurate simulation of the interaction of solar radiation with seafoam throughout the day to identify the optimal bubble diameter, seafoam thickness, and wake lifetime. Then, the ship wake can be accordingly modified, e.g., by injecting microbubbles to increase wake albedo and/or using natural surfactants to increase bubble lifetime [25].

1.1.3 Radiative cooling

Cooling applications currently account for 15% of the global electricity consumption [26]. This demand is expected to increase to nearly 25% by the end of 2050 due to extreme temperatures resulting from climate change [26]. In this context, daytime radiative cooling has emerged as particularly attractive for passively achieving subambient temperatures. It involves (i) reflecting incident solar energy and (ii) radiating heat to the outer space (at 3 K) via thermal emission primarily in the long-wavelength infrared (LWIR) atmospheric transparency window between 8 to 13 µm [see Figure 1.3].

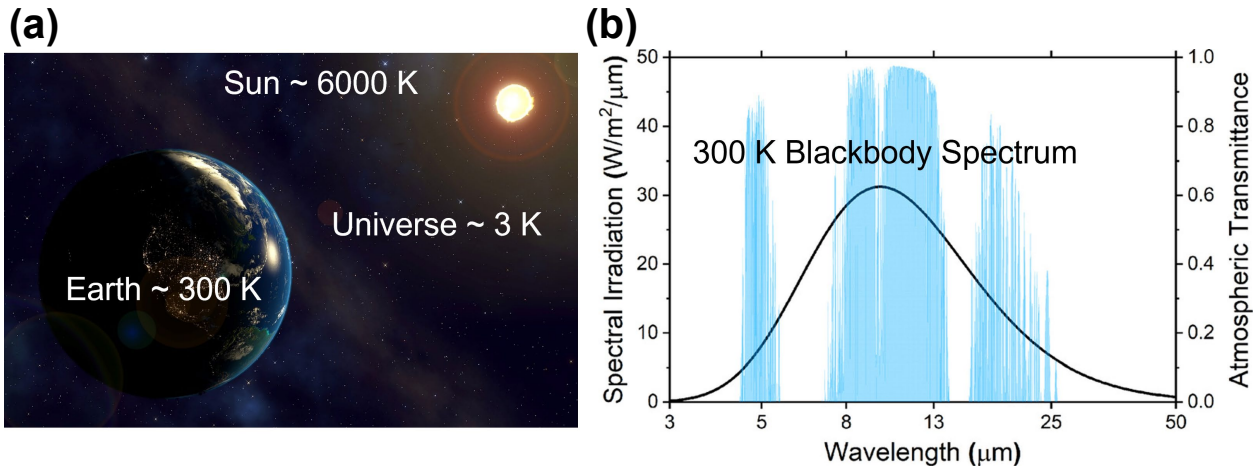

Figure 1.3: (a) The coldness of space can be harnessed for passively cooling objects on Earth via radiative cooling (credit: Kevin M. Gill [22]). (b) The atmospheric transparency window between 8 to 13 µm conicides with the spectral range for peak emissive power for blackbodies around temperature 300 K (reprinted from Ref. [27], with the permission of AIP Publishing).

Raman et al. [28] first demonstrated passive daytime radiative cooling experimentally using a multilayer photonic structure made up of seven layers of HfO_2 and SiO_2 films deposited

on a Ag-coated Si wafer. Their radiative cooling surface achieved a surface temperature 10°C below the ambient temperature under direct sunlight. Since then, many radiative cooling materials have been developed for various applications such as cooling of buildings, water harvesting, and electricity generation [29–31].

A simple daytime radiative cooling surface consists of a spectrally-selective infrared-emitting coating deposited on top of metallic reflector to reflect solar radiation between 0.3 to 2.5 µm [28]. Ideally, the coating should not absorb any solar radiation and should have very high emittance in the atmospheric transparency window. Many radiative cooling surfaces have also been developed that eliminate the need for metallic reflectors by embedding micron-sized scatterers inside high infrared emissivity coatings to reflect sunlight [32].

In addition, many applications such as photovoltaic cells and glazings in buildings utilize solar energy in the visible but need to eliminate the undesirable solar heating [33]. Indeed, the max efficiency of crystalline Si solar cells decreases by 0.45% for every 1 K rise in operating temperature above the ambient [34]. As such, the aging rate of photovoltaic modules doubles for every 10 K rise in their operating temperature [35]. For such applications, the radiative cooling surfaces must be carefully designed to transmit visible solar radiation while selectively emitting in the atmospheric transparent wavelength window of 8-13 µm.

Silica is a popular Earth-abundant coating material for such applications due to its high transparency ($> 95\%$) in the visible and large emittance $\varepsilon > 0.8$ in the mid-infrared wavelengths. However, it also exhibits a significant decrease in emittance at wavelengths λ around 9 - 9.5 µm due to a reflectance peak resulting from the Reststrahlen effect when light interacts with the vibrational modes of the silica lattice [36]. This effect decreases substantially the maximum achievable radiative cooling power for bodies around 300 K that have peak blackbody spectral emissive power around the same wavelength. To address this decrease in emissivity, this dissertation explores the use of mesoporous aerogels made up of silica nanoparticles about 2 nm in diameter. These ambiently-dried aerogel monoliths can be used on top of metallic surfaces for passive daytime radiative cooling applications. Additionally, the aerogels could be used as covers for thermophotovoltaic (TPV) cells, glazings, as well as windows of vehicles to achieve both radiative cooling and visible light transmission.

1.2 Radiation transfer through semitransparent scattering media

In all the aforementioned technologies, solar radiation transfer takes place through a semi-transparent medium containing scatterers, albeit at different length scales. When solar radiation is incident on such a medium, it undergoes several interactions before ultimately getting either reflected back, absorbed, or transmitted. For instance, the radiation may get back-scattered at the surroundings/medium interfaces or get attenuated and absorbed inside the medium. Additionally, the particles embedded inside the medium may scatter the radiation thereby affecting its reflectance, absorptance, and transmittance. In this dissertation, only spherical particles were considered. Therefore, the intensity and angular distribution of scattering depended on (i) the refractive index mismatch between the particles and the surrounding medium and (ii) the particle size parameter $\chi = 2\pi r_p/\lambda$ that compares the radius r_p of the spherical scatterers with the wavelength λ of the incident radiation. The underlying scattering physics varies vastly depending on the size parameter χ, as discussed in the following subsections.

1.2.1 Size parameter $\chi >> 1$ - Geometric scattering

Geometric scattering is governed by the laws of geometric optics and occurs when the size of the scatterer is much larger than the wavelength of the incident radiation. The direction of the refracted or reflected radiation at an interface is given by the Snell's law, defined as [37]

$$n_i sin\theta_i = n_t sin\theta_t, \tag{1.1}$$

where n_i and n_t are the refractive indices of the medium of incidence and transmittance, while θ_i and θ_t are angles of the incident and transmitted radiation measured from the normal.

For unpolarized light, the fraction of energy reflected from an interface, i.e., the reflectivity ρ can be calculated using Fresnel's equation given by [37]

$$\rho = \frac{1}{2}\left[\left(\frac{n_i cos\theta_t - n_t cos\theta_i}{n_i cos\theta_t + n_t cos\theta_i}\right)^2 + \left(\frac{n_i cos\theta_i - n_t cos\theta_t}{n_i cos\theta_i + n_t cos\theta_t}\right)^2\right] \tag{1.2}$$

Then, the transmissivity τ of the interface can be calculated as [37]

$$\tau = 1 - \rho. \tag{1.3}$$

1.2.2 Size parameter $\chi \sim 1$ - Mie scattering

Mie scattering occurs when the size of the scatterer is comparable to the wavelength of the incident radiation, e.g., when sunlight interacts with scatterers such as dust, smoke, and water droplets in clouds. It is described by the Lorenz-Mie theory, which is a full solution of Maxwell's equations for the interaction of a planar wave with a single spherical particle embedded in a non-absorbing medium [37]. Here, the angular distribution of scattering intensity varies strongly with the particle size parameter [37].

1.2.3 Size parameter $\chi << 1$ - Rayleigh scattering

Rayleigh scattering occurs when the scatterer is much smaller than the wavelength of the incident radiation such that the radiation is scattered equally in all directions. Here, the scattering intensity is inversely proportional to the fourth power of incident wavelength [37]. Therefore, shorter wavelengths are scattered much more strongly than longer wavelengths, which is the reason behind many atmospheric phenomena such as the blue color of the daytime sky as well as reddish sky appearance around sunrise and sunset [37].

The three scattering regimes discussed above pertain to the interaction of radiation with a single particle. Typically, host media contain a large number of scatterers. Then, the incident radiation also undergoes multiple scattering whereby the scattered radiation from one particle interacts with other particles. The radiation may also get attenuated if the scatterers and/or the host media are absorbing. All these scattering and/or absorption events have a cumulative effect on radiation transfer.

1.3 Prediction of radiation transfer

Radiation transfer through a semitransparent scattering medium can be simulated accurately by solving Maxwell's equations. However, typical methods such as the superposition T-matrix method [38], the finite difference time domain (FDTD) method [39], and the discrete dipole approximation method [40] require large computational resources and are limited to nanoparticles embedded in suspensions of thickness on the same order of magnitude as the wavelength of interest [41].

Radiation transfer can also be simulated with high accuracy using the Monte Carlo ray-tracing (MCRT) method when geometric optics is valid [37, 42]. The MCRT is a stochastic simulation method that traces millions of photon bundles or "rays" along their path in the computational domain as they undergo specular reflection or refraction at the bubble/medium or medium/surrounding interfaces according to Snell's law and Fresnel's equations [37]. The computational domain can be generated numerically by randomly distributing polydisperse particles in a semitransparent medium following an arbitrary size distribution. Alternatively, the location and size distribution of the bubbles can be experimentally determined by performing a microcomputed X-ray tomography (microCT) scan of an actual sample containing those particles. Finally, periodic boundary conditions (BCs) can be used such that the rays reaching one edge of the computational domain re-enter the domain from the opposite edge maintaining their original direction. When the periodic BCs are eliminated, the rays reaching the edges of the medium undergo reflection/refraction at the medium/surrounding interface. The reflected rays are then traced on their onward path, while the refracted rays are considered as lost. Overall, each ray is traced until it is transmitted or reflected from the domain or absorbed in the semitransparent medium or lost from the edges. A sufficiently large number of rays (on the order of 10^6) is necessary to obtain numerically converged predictions of transmittance, reflectance, and absorptance [43, 44]. However, the MCRT method is also computationally intensive and requires development of customized models.

Conventionally, the 1D radiative transfer equation (RTE) is solved to predict the re-

flectance and transmittance of an absorbing, scattering, and non-emitting medium [45–47]. The one-dimensional steady-state RTE is expressed as [37]

$$\mu \frac{\partial I_\lambda(z,\theta)}{\partial z} = -(\kappa_\lambda + \sigma_{s,\lambda}) I_\lambda(z,\theta) + \frac{\sigma_{s,\lambda}}{2} \int_{-1}^{1} I_\lambda(z,\theta')\, \Phi_\lambda(\theta',\theta) d\mu', \tag{1.4}$$

where $I_\lambda(z,\theta)$ is the spectral radiation intensity at location z and in direction $\mu = \cos\theta$, and the effective spectral radiation characteristics of the heterogeneous medium treated as homogeneous include the effective scattering coefficient $\sigma_{s,\lambda}$, the absorption coefficient κ_λ, and the effective scattering phase function $\Phi_\lambda(\theta',\theta)$. The latter corresponds to the probability of a photon incident from direction $\mu' = \cos\theta'$ being scattered in the direction of interest $\mu = \cos\theta$. Usually, these radiation characteristics are determined using a combination of Lorenz-Mie theory and superposition principle for an ensemble of particles, assuming the bubbles scatter independently of each other [37]. This methodology can be used for a wide range of particle size parameters. However, it cannot be used to determine the effective radiation characteristics when the host medium containing scatterers is semitransparent because the Lorenz-Mie theory is based on the assumption that the host medium is non-absorbing. Additionally, assuming heterogeneous media as homogeneous limits the accuracy of RTE when properties change abruptly, especially near the boundaries of the medium. As such, the RTE cannot be used to predict radiation transfer through configurations such as cap-shaped droplets on top of a windows [48] or bubbles nucleating from substrates subjected to solar radiation [49]. Finally, the RTE cannot account for coherent backscattering at the boundaries of a medium containing very small nanoparticles [41]. In that case, the medium behaves as homogeneous, and its effective refractive and absorption indices are determined using the Maxwell-Garnett effective medium theory [50]. Then, the radiation transfer can be solved using other tools such as the Transfer Matrix method [51].

1.4 Objectives of the present study

This dissertation aims to study the interaction of solar radiation with scatterers of different length scales embedded in semitransparent media for novel climate technology applications, namely, photoelectrochemical water splitting, geoengineering, and radiative cooling.

For large scatterers ($\chi >> \lambda$), the interaction of light with large gas bubbles present on the surface of the photoelectrode as well as in the volume of the semitransparent aqueous electrolyte was studied in order to systematically quantify their effect on the performance of the photoelectrode during photoelectrochemical water splitting. Monte Carlo ray-tracing models were developed to simulate light transfer in the presence of bubbles in order to identify the key parameters affecting optical losses and their relative importance. Accordingly, design guidelines were provided to minimize the optical losses for enhanced system efficiency.

For scatterers of size comparable to the wavelength, i.e., $\chi \sim \lambda$, first, the relevant models predicting radiation transfer through semitransparent host medium containing scatterers were critically reviewed, and their validity was assessed numerically and experimentally. Then, the most accurate model was used to simulate radiation transfer through seafoams in ship wakes containing microbubbles to predict their albedo for a wide range of bubble radii and seafoam thickness.

For scatterers much smaller than the wavelength, i.e., $\chi << \lambda$, mesoporous aerogels composed of silica nanoparticles were studied for passive daytime radiative cooling applications. First, simulations were performed using the Transfer Matrix method [51] for design optimization. Then, the aerogels were prepared and characterized using UV-Visible and FTIR spectrophotometers. Finally, their radiative cooling power and long-wavelength infrared (LWIR) emissivity were quantified and compared with other radiative cooling surfaces reported in literature.

1.5 Organization of the document

Chapters 2 and 3 correspond to large gas bubbles exhibiting geometric scattering for applications in photoelectrochemistry. Chapter 2 quantifies the effect of bubbles attached to the photoelectrode surface on the optical losses in photoelectrochemical water splitting. Chapter 3 computes the optical losses due to the presence of bubbles randomly dispersed in the electrolyte volume and assesses their impact on photoelectrode performance. Chapters 4 studies Mie scattering by gas bubbles embedded in a semitransparent medium. It critically

reviews and assesses numerically and experimentally the validity of different numerical models predicting radiation transfer through semitransparent media containing scatterers. It also quantifies the achievable albedo enhancement in ship wakes with the use of microbubbles and identifies the required bubble size and foam thickness for the same. Chapter 5 studies the efficacy of mesoporous aerogels composed of silica nanoparticles for daytime radiative cooling applications. Chapter 6 presents conclusions of the dissertation and discusses potential future work. Figure 1.4 summarizes the organization of the dissertation in terms of the different scattering regimes, their corresponding applications, and the methods of solution.

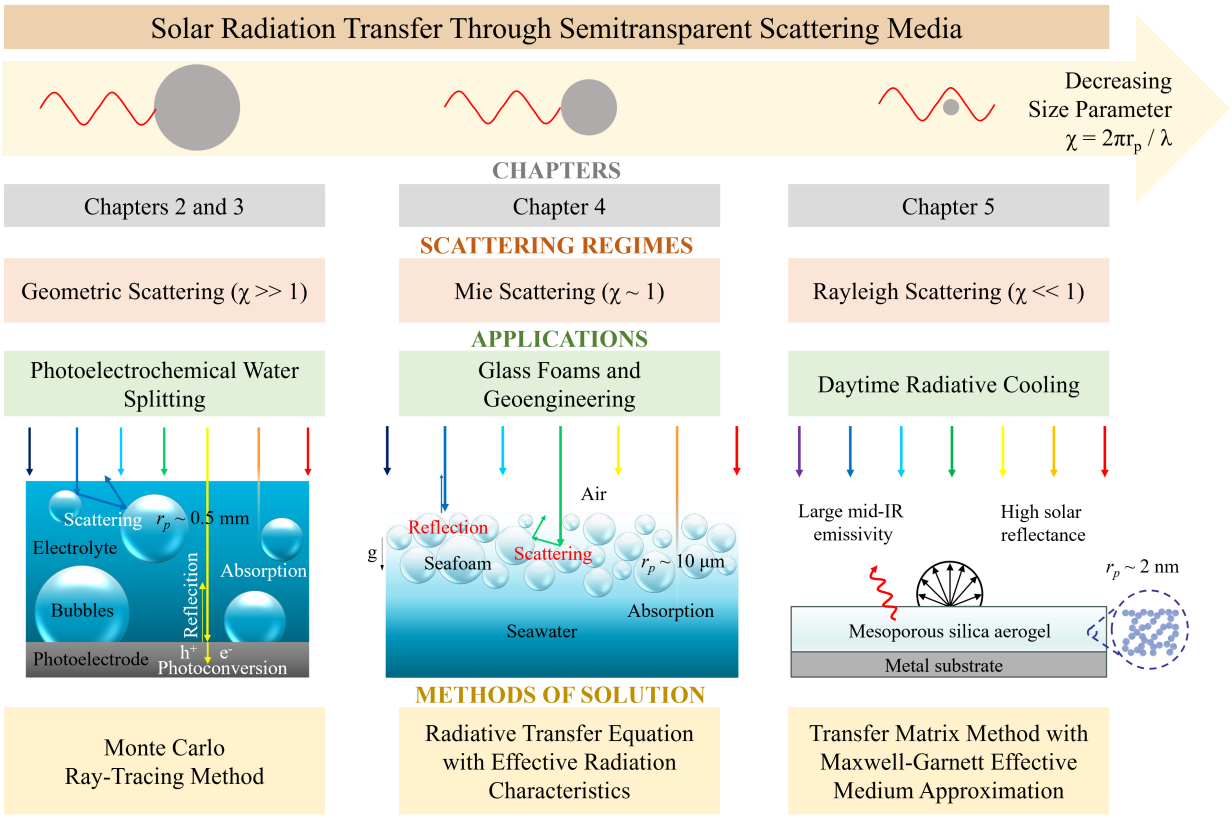

Figure 1.4: Organization of this dissertation.

CHAPTER 2

Effect of surface-attached bubbles on the performance of photoelectrodes for solar water spliting

This chapter systematically investigates the effect of gas bubble formation on the performance of a horizontal photoelectrode exposed to normally incident light during photoelectrochemical water splitting. The presence of hydrogen or oxygen gas bubbles on photoelectrode surface increases the back-scattering losses from the photoelectrode, thereby decreasing the photocurrent density generated. To quantify these optical losses, the normal-hemispherical reflectance of a Si photoelectrode covered with non-absorbing cap-shaped gas bubbles was predicted using the Monte Carlo ray-tracing method. The light absorption by a bare photoelectrode without bubbles served as a reference. For the first time, results are reported for both monodisperse and polydisperse bubbles with diameter ranging between 0.25 and 1.75 mm, projected surface area coverage varying between 0 and 78.5%, and contact angle ranging between 0°and 180°. The normal-hemispherical reflectance of the photoelectrode was found to be independent of the bubble diameter, and spatial and size distribution for any given projected surface area coverage. However, it varied significantly with the bubble contact angle due to total internal reflection at the electrolyte/bubble interface. The normal-hemispherical reflectance also increased with increasing projected surface area coverage thereby reducing the photon flux absorbed in the photoelectrode. In fact, the photons were absorbed mostly outside the bubble projection where they were preferentially scattered by the bubbles. The area-averaged absorptance in a bubble-covered Si photoelectrode reduced by up to 18% compared with a bare photoelectrode. The results presented in this study indicate that the performance of large photoelectrodes can be improved by using hydrophilic photoelectrodes or coatings.

2.1 Background

Very few studies have analyzed the optical effects of bubbles on the performance of vertical or horizontal photoelectrodes [1,12,13,52,53]. Holmes-Gentle et al. [52] conducted experiments to study the optical losses due to a rising plume of O_2 gas bubbles evolving from a transparent vertical electrode consisting of a glass slide of surface area 15×15 mm^2 coated with fluorine-doped tin oxide (FTO) and immersed in an aqueous solution of 1 M NaOH. Collimated light was incident normally onto the electrode surface and its normal-hemispherical transmittance was recorded in the presence of bubbles using an integrating sphere. Then, the optical losses due to back-scattering from the bubble-covered electrode were calculated using the recorded transmittance since the electrode and electrolyte were non-absorbing. The average diameter of bubbles in the plume was about 45 μm. Optical losses up to 5% were reported due to scattering by the bubbles. Some of the strategies proposed to mitigate scattering losses included evolving fewer but larger bubbles and removing bubbles faster by flowing the electrolyte.

Njoka et al. [13] characterized the behavior of O_2 and H_2 gas bubbles on the surface of vertically-oriented Pt photoelectrodes by capturing macroscopic images to understand their effect on the performance of a tandem photoelectrochemical cell subject to normally incident radiation. The authors observed that H_2 bubbles tended to grow independently from one another, remained attached to the photoelectrode, and accumulated at its surface for longer periods of time compared to O_2 bubbles which tended to coalesce and rise rapidly. They reported that the size of bubbles on photoelectrodes was much larger than that on electrodes because of lower photocurrent densities in the photoelectrodes, with average departure diameter of H_2 bubbles about 1.7 mm while that of O_2 bubbles about 1.4 mm at photocurrent density of 9.6 mA/cm^2. Unfortunately, the bubble contact angle and surface area coverage were not reported. Overall, they estimated about 5% loss in the photocurrent density due to the presence of bubbles in a tandem photoelectrochemical cell.

Dorfi et al. [12] studied experimentally the losses in photocurrent density and external quantum efficiency (EQE) due to a single H_2 bubble attached to the surface of an upward-

facing horizontal Si photocathode immersed in 0.5 M H_2SO_4 aqueous electrolyte. The bubble diameter varied from 200 μm to 2 mm while the contact angle of the bubble was either 20°or 50°. The authors used scanning photocurrent microscopy (SPCM) producing line scans of a normally incident laser beam of wavelength 532 nm over the bubble to determine experimentally the local variation of photocurrent density and EQE as compared to that of a Si photoelectrode without bubbles. Then, the experimental results were explained using predictions from a simple optical model based on Snell's law and accounting for bubble curvature but ignoring multiple reflections. The reduction in the photocurrent density caused by the presence of a bubble of diameter $D = 1$ mm reached up to 23%.

More recently, Kempler et al. [53] presented experimental measurements and ray-tracing simulations for the optical and electrochemical effects of H_2 bubbles attached to the surface of upward-facing horizontal 1×1 cm^2 Si photoelectrodes exposed to unpolarized monochromatic light ($\lambda = 630$ nm). They established experimentally that the photocurrent density decreased by up to 10% compared to that in a bare Si photoelectrode when a large fraction of the photoelectrode surface was covered with bubbles and not in direct contact with the electrolyte. Ray-tracing simulations were performed, generating line-scans of photocurrent density for a single bubble and a few equally-spaced monodisperse bubbles for a limited number of bubble contact angles ($\theta_c = 20°$, 60°, and 90°) and contact surface area coverages ($f_S = 0$ to 60%). Smaller bubbles were reported to cause smaller losses in photocurrent density as compared to larger bubbles for the same contact surface area coverage f_S. This was attributed to totally internally reflected rays from larger bubbles being redirected away from the photoelectrode surface. However, line-scan results do not fully capture the envisioned outdoor operation of photoelectrochemical cells where the entire photoelectrode surface and the numerous polydisperse bubbles are irradiated simultaneously.

Most previous studies investigated experimentally the effect of bubbles on the performance of photoelectrodes. They supported their experimental observations with relatively simple ray-tracing simulations considering a single bubble or a few monodisperse bubbles. However, 2.1 shows that in reality, numerous polydisperse bubbles are present on the photoelectrode surface. In addition, discussion of the effect of bubble contact angle on the

optical losses was limited to a small range of contact angles. Indeed, the presence of micro- and nano-structures on the photoelectrode surface can change its wettability and thus the bubble contact angle [54]. In addition, the bubble contact angle may change due to photoinduced hydrophilicity [55] and Marangoni effects due to concentration gradients at the electrolyte/bubble interface [56]. Moreover, for generating sufficient H_2 gas to make the technology commercially viable, the photoelectrode should ideally be of a very large area [53], whereas the photoelectrode areas simulated in most previous studies were at most cm-scale to match the electrode size used in their experiments.

This study aims to comprehensively investigate the optical losses caused by the presence of bubbles on horizontal photoelectrodes immersed in an aqueous electrolyte and exposed to normally incident monochromatic radiation. Monte Carlo ray-tracing method was utilized to predict the local and area-averaged absorptance in the photoelectrode. The simulations faithfully accounted for the interaction of the incident light on an infinitely large photoelectrode surface covered with either ordered or randomly distributed, monodisperse or polydisperse non-absorbing cap-shaped bubbles with a wide range of bubble diameters, contact angles, and projected surface area coverages. The spatial variations of the absorptance and its area-averaged value were systematically compared with those for the reference case of a bare photoelectrode immersed in electrolyte but without bubbles.

2.2 Analysis

2.2.1 Problem Statement

Let us consider a square upward-facing horizontal Si photoelectrode of length L and thickness H immersed in an electrolyte and partially covered with a gas bubble of diameter D, contact angle θ_c, and projected diameter d_p such that $d_p = D$ for $0^\circ \leq \theta_c < 90^\circ$and $d_p = D\sin(180^\circ - \theta_c)$ for $90^\circ \leq \theta_c < 180^\circ$. The bubble/photoelectrode contact circle has a diameter d_c such that $d_c = d_p \sin\theta_c$ for $\theta_c \leq 90^\circ$, and $d_c = d_p$ for $\theta_c > 90^\circ$. The bubble projected surface area coverage f_A represents the fraction of the photoelectrode surface area covered

with bubbles, as encountered by the normally incident photons. We also define the contact surface area coverage f_S as the fraction of the photoelectrode surface area covered by the bubble/photoelectrode interface. For a single bubble of contact angle θ_c and projected diameter d_p covering the photoelectrode surface area $L \times L$, $f_A = \pi d_p^2/4L^2$ and $f_S = \pi d_c^2/4L^2$. The opaque photoelectrode, of refractive and absorption indices n_p and k_p respectively, is immersed in a non-absorbing aqueous electrolyte and is subjected to collimated and normally incident radiation of wavelength λ. Figure 2.1(a) shows the side view of the three-dimensional (3D) computational domain considered in the Monte Carlo ray-tracing simulations. It also shows the diameter d_t of the circle outside which total internal reflection occurs at the electrolyte/bubble interface.

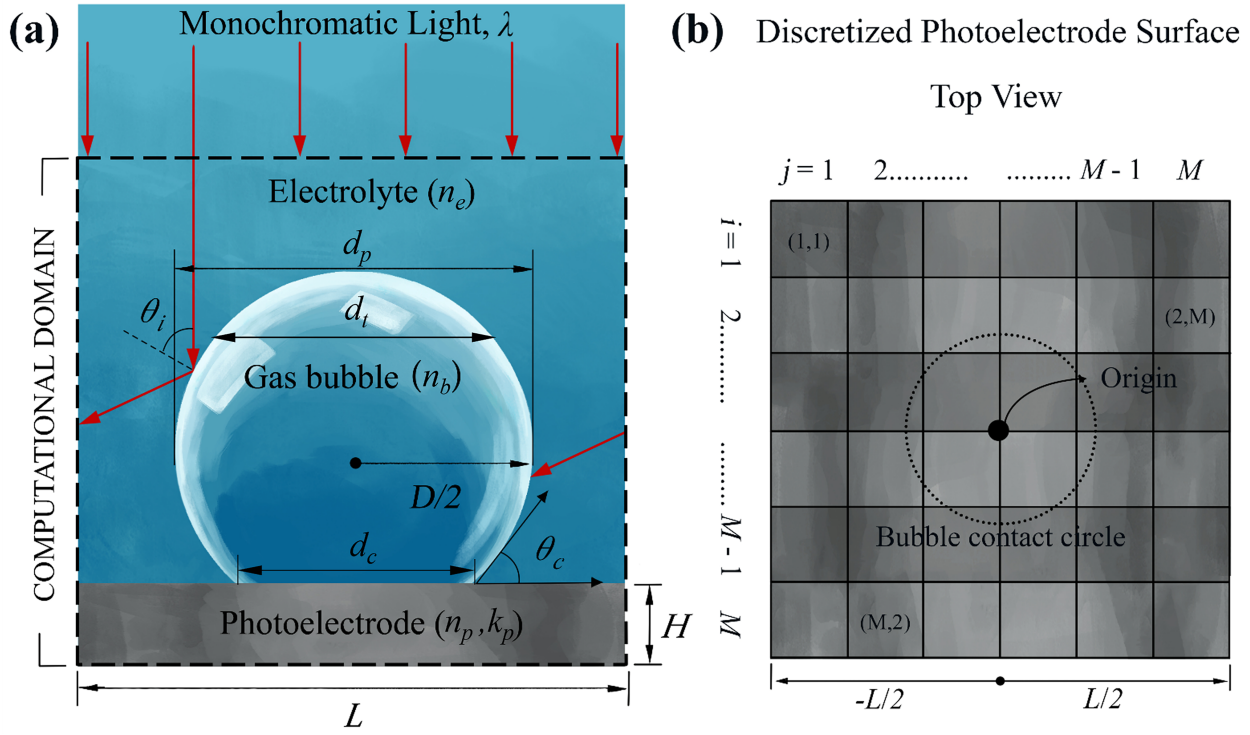

Figure 2.1: (a) 2D cross-section of the 3D computational domain considered in Monte Carlo ray-tracing simulations for an infinite photoelectrode covered with monodisperse bubbles. Scattered photons reaching the sides of the system re-enter from the other side at the same height and travel in the same direction. (b) Photoelectrode surface discretized into $M \times M$ bins for computing the spatial variation of the local absorptance.

2.2.2 Assumptions

To make the problem mathematically trackable, the following assumptions were made : (1) gas bubbles were cap-shaped. (2) Gas bubbles had a constant volume, constant contact angle, and were pinned (no sliding) to the surface of the photoelectrode. (3) Bubbles and electrolyte were non-absorbing with constant refractive indices denoted by n_b and n_e, respectively. (4) All surfaces were optically smooth so that specular reflection and refraction occurred at all interfaces according to Snell's law and Fresnel's equations. (5) Dimensions of the photoelectrode and of the bubbles were much larger than the wavelength λ of the incident radiation so that geometric optics was valid and wave effects could be neglected. (6) The photoelectrode was opaque so that all the photons entering it were absorbed. (7) Photoinduced hydrophilicity effects were neglected.

2.2.3 Modeling

Dorfi et al. [12] presented the following expression for the area-averaged photocurrent density $\bar{J}_{ph}$ (in A/m^2) generated in the photoelectrode immersed in an absorbing electrolyte

$$\bar{J}_{ph} = qIQE\frac{I}{(\frac{hc}{\lambda})}(1 - R_{nh} - A - T_{nh}) \tag{2.1}$$

Here, q is the charge of an electron ($q = 1.60 \times 10^{-}19$ C), IQE is the internal quantum efficiency of the photoelectrode, I is the intensity of the incident radiation (in W/m^2), h is the Planck's constant (m^2 kg/s), c is the speed of light in vacuum (in m/s), λ is the wavelength of the incident radiation (in m), A is the fraction of the incident radiation lost due to absorption in the electrolyte before reaching the photoelectrode, and R_{nh} and T_{nh} are the normal-hemispherical reflectance and transmittance of the photoelectrode immersed in the electrolyte with or without bubbles. However, Equation (2.1) seems erroneous. Indeed, for an absorbing electrolyte, the intensity of the radiation reaching the photoelectrode surface is $I(1 - A)$, a fraction of which is reflected or transmitted by the photoelectrode and is not converted into charge carriers in the photoelectrode. Therefore, the area-averaged photocurrent density $\bar{J}_{ph}$ when the electrolyte is partially absorbing the incident radiation should be

expressed as

$$\bar{J_{ph}} = qIQE\frac{I}{(\frac{hc}{\lambda})}(1-A)(1-R_{nh}-T_{nh}). \tag{2.2}$$

In addition, this expression assumes that the internal quantum efficiency IQE is the same at the bubble/photoelectrode interface and at the electrolyte/photoelectrode interface. However, among all the photons absorbed by the photoelectrode, those absorbed inside the bubble contact surface area may not all contribute to the photocurrent due to the absence of semiconductor-liquid junction where band-bending helps separate the generated charge carriers.

In the present study, the electrolyte is non-absorbing and the photoelectrode is opaque so that $A = 0$ and $T_{nh} = 0$. Therefore, optical losses were only caused by back-scattering at various interfaces and quantified by the normal-hemispherical reflectance R_{nh} of the bubble-covered photoelectrode. An area-averaged absorptance $\bar{A}$ of the photoelectrode can be defined as

$$\bar{A} = 1 - R_{nh} = N_a/N_i, \tag{2.3}$$

where N_i is the number of incident photons at wavelength λ and N_a is the number of photons absorbed in the photoelectrode. The absorptance for a photoelectrode without bubbles, with all other conditions remaining the same, is uniform over the photoelectrode surface, i.e., $\bar{A} = A_0$ which can be written as

$$A_0 = 1 - R_{nh,0} = N_{a,0}/N_i, \tag{2.4}$$

where $N_{a,0}$ is the number of photons absorbed and $R_{nh,0}$ is the normal-hemispherical reflectance of the photoelectrode immersed in the electrolyte given by [37, 42]

$$\rho_{ij} = \frac{(n_p - n_e)^2 + k_p^2}{(n_p + n_e)^2 + k_p^2}. \tag{2.5}$$

Here n_p and n_e are, respectively, the refractive indices of the photoelectrode and the transparent electrolyte while k_p is the absorption index of the photoelectrode. The area-averaged absorptance normalized by the absorptance of the bare photoelectrode A_0 can be used to assess the optical losses caused by the presence of bubbles and defined as

$$\frac{\bar{A}}{A_0} = \frac{1 - R_{nh}}{1 - R_{nh,0}}. \tag{2.6}$$

Equation (2.6) indicates that the normalized area-averaged absorptance depends only on the normal-hemispherical reflectance R_{nh} of the photoelectrode.

Moreover, the presence of bubbles causes spatial variations in the photon flux absorbed in the photoelectrode. To determine the local absorptance, the photoelectrode surface was discretized into $M \times M$ square bins, as illustrated in Figure 2.1(b). The location of each bin was identified by the (x, y) coordinates of its center, with the center of the photoelectrode surface serving as the origin (0,0). By analogy with Equation (**??**), the local absorptance $A(x, y)$ generated in the bin at location (x, y) can be expressed as

$$A(x, y) = N_a(x, y)/N_i, \tag{2.7}$$

where $N_a(x, y)$ is the number of photons locally absorbed in the bin located at (x, y). The number $N_a(x, y)$ varied spatially from one bin to another due to redistribution of the incident radiation on the photoelectrode surface owing to scattering by the bubbles, and because of difference in the reflectances of the electrolyte/photoelectrode and bubble/photoelectrode interfaces. In the absence of bubbles, the number of photons absorbed is the same in all bins and equal to $N_{a,0} = N_i(1 - R_{nh,0})$. Then, the normalized local absorptance $A(x, y)/A_0 = N_a(x, y)/N_{a,0}$ represents the factor by which the local photon absorption is affected by the presence of bubbles.

2.2.4 Method of solution: Monte Carlo Ray-Tracing Method

The Monte Carlo ray-tracing method [37,42] was utilized to predict the normal-hemispherical reflectance R_{nh} and the local absorptance in an opaque photoelectrode immersed in a non-absorbing electrolyte and supporting gas bubbles on its top and subjected to normally incident monochromatic radiation. A step-by-step explanation of the computational procedure was given in our previous studies involving light transfer through a window supporting droplets on its front or back side [43, 44]. Monodisperse or polydisperse cap-shaped bubbles were generated and Snell's law and Fresnel coefficients were calculated at the electrolyte/bubble, bubble/photoelectrode, and electrolyte/photoelectrode interfaces by using a similar methodology as that used in our previous studies [43, 44]. Figure 2(a) illustrates

the working of periodic boundary conditions such that photons reaching the sides of the computational domain re-enter from the opposite side at the same height and in the same direction. Such boundary conditions enable us to quantify the optical losses due to back-scattering of the incident photons by an infinitely large photoelectrode surface covered with bubbles. These losses can be characterized by the normal-hemispherical reflectance R_nh of the bubble-covered photoelectrode, as discussed in the next section. In addition, the performance of the photoelectrode can be compared with and without bubbles based on the local and area-averaged absorptance.

2.2.5 Closure Laws

All simulations were performed using normally incident monochromatic radiation at wavelength $\lambda = 630$ nm. This wavelength was chosen because scaled-up photoelectrochemical water splitting systems are envisioned to be driven by visible light [7]. The refractive index of the aqueous electrolyte solution was assumed to be that of water in the visible, i.e., $n_e = 1.33$ [53]. Similarly, the refractive index of non-absorbing gas bubbles (H_2 or O_2) was assumed to be the same as that of vacuum, i.e., $n_b = 1.0$ [53]. In this study, crystalline Si was considered as the photoelectrode because of its relatively low bandgap, low cost, and abundance [7]. Its refractive and absorption indices at $\lambda = 630$ nm were taken as $n_p = 3.88$ and $k_p = 0.016$ [53].

The bubble diameter D was varied between 0.25 and 1.75 mm based on experimental results reported in Ref. [12]. The projected surface area coverage f_A was varied between 0 and 78.5% (i.e.,$\pi/4$) corresponding to the maximum possible value for monodisperse bubbles attached to the surface of a square photoelectrode. The contact angle θ_c was varied between 0°and 180°in increments of 15°to gain insights into the effects of surface wettability. For polydisperse bubbles, a normal distribution $f(D)$ of bubble diameter was assumed with a mean value of $\bar{D} = 1$ mm and standard deviation $\sigma = 0.25$ mm, and the length of the square photoelectrode was $L = 10$ mm with periodic boundary conditions. For monodisperse bubbles, different bubble diameters $D = 0.5$, 1, or 1.5 mm were considered and the

photoelectrode length L was adjusted to achieve the desired value of projected surface area coverage f_A. In order to predict the normalized local absorptance $A(x,y)/A_0$ with a good spatial resolution at reasonable computational time, the length of the square photoelectrode was taken as $L = 1$ mm, and the photoelectrode surface was divided into $M \times M$ bins, with $M = 101$. Thus, all the bins were square and approximately 10 μm in length. Normalized local absorptance maps were generated for a single bubble with periodic boundary conditions to simulate monodisperse bubbles. Here, the diameter of the bubble was varied to achieve the desired projected surface area coverage. Finally, all the results reported correspond to a total number of incident photons $N_i = 10^7$ necessary to achieve numerical convergence.

2.3 Results and Discussion

This section presents the effects of (1) bubble diameter D, (2) bubble size distribution $f(D)$, (3) contact angle θ_c, and (4) projected surface area coverage f_A on the normal-hemispherical reflectance R_{nh} and on the local $A(x,y)$ and area-averaged $\bar{A}$ absorptance of a horizontal Si photoelectrode covered with H_2 or O_2 bubbles.

2.3.1 Normal hemispherical reflectance

2.3.1.1 Effect of bubble size, polydispersity and spatial distribution

Figure 2.2(a) plots the normal-hemispherical reflectance R_{nh} as a function of contact angle θ_c for monodisperse bubbles with projected surface area coverage f_A equal to 40% or 78.5% and diameter D equal to 0.5, 1.0, or 1.5 mm. Here, the length of the photoelectrode L was adjusted to achieve the desired projected surface area coverage f_A. It is evident that the bubble diameter D had no effect on the normal-hemispherical reflectance R_{nh} for any given projected surface area coverage f_A and bubble contact angle θ_c. In fact, the reflectance R_{nh} increased systematically with increasing projected surface area coverage f_A for any given contact angle θ_c. However, the bubble contact angle θ_c had a more complex effect on R_{nh}, as discussed later in this study.

Figure 2.2(b) compares the normal-hemispherical reflectance R_{nh} of a photoelectrode surface covered with either ordered monodisperse bubbles (diameter $D = 1$ mm) or randomly distributed polydisperse bubbles (normal size distribution with $\bar{D}$ =1 mm and $\sigma = 0.25$ mm) as a function of bubble contact angle θ_c for projected surface area coverage f_A equals to 20%, 40%, and 60%. The photoelectrode length L was equal to 10 mm. Figure 2.2(b) establishes that the bubble size distribution and their spatial distribution did not have any significant effect on R_{nh} for given values of projected surface area coverage f_A and contact angle θ_c. Similar trends were obtained for non-absorbing droplets on a transparent window [43, 44].

Overall, Figure 2.2 establishes that for a non-absorbing electrolyte, the bubble diameter D and size distribution $f(D)$ had no effect on the normal-hemispherical reflectance R_{nh} of the photoelectrode. Instead, R_{nh} was only dependent on the bubble contact angle θ_c and projected surface area coverage f_A, i.e., $R_{nh} = R_{nh}(f_A, \theta_c)$.

2.3.1.2 Effect of bubble contact angle θ_c

Figure 2.3 presents the normal-hemispherical reflectance R_{nh} as a function of bubble contact angle θ_c for projected surface area coverage f_A ranging from 0% to 78.5%. The reflectance R_{nh} of a bare Si photoelectrode (i.e., f_A= 0 %) immersed in electrolyte and that of a Si photoelectrode covered with a 1 mm thick gas film (i.e., f_A= 100 %) sandwiched between the photoelectrode and the electrolyte are also shown as references. Here again, it is evident that the reflectance R_{nh} increased with increasing projected surface coverage f_A for any given contact angle θ_c due to back-scattering caused by various interfaces. Even though the incident radiation was normal to the photoelectrode surface, the angle of incidence θ_i at the electrolyte/bubble interface - defined from the outward normal to the bubble surface [see Figure 2.1(a)] = varied due to the bubble curvature. In fact, it varied between 0°and 90°for $\theta_c \leq 90$°and between 0°and 180°- θ_c, for $\theta_c > 90$°. According to Snell's law, total internal reflection occurs when the angle of incidence θ_i is such that $\theta_i > \sin^{-1}(n_b/n_e)$ where n_b and n_e are the refractive indices of the gas and the electrolyte, respectively. Since the range of θ_i depends on the bubble contact angle θ_c, total internal reflection occurred when θ_c was

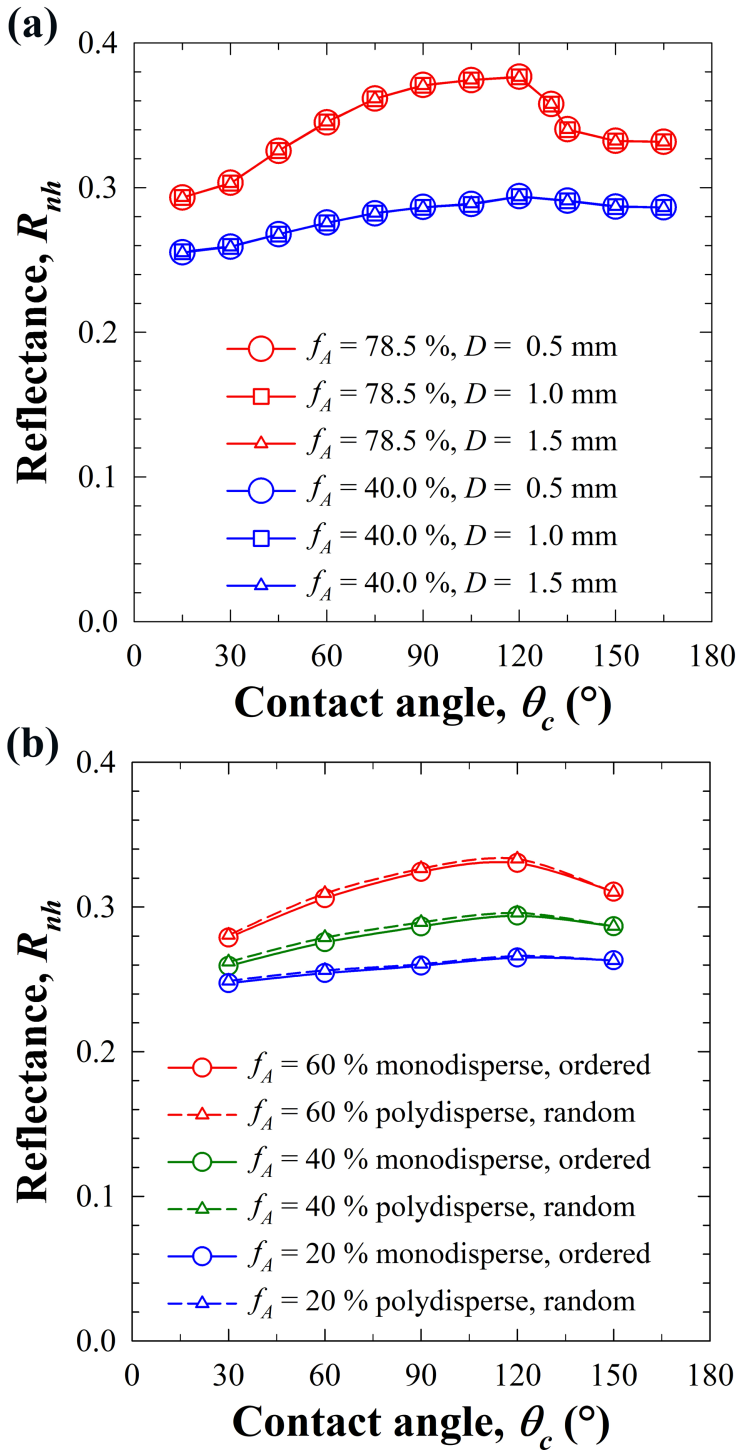

Figure 2.2: (a) Normal-hemispherical reflectance R_{nh} of a photoelectrode covered with bubbles as a function of contact angle θ_c for (a) ordered monodisperse bubbles with different diameter D and projected surface area coverage $f_A = 40\%$ or 78.5%; (b) ordered monodisperse bubbles and randomly distributed polydisperse bubbles with normal distribution with $\bar{D}$ =1 mm and $\sigma = 0.25$ mm for projected surface area coverage $f_A = 20\%$, 40%, or 60%.

smaller than the critical angle for total internal reflection given by

$$\theta_{cr} = 180^\circ - \sin^{-1}(n_b/n_e) = 131.2^\circ \tag{2.8}$$

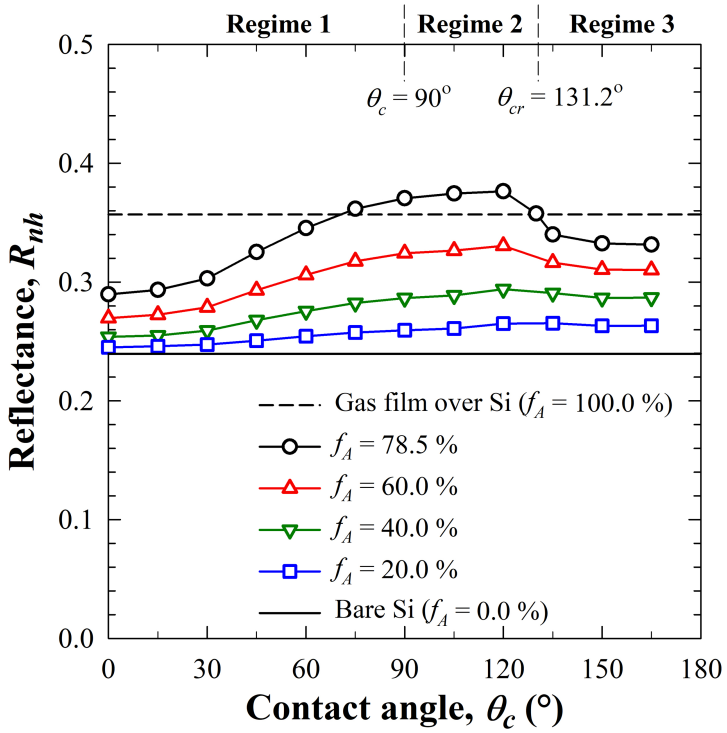

Figure 2.3: Normal-hemispherical reflectance R_{nh} as a function of contact angle θ_c for different projected surface area coverage f_A. The reflectance R_{nh} of a bare Si photoelectrode (i.e., $f_A = 0\%$) immersed in electrolyte, and that of an Si photoelectrode covered with a 1 mm thick gas film (i.e., $f_A = 100\%$) immersed in electrolyte are also shown as references.

In particular, for $\theta_c > \theta_{cr}$, no incident photon was internally reflected at the electrolyte/bubble interface. Thus, for a given projected surface area coverage f_A, three distinct optical regimes can be identified, namely (a) Regime 1 corresponding to contact angles $0^\circ \leq \theta_c < 90^\circ$, (b) Regime 2 with $90^\circ \leq \theta_c < \theta_{cr}$, and (c) Regime 3 such that $\theta_c \geq \theta_{cr}$., as illustrated by the ray-tracing diagrams of Figure 2.4.

Regime 1, $0^\circ \leq \theta_c < 90^\circ$

As θ_c increased from 0°to 90°for a given projected surface area coverage, the contact surface area coverage f_S $(= \frac{\pi d_c^2}{4L^2})$ increased. Therefore, more incident rays reached the bub-

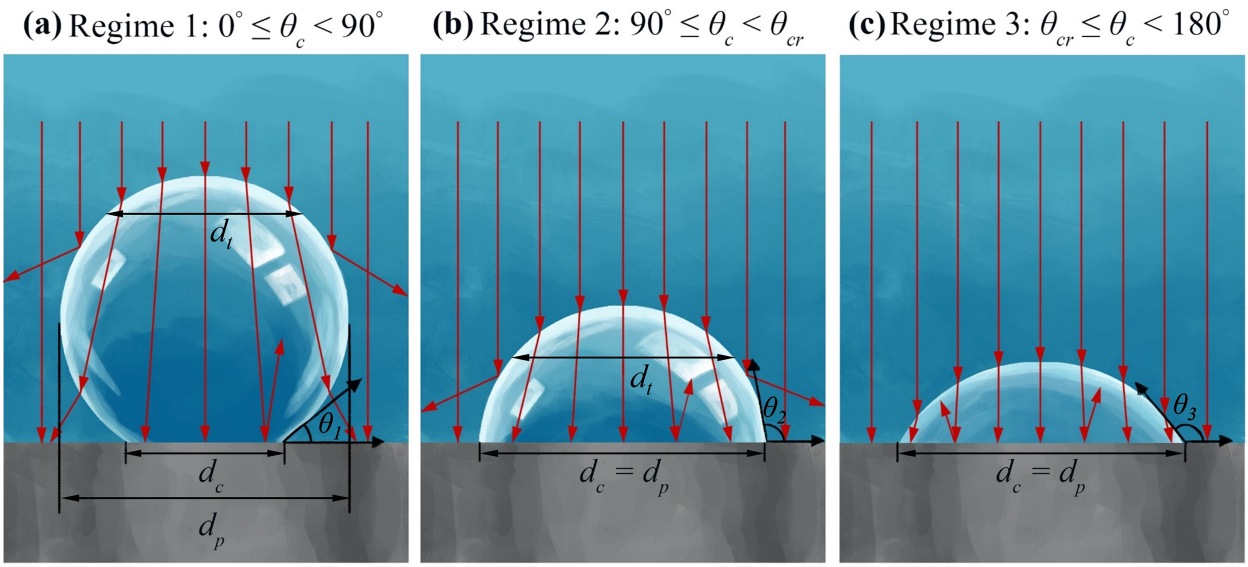

Figure 2.4: Schematic illustrating the change in the contributions from surface area coverage ($=\frac{\pi d_c^2}{4L^2}$) and total internal reflection to the normal hemispherical reflectance R_{nh} based on the contact angle θ_c in (a) Regime 1, (b) Regime 2, and (c) Regime 3.

ble/photoelectrode interface rather than the electrolyte/photoelectrode interface and were more likely to get reflected back due to the large refractive index mismatch. Therefore, in Regime 1, the normal-hemispherical reflectance R_{nh} increased with increasing contact angle θ_c. Also, since $\theta_c < \theta_{cr}$, some of the photons were totally internally reflected at the electrolyte/bubble interface and contributed to the reflectance R_{nh}. However, their contribution did not change significantly with θ_c since the annular region between diameters d_t and d_p inside which total internal reflection occurred remained unchanged in this regime and most of the internally reflected photons were scattered forward [see Figure 2.4(a)] and eventually reached the surface of the photoelectrode regardless of the contact angle.

Regime 2, $90^\circ \le \theta_c < \theta_{cr}$

In Regime 2, the contact surface area coverage f_S was equal to the projected surface area coverage f_A since $d_c = d_p$. However, for a given value of f_A, the annular region between diameters d_t and d_p, in which total internal reflection occurred, decreased as the contact angle θ_c increased due to increase in d_t up to $d_t = d_p$ at contact angle $\theta_c = \theta_{cr}$. Then, fewer photons were totally internally reflected as compared to Regime 1 and more of them were re-

fracted across the bubble/electrolyte interface towards the bubble/photoelectrode interface. Therefore, the contribution of total internal reflection to the reflectance R_{nh} decreased while that of reflection at the bubble/photoelectrode interface increased with increasing contact angle. Thus, the reflectance R_{nh} increased slightly with increasing contact angle up to $\theta_c =$ 120°and then decreased beyond due to negligible contribution from total internal reflection.

Regime 3, $\boldsymbol{\theta_c \geq \theta_{cr}}$

In Regime 3 also, $d_c = d_p$ and $f_S = f_A$ but total internal reflection did not occur at the electrolyte/bubble interface since $\theta_c > \theta_{cr}$ [see Figure 2.4]. Therefore, the normal-hemispherical reflectance R_{nh} was only due to contribution from reflection at the bubble/photoelectrode or electrolyte/photoelectrode interfaces. Thus, R_{nh} dropped off at $\theta_c = \theta_{cr}$, and remained nearly constant beyond, since the contact surface area coverage f_S was constant for a given f_A and the number of photons encountering the bubble/photoelectrode interface remained unchanged with increasing contact angle.

Finally, it is interesting to note that for all projected surface area coverages f_A considered, the magnitude of the normal-hemispherical reflectance R_{nh} at contact angle $\theta_c = 0°$(Regime 1) - when total internal reflection dominated - was smaller than that at $\theta_c = 165°$(Regime 3) when reflection at the bubble/photoelectrode interface dominated. These limiting cases illustrate the interplay between total internal reflection at the electrolyte/bubble interface and reflection at the bubble/photoelectrode interface for a horizontal photoelectrode under normal incidence.

2.3.1.3 Effect of bubble projected area coverage f_A

Figure 2.5 plots the normal-hemispherical reflectance R_{nh} as a function of projected surface area coverage f_A for three different contact angles θ_c equal to 60°, 90°, and 150°corresponding, respectively, to the optical Regimes 1, 2, and 3 described previously. The figure also shows the reflectance $R_{nh,0}$ of a bare photoelectrode immersed in the electrolyte and the reflectance $R_{nh,gf}$ of the photoelectrode in contact with a non-absorbing gas film with the same thickness

as the bubble diameter and given by [37, 42]

$$R_{nh,gf} = \rho_{eb} + \frac{\rho_{bp}(1-\rho_{eb})^2}{1-\rho_{eb}\rho_{bp}}, \tag{2.9}$$

where ρ_{ij} is the reflectance at the optically smooth interface between media i and j under normal incidence, given by [37, 42]

$$\rho_{ij} = \frac{(n_i - n_j)^2 + (k_i - k_j)^2}{(n_i + n_j)^2 + (k_i + k_j)^2}, \tag{2.10}$$

where n_i and n_j are respectively the refractive indices of media i and j, while k_i and k_j are their absorption indices, respectively. The subscripts e, b and p refer to the electrolyte, the bubble, and the photoelectrode, respectively.

In Regimes 1 and 2, R_{nh} increased non-linearly with f_A while in Regime 3, it increased linearly. This can be explained by analyzing the respective contributions of total internal reflection at the electrolyte/bubble interface and reflection at the bubble/photoelectrode interface to the total optical losses. Figure 2.5(b) schematically compares the illumination over a photoelectrode covered with bubble having small or large projected surface area coverage f_A for the same bubble contact angle θ_c in Regime 1 or 2. It illustrates that the losses due to total internal reflection increased with increasing projected surface area coverage f_A. In fact, at low projected surface area coverage f_A, many photons eventually reached the photoelectrode surface after total internal reflection. By contrast, for large projected surface area coverage f_A, many photons were back-scattered upon total internal reflection at the electrolyte/bubble interface. The losses further increased with increasing f_A since the contact surface area coverage f_S increased and more rays encountered the bubble/photoelectrode interface rather than the electrolyte/photoelectrode interface. Therefore, in Regimes 1 and 2, the normal-hemispherical reflectance R_{nh} increased non-linearly with projected surface area coverage f_A. Note that for a projected surface area coverage f_A= 78.5%, the normal-hemispherical reflectance R_{nh} in Regime 2 even surpassed that of a gas film corresponding to f_A= 100%. This can be attributed to the additional back-scattering losses from total internal reflection arising from the bubbles' curvatures.

On the other hand, in Regime 3 for contact angles $\theta_c \geq \theta_{cr}$, total internal reflection was absent and R_{nh} could be approximated as the weighted sum of the reflectances (i) $R_{nh,0}$ of

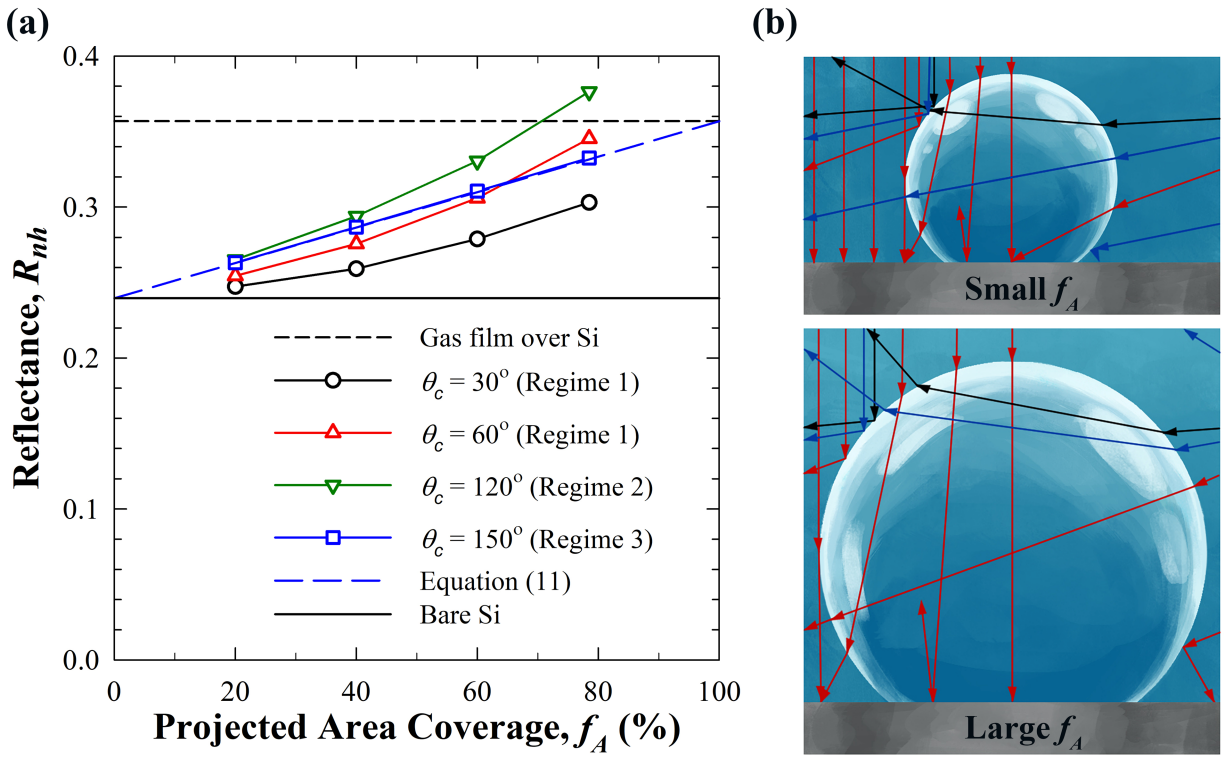

Figure 2.5: (a) Normal-hemispherical reflectance R_{nh} as a function of projected surface area coverage f_A for different contact angles θ_c in Regimes 1, 2, and 3. The reflectance R_{nh} of a bare Si photoelectrode (i.e., $f_A = 0\%$) immersed in electrolyte and that for an Si photoelectrode completely covered with a gas film (i.e., $f_A = 100\%$) and immersed in electrolyte are also shown. (b) Ray-tracing diagrams showing an increase in the total internal reflection losses as f_A increased.

the photoelectrode in contact with the electrolyte [Equation (A.2)] and (ii) $R_{nh,gf}$ of the electrode covered with a gas film [Equation (2.9)], i.e.,

$$R_{nh} = R_{nh,0}(1 - f_A) + R_{nh,gf} f_A \tag{2.11}$$

Figure 2.5(a) establishes that in Regime 3, predictions of the reflectance R_{nh} by Equation (2.11) were in excellent agreement with results from Monte Carlo Ray Tracing simulations.

All the results correspond to situations when bubbles were attached to the surface of the photoelectrode and no bubbles were present in the volume of the electrolyte above the photoelectrode surface. In practice, this situation corresponds to the onset of the photoelectrochemistry and bubble nucleation. At later times, bubbles may be present in the electrolyte volume and may increase the back-scattering losses and affect the direction of rays incident on the photoelectrode surface covered with bubbles. On the other hand, some of the reflected radiation from the bubble-covered photoelectrode surface may also be back-scattered towards the photoelectrode after interaction with the bubbles in the volume. Note, however, that large bubbles in the non-absorbing electrolyte scatter visible light mostly in the forward direction [37, 57]. The overall effect of bubbles in the electrolyte is complicated and its investigation falls beyond the scope of this study.

The results for the normal-hemispherical reflectance R_{nh} can be used to compare the optical losses in a photoelectrode with and without bubbles quantified by the normalized area-averaged absorptance. On the other hand, more detailed simulations are necessary for predicting the normalized local absorptance as discussed in the following sections.

2.3.2 Normalized area-averaged absorptance $\bar{A}/A_0$

Figure 2.6(a) presents the normalized area-averaged absorptance $\bar{A}/\bar{A}_0$ (Equation 2.6) as a function of bubble contact angle θ_c for different projected surface area coverage f_A. It indicates that the optical losses caused by the presence of bubbles can be as high as 18% for f_A= 78.5% and $\theta_c = 120°$. Figure 2.6(a) also establishes that the losses were the smallest for $\theta_c = 0°$for any given surface area coverage f_A. In fact, for contact angle θ_c up to 30°, the optical losses were less than 10% for any considered value of f_A. Therefore, hydrophilic

surfaces should be used to minimize the photocurrent density losses due to back-scattering by the bubbles. For silicon, hydroxyl-terminated Si surfaces have a high wettability, which increase the bubble contact angle θ_c and decrease the contact surface area coverage f_S [53]. The wettability of photoelectrodes can also be controlled by micro/nanostructuring their surfaces [53].

Figure 2.6(b) plots the normalized area-averaged absorptance $\bar{A}/A_0$ as a function of the projected surface area coverage f_A for different contact angles θ_c corresponding to the three different optical Regimes 1 to 3 previously identified. It indicates that optical losses increased with increasing f_A for all values of θ_c considered. In addition, the kinetic and ohmic losses also increase with increasing projected area coverage since the bubble contact surface area coverage increases [6]. The kinetic and ohmic losses are usually estimated in terms of their respective activation and ohmic overpotentials [6]. Typically, the kinetic losses dominate over the ohmic losses at low current densities while the opposite prevails for high current densities [6]. For photoelectrochemical applications, the current densities are usually relatively small and therefore, the ohmic losses are negligible compared with kinetic losses [12]. The kinetic losses are estimated to be between 0 and 2% for bubble contact surface area coverages f_S up to 40% [58]. Increasing the contact surface area coverage also decreases the photoelectrode surface exposed to the electrolyte and available for the redox reactions. Due to this loss of semiconductor-liquid junction, some of the generated charge carriers directly below the bubble contact surface area may not contribute to the photocurrent. Overall, the photoelectrode performance can be improved by reducing the bubble coverage by facilitating the early departure of bubbles from the surface with the help of convection in the electrolyte or the use of surfactants [6, 52, 59, 60].

The results presented in this study show good qualitative agreement with experiments reported in the literature [12, 53]. First, Kempler et al. [53] estimated around 10% loss in the photocurrent density due to substantial gas coverage on the photoelectrode surface with bubble advancing contact angle $> 70°$. These results agree well with the optical loss predictions from our simulations for bubbles with projected surface area coverage $f_A = 60\%$ and the contact angle $\theta_c = 75°$ at the same wavelength of incident radiation. Second, the

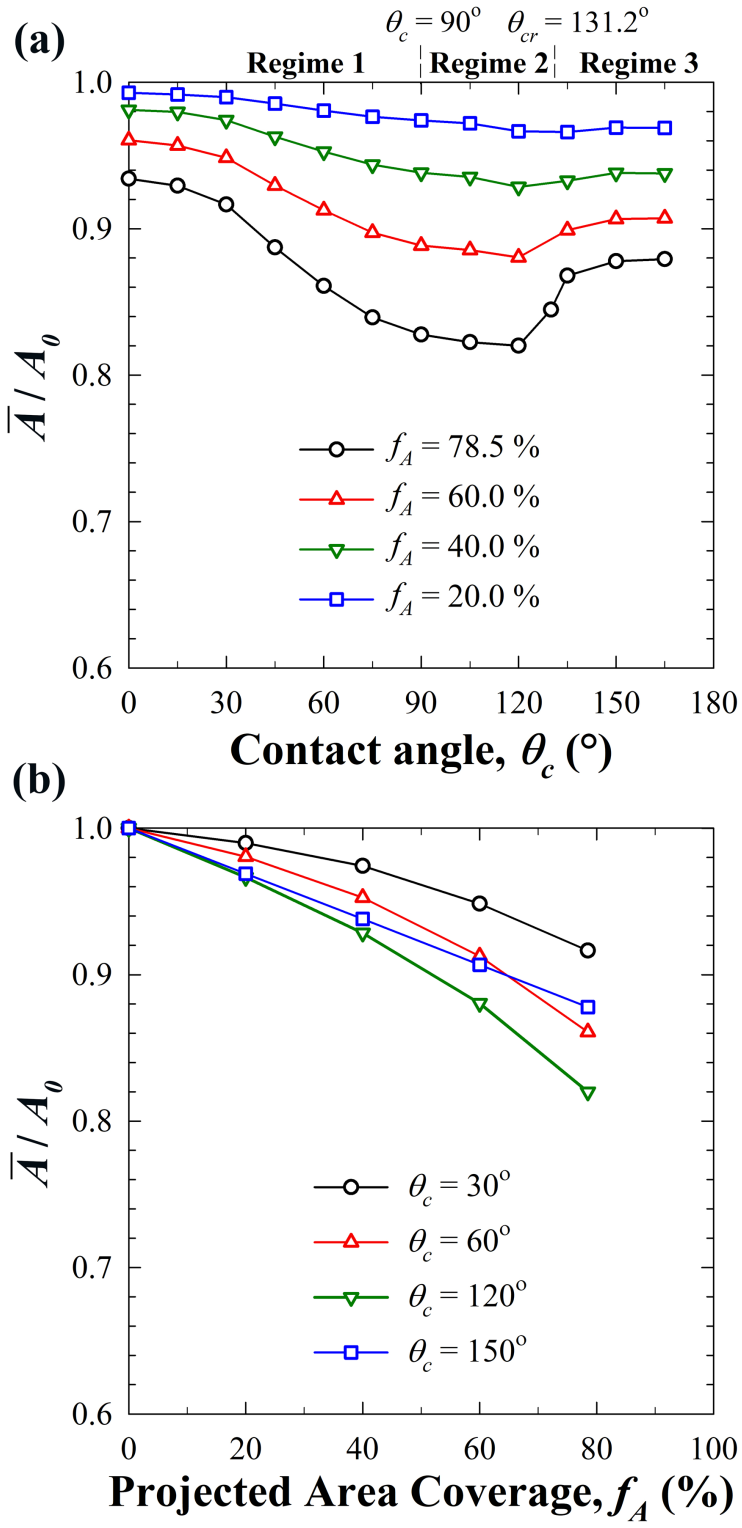

Figure 2.6: Normalized area-averaged absorptance $\bar{A}/A_0$ as a function of (a) the bubble contact angle θ_c for different surface area coverage and (b) the projected surface area coverage f_A for different bubble contact angles corresponding to Regimes 1 to 3.

benefits of using hydrophilic coatings on the surface of the photoelectrode as previously discussed are substantiated by the experimental results from Kempler et al. [53]. On the other hand, our predictions differ from the experimental results by Dorfi et al. [12], who concluded that smaller bubbles were preferable over larger bubbles to minimize optical losses. By contrast, our study demonstrated that the bubble size had no effect on the photoelectrode absorptance for a given projected surface area coverage f_A. However, the bubble projected surface area coverage in the study by Dorfi et al. [12] increased with increasing bubble size. Also, the authors used a small photoelectrode (area = 0.25 cm^2) resulting in optical losses from the edges of the photoelectrode. By contrast, edge effects were negligible for the large photoelectrodes simulated in our study and light scattered by one bubble interacted with neighboring bubbles while keeping the projected area coverage constant; hence the discrepancies.

2.3.3 Normalized local absorptance $A(x, y)/A_0$

Spatial variations in the local absorbed photon flux due to the presence of bubbles can be visualized using the normalized local absorptance map of $A(x, y)/A_0$.

2.3.3.1 Effect of bubble contact angle θ_c

Figure 2.7(a) and 2.7(b) show respectively the side and top views of an upward-facing photoelectrode exposed to normally incident collimated radiation and featuring a gas bubble attached to its surface with a contact angle θ_c. Figure 2.7(b) also shows the x-axis, a centerline CL, and three rings corresponding to (i) the bubble's projected radius $r_p = d_p/2$, (ii) the contact radius r_c of the bubble covering the photoelectrode such that $r_c = d_c/2$, and (iii) the radius r_t of the circle outside which total internal reflection occurs on the bubble, given by $r_t = r_p \sin(180° - \theta_c r)$ where θ_{cr} is given by Equation (2.8). The interaction of the incident photons with interfaces identified by these three rings influenced the spatial distribution of absorbed light intensity in the photoelectrode.

Figure 2.7 shows the normalized local absorptance maps for bubble contact angle (c) $\theta_c =$

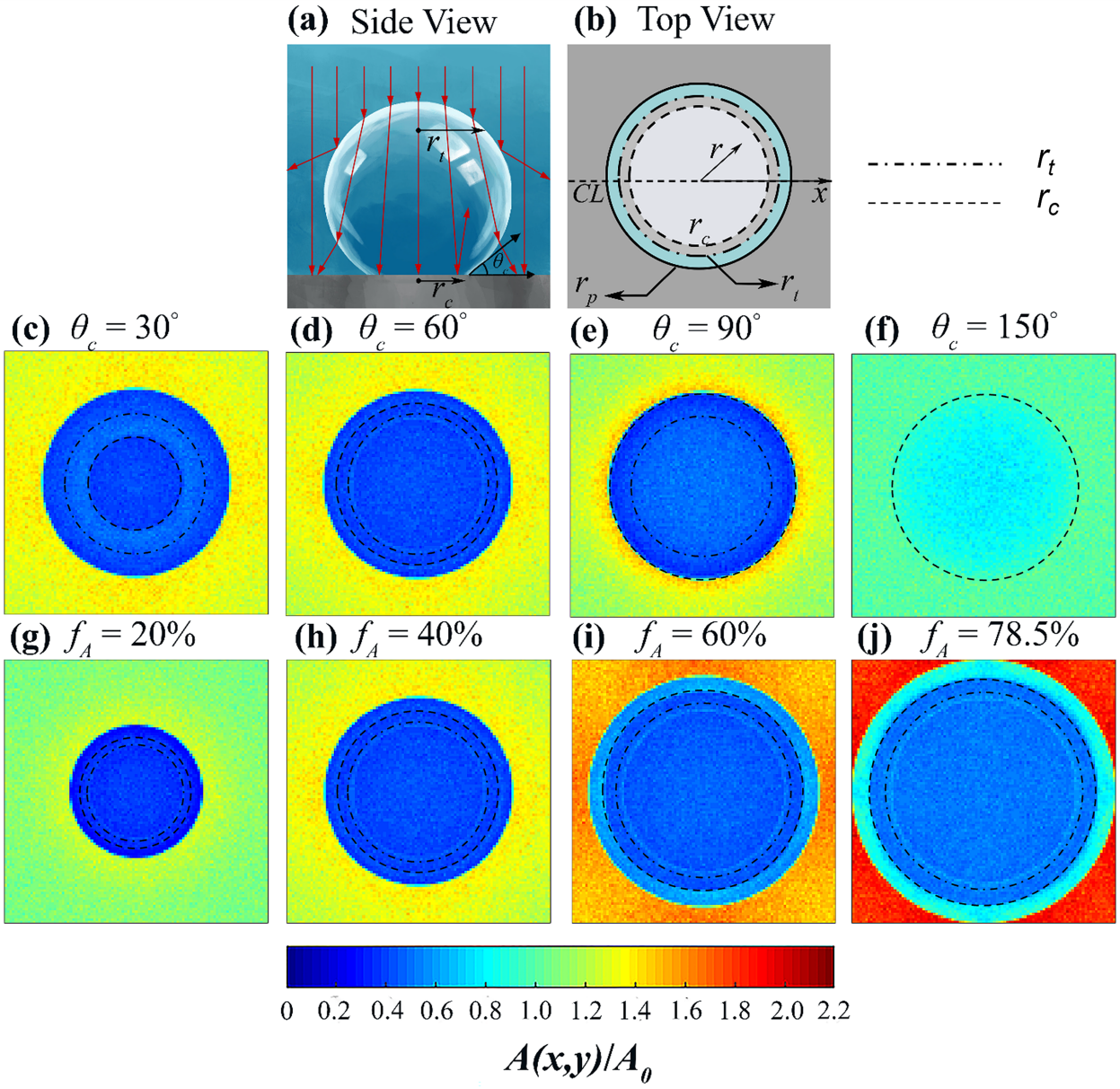

Figure 2.7: (a) Side view of a photoelectrode covered with a bubble. (b) Top view of the photoelectrode surface, showing the x-axis, the centerline CL, and the three rings of radii r_t, r_c, and r_p. Spatial variation of the normalized local absorptance $A(x, y)/A_0$ for contact angle (c) $\theta_c = 30^\circ$, (d) $\theta_c = 60^\circ$, (e) $\theta_c = 90^\circ$, and (f) $\theta_c = 150^\circ$at projected surface area coverage f_A= 40% and for projected surface area coverages (g) f_A= 20%, (h) f_A= 40%, (i) f_A= 60%, and (j) f_A= 78.5% at contact angle $\theta_c = 60^\circ$.

30°, (d) $\theta_c = 60°$, (e) $\theta_c = 90°$, and (f) $\theta_c = 150°$and projected surface area coverage f_A= 40%. As a reference, the normalized local absorptance for a bare photoelectrode submerged in the electrolyte was $A(x, y)/A_0 = 1$. Outside the projected bubble radius r_p, $A(x, y)/A_0$ was larger than 1.0 for bubbles with $\theta_c < \theta_{cr}$ (optical Regimes 1 and 2) due to light concentration after scattering by the bubbles. The thickness of this concentration region shrank as θ_c increased since the photons traveled relatively shorter distance to reach the photoelectrode surface after total internal reflection at the surface of one or more bubbles. The concentration region eventually disappeared for $\theta_c > \theta_{cr}$ when total internal reflection was absent. Inside the disk such that $r < r_p$, the ratio $A(x, y)/A_0$ was less than unity and its spatial variation for different contact angles θ_c can be explained by considering the differences in optics brought about by the change in the relative positions of the rings of radii r_t, r_c, and r_p as well as by the changing bubble contact angle. Figure 2.7(c) shows the results for bubble contact angle θ_c = 30°, where the contact radius r_c was smaller than the radius r_t of the circle outside which total internal reflection prevailed since $\theta_c < 180°$- θ_{cr}. Most of the incident photons in the annular region $r_t \leq$ r $\leq r_p$ were totally internally reflected at the electrolyte/bubble interface while those inside the disk of radius r_t were mostly refracted towards the photoelectrode surface. The photons reaching the photoelectrode surface encountered the bubble/photoelectrode interface inside the disk of radius r_c, leading to $A(x, y)/A_0 < 1$ due to reflection caused by the large refractive index mismatch between the bubble(s) and the photoelectrode. Outside r_c, the photons encountered the electrolyte/photoelectrode interface, where $A(x, y)/A_0 < 1$ in the annular region $r_c \leq$ r $\leq r_p$ due to reduced local photon flux as compared to a bare photoelectrode owing to scattering by the bubbles. Finally, as previously discussed, light concentrated outside the projected bubble radius such that $A(x, y)/A_0 > 1$ for $r > r_p$. These results were typical for contact angles in the range $0 \leq \theta_c \leq 180°$- θ_{cr}, since the relative positions of the three rings remained the same i.e., $r_c < r_t < r_p$. Figure 2.7(d) corresponds to $\theta_c = 60°$, where the radius of the contact circle r_c was greater than the radius r_t since $\theta_c >$ 180°- θ_{cr}. Most of the photons incident in the region $r < r_t$ were refracted and got reflected at the bubble/photoelectrode interface resulting in normalized local absorptance $A(x, y)/A_0$ < 1. In the annular region $r_t \leq$ r $\leq r_p$, $A(x, y)/A_0$ remained less than unity due to reduced

local photon flux owing to total internal reflection. These results were representative of contact angles in the range 180°- $\theta_{cr} \leq \theta_c \leq 90°$. Figure 2.7(e) shows the results for contact angle $\theta_c = 90°$. Here, the contact and projected bubble radii were equal, i.e., $r_c = r_p$ but r_c was larger than r_t, the radius for total internal reflection at the bubble surface. Thus, in the region $r < r_p$, all refracted photons reached the bubble/photoelectrode interface where reflection due to high refractive index mismatch led to $A(x, y)/A_0 < 1$. In the annular region $r_t \leq$ r $\leq r_p$, $A(x, y)/A_0$ decreased further due to the reduction in the local photon flux owing to total internal reflection. These results were typical of contact angles in the optical Regime 2 i.e., $90° \leq \theta_c \leq \theta_{cr}$ as discussed earlier. Finally, Figure 2.7(f) shows that for contact angle $\theta_c = 150°$, the local photon flux was nearly uniform because total internal reflection did not occur at the electrolyte/bubble interface, since $\theta_c > \theta_{cr}$. Here also, $r_c = r_p$ and $A(x, y)/A_0$ was smaller than 1 for $r < r_c$ due to reflection at the bubble/photoelectrode interface. The photons incident outside r_c reached the electrolyte/photoelectrode interface leading to $A(x, y)/A_0 = 1$. These results were representative of all contact angles $\theta_c > \theta_{cr}$ corresponding to the optical Regime 3.

Overall, the results establish that the presence of bubbles caused significant local variation in the absorbed photon flux in the photoelectrode. This variation inside and outside the projected footprint of the bubble was explained by analyzing the different optical phenomena occurring for different bubble contact angles and contact surface area coverages. The absorbed photon flux was concentrated in the rim of the bubble outside the projected radius r_p, while inside, it was always less than that in a bare photoelectrode. The results also indicate that even though hydrophilic surfaces should be preferred to minimize the optical losses, the bubbles generated on such surfaces can scatter the photons far from their incident location. This could potentially be an issue when conducting experiments with small (mm-scale) photoelectrodes due to photons being totally internally reflected away from the photoelectrode. Then, the optical losses will be larger than those predicted in this study.

2.3.3.2 Effect of bubble projected surface area coverage f_A

Figure 2.7 also presents the normalized local absorptance maps $A(x,y)/A_0$ for projected surface area coverage f_A equal to (g) 20%, (h) 40%, (i) 60%, and (j) 78.5% for contact angle $\theta_c = 60°$. It indicates that $A(x,y)/A_0$ became increasingly concentrated (up to a factor of 2) outside the projected footprint of the bubble as f_A increased due to total internal reflection and the increased proximity of the bubbles (see Figure 2.5(b)). Such high local concentration of incident radiation due to scattering from bubbles can lead to corrosion of the photoelectrode, thereby reducing its lifetime [61]. Inside the projected footprint of the bubble, the spatial variation of $A(x,y)/A_0$ can be explained with the help of rings of radii r_c, r_t, and r_p, as discussed earlier for $\theta_c = 60°$and f_A= 40% (Figure 2.7(d)). Overall, $\frac{A(x,y)}{A_0}$ increased at all locations inside the projected footprint of the bubble as f_A increased due to scattered photons from neighboring bubbles ultimately reaching the bubble/photoelectrode interface.

2.3.3.3 Comparison of normalized local absorptance

Figure 2.8 plots the normalized local absorptance $A(x,y)/A_0$ as a function of the normalized location of the center of the bins x/r_p along the centerline CL of the bubble (see Figure 2.7(a)) for (a) contact angles $\theta_c = 30°$, 60°, 90°, and 150°with projected surface area coverage f_A= 40% and for (b) projected surface area coverages f_A= 20%, 40%, 60% and 78.5% with contact angle $\theta_c = 60°$. Figure 2.8(a) shows that for $\theta_c = 30°$, 60°, and 90°, the presence of the bubbles concentrated the local absorptance up to 1.5 times in a region outside the bubble projected diameter. Inside, $A(x,y)/A_0$ decreased sharply to 0.4 and was nearly identical for all contact angles considered. However, no such concentration or sharp drop-off was observed for $\theta_c = 150°$due to the absence of total internal reflection. Note that the spikes observed in the plots were due to the small local variation in the number of incident photons due to random incident locations generated in the Monte Carlo ray-tracing simulations.

Similarly, Figure 2.8(b) compares the magnitude of normalized local absorptance $A(x,y)/A_0$ for different values of f_A. Here, the projected bubble radius r_p increased with increasing f_A

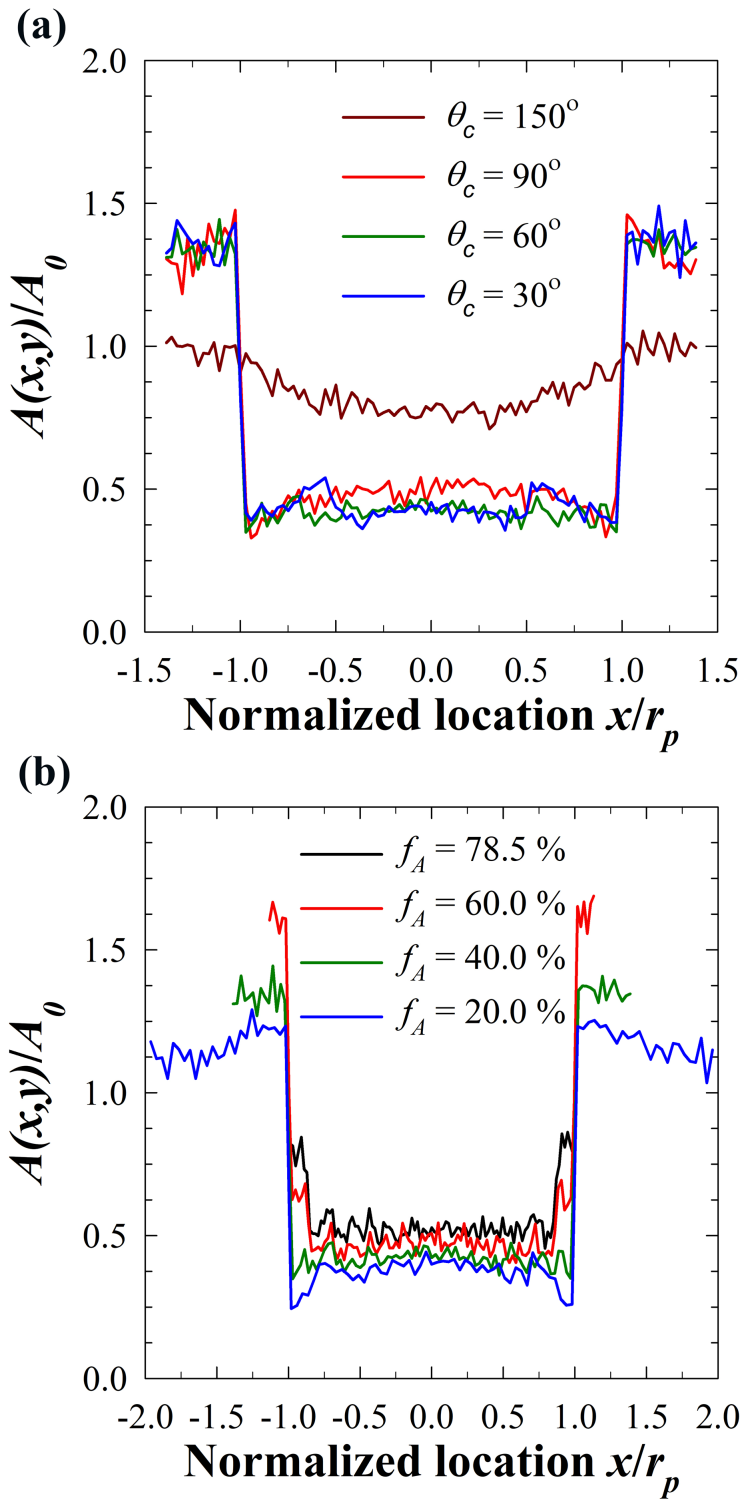

Figure 2.8: Normalized local absorptance $A(x, y)/A_0$ along the centerline of a bubble as a function of normalized location x/r_p for (a) different contact angles θ_c with projected surface area coverage $f_A = 40\%$ and (b) different projected surface area coverages f_A with contact angle $\theta_c = 60^\circ$.

for the same dimensions of the photoelectrode surface. Figure 2.8(b) shows that the magnitude of $A(x, y)/A_0$ increased with f_A both inside and outside the projected footprint of the bubble, as discussed earlier for Figure 2.7(g)- 2.7(j). Note that the spikes observed in the plots were due to the small local variation in the number of incident photons due to random incident locations generated in the Monte Carlo ray-tracing simulations.

2.3.3.4 Comparison of absorption inside and outside bubble contact surface area

Figure 2.9 plots the fraction of incident radiation reflected and absorbed inside or outside the bubble contact surface area as a function of bubble contact angle for different projected surface area coverages (a) $f_A = 20\%$, (b) $f_A = 40\%$, (c) $f_A = 60\%$, and (d) $f_A = 78.5\%$. Figure 2.9 shows that most of the absorption still took place in the photoelectrode area in contact with the electrolyte even for high projected area coverage f_A, provided the contact angle was small. Thus, hydrophilic photoelectrodes with small bubble contact angle are preferable since they ensure that most of the photoelectrode surface area remains in contact with the electrolyte so that the generated charge carriers participate in the water splitting reaction. However, for large projected area coverage f_A, as the contact angle increased, the amount of absorption inside the bubble contact surface area exceeded that outside it. Such a situation is undesirable since most of the generated charge carriers may not be able to participate in the water splitting reaction in the absence of semiconductor-liquid junction. The results presented in Figure 2.9 also have implications in selecting a suitable anti-reflective coating for the photoelectrode surface. Indeed, if the projected surface area coverage and the bubble contact angle are large, it may be appropriate to choose an anti-reflective coating aimed at reducing the reflectance of the bubble/photoelectrode interface rather than that of the electrolyte/photoelectrode interface, since most of the rays may reach the photoelectrode surface inside the bubble contact surface area. For example, at f_A= 78.5% and contact angle $\theta_c = 90^\circ$, the contact surface area coverage $f_S = f_A$ and most of the incident photons encounter the bubble/photoelectrode interface. However, for a hydrophilic photoelectrode surface, the bubble contact surface area is small, and the anti-reflective coating should then

be chosen to reduce the reflectance of the electrolyte/photoelectrode interface only. For example, in the case of Si photoelectrodes considered in this study, $a \sim 150$ nm thick titania film could serve as an anti-reflective coating, as demonstrated experimentally in Refs. [62, 63]. In fact, Seger et al. [63] reported an increase of around 15% in the saturation photocurrent density owing to the antireflective properties of titania. In addition, titania coatings exhibit photoinduced hydrophilicity [64] and also act as a protection layer for the photoelectrode [53, 62, 63].

2.4 Conclusions

This chapter presented a comprehensive study to assess and quantify the optical losses caused by the presence of non-absorbing cap-shaped gas bubbles on large horizontal Si photoelectrode immersed in an aqueous electrolyte. Monte Carlo ray-tracing method was utilized to predict (i) the normal hemispherical reflectance R_{nh}, (ii) the area-averaged absorptance , and (iii) the local absorptance in the photoelectrode covered with bubbles. The optics in the photoelectrode without bubbles was used as a reference. It was established that bubble diameter and polydispersity did not have any significant effect on the optical losses for a given projected surface area coverage f_A. However, the optical losses depended on the contact angle and increased with f_A. Three different optical regimes were defined to explain the variation of optical losses with bubble contact angle θ_c based on the interplay of total internal reflection at the electrolyte/bubble interface and reflection at the bubble/photoelectrode interface. Overall, a maximum of 18% loss in the absorbed radiation was predicted in the photoelectrode covered with bubbles of contact angle $\theta_c = 120°$and projected area coverage $f_A = 78.5\%$. Scattering by bubbles also caused substantial local variation in the absorbed photon flux, with significant light concentration by up to a factor 2 outside the projected footprint of the bubble compared to a bare photoelectrode. The magnitude of absorbed photon flux just outside the bubble projected footprint was up to 4 times that inside. It was established that photoelectrodes with hydrophilic materials or coatings should be preferred to minimize the optical losses caused by the presence of bubbles. However, in these conditions,

the bubbles significantly redistributed the incident radiation on the photoelectrode surface, which may lead to more optical losses when performing experiments with small (mm-scale) photoelectrodes due to losses from the edges. In addition, an anti-reflective coating aimed at minimizing the reflectance of the electrolyte/photoelectrode interface can further reduce the back-scattering losses from the photoelectrode. However, at high bubble coverages and high contact angles, it would be beneficial to explore an anti-reflective coating that minimizes the reflectance of the bubble/photoelectrode interface instead. Finally, high bubble coverages not only increase the optical losses but also the kinetic and ohmic losses. Therefore, convection in the electrolyte and/or the use of surfactants can facilitate the removal of bubbles.

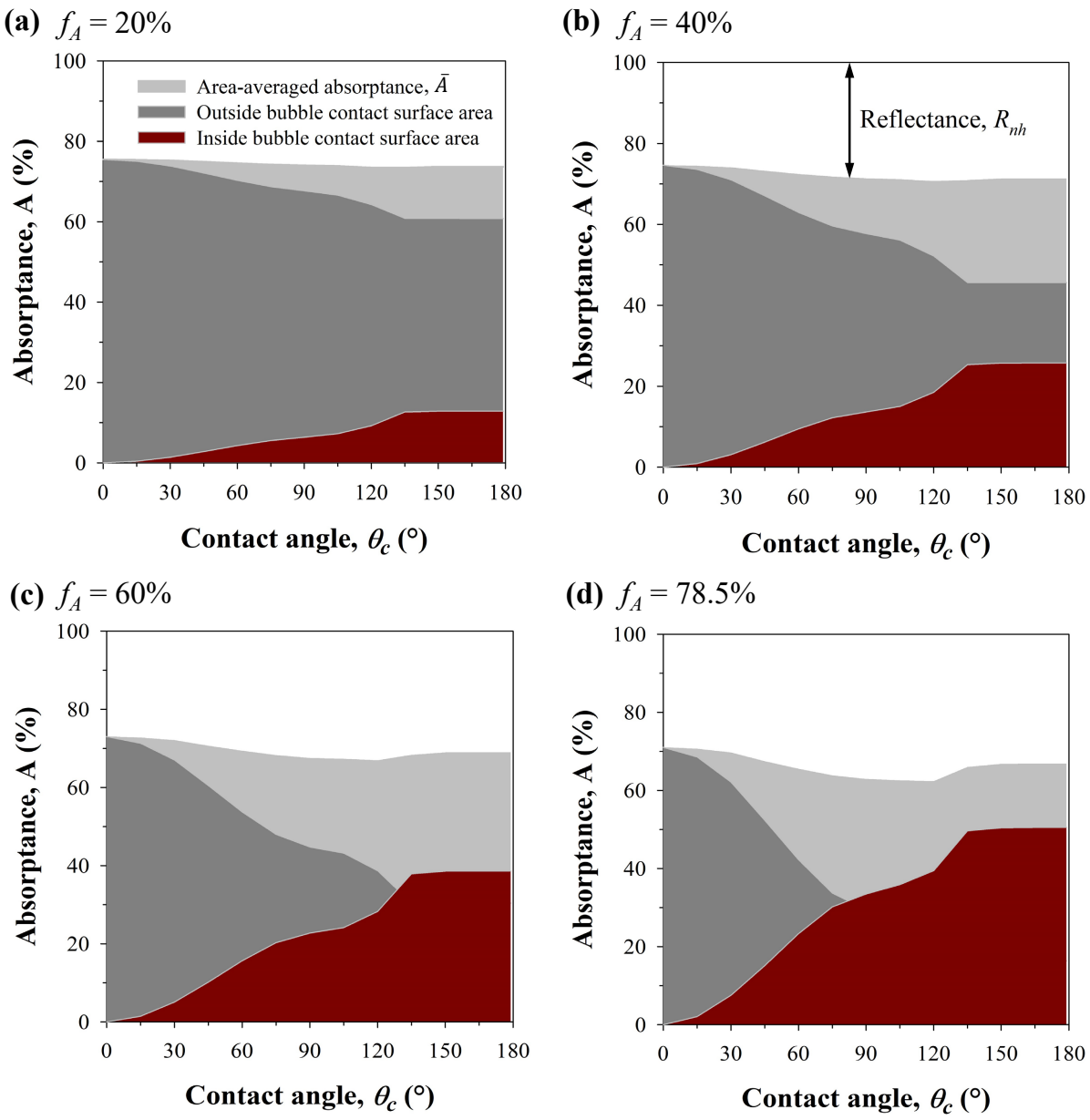

Figure 2.9: Fraction of the incident radiation reflected and absorbed inside or outside the bubble contact surface area as functions of contact angle θ_c for projected surface area coverages (a) $f_A = 20\%$, (b) $f_A = 40\%$, (c) $f_A = 60\%$, and (d) $f_A = 78.5\%$.

CHAPTER 3

Light transfer through bubble-filled electrolyte for solar water splitting

This chapter systematically quantifies the optical losses caused by hydrogen or oxygen bubbles released from an illuminated photoelectrode and rising through a semitransparent aqueous electrolyte during photoelectrochemical water splitting. Indeed, the presence of gas bubbles increases backscattering of the incident radiation and absorption losses in the electrolyte due to multiple scattering. These optical losses were quantified by predicting (i) the normal-hemispherical reflectance, (ii) the electrolyte absorptance, and (iii) the area-averaged absorptance of the photoelectrode for wavelengths between 400 and 1100 nm using the Monte Carlo ray-tracing method. Results are reported for randomly distributed monodisperse and polydisperse bubbles with diameter ranging between 100 µm and 1 mm, volume fraction varying between 0 and 30%, and plume thickness ranging from 2 to 20 mm. The photoelectrode absorptance and efficiency were found to decrease with decreasing bubble diameter and increasing bubble volume fraction and plume thickness. In fact, without careful design and operation, the optical losses can significantly degrade the photoelectrode performance. The contribution to the total optical losses from bubbles attached to the photoelectrode surface increased with increasing bubble contact surface area coverage and decreasing plume thickness. The results indicate that increasing the bubble departure diameter by increasing the surface tension of the electrolyte/bubble interface and flowing the electrolyte to reduce the plume thickness can substantially minimize the optical losses. Additionally, illuminating the PEC cell from the anode side could be particularly beneficial given the larger size and smaller volume fraction of oxygen bubbles as compared to hydrogen bubbles.

3.1 Background

In Chapter 2, we quantified the effect of surface-attached spherical cap-shaped bubbles on optical losses in PEC cells consisting of large horizontal photoelectrodes immersed in a non-absorbing electrolyte and subjected to normally incident monochromatic radiation [49]. Monte Carlo ray-tracing method [37, 42] was used to predict the normal-hemispherical reflectance and the area-averaged and local absorptance of the photoelectrode in the visibile part of the solar spectrum for bubble contact angle θ_c varying between 0° and 180°, bubble diameter D ranging from 0.25 to 1.75 mm, and projected surface area coverage f_A varying from 0 to 78.5%. The bubble diameter and polydispersity were found to have no significant effect on the optical losses for a given projected surface area coverage f_A. However, the optical losses increased with increasing projected surface area coverage f_A due to stronger reflectance at the bubble/photoelectrode interface as compared to the electrolyte/photoelectrode interface. Three different optical regimes were defined by comparing the bubble contact angle θ_c and the critical angle θ_{cr} for total internal reflection at the electrolyte/bubble interface. The optical losses in each regime were based on the interplay of reflections at the electrolyte/bubble or the bubble/photoelectrode interface. In addition, the bubbles were found to significantly redistribute the incident light intensity causing most photons to be absorbed in a rim outside the projected footprint of the bubble attached to the photoelectrode surface. The study predicted optical losses up to 18% caused by bubbles with contact angle $\theta_c = 120°$, diameter $D = 1$ mm, and projected surface area coverage $f_A = 78.5\%$. Finally, hydrophilic photoelectrodes were recommended to reduce the bubble coverage on the photoelectrode which not only minimizes the optical losses but also increases the electrochemically active surface area of the photoelectrode.

However, our previous study [49] was limited to the situation when bubbles were attached to the photoelectrode surface with no additional bubbles in the electrolyte volume. Such a scenario corresponds to the onset of water splitting reaction and/or to PEC cells having horizontal photoelelectrodes covered by a very thin layer of electrolyte. In all other configurations, the bubbles releasing from the photoelectrode surface and rising through the

electrolyte also scatter the incident light until they burst at the free surface of the electrolyte or are convectively removed. Figure 3.1 shows the schematics of a photoelectrode in (a) vertical and (b) horizonal configuration, exposed to solar radiation through a bubble-filled electrolyte in a PEC cell. Figure 3.1(c) shows the photograph of a horizontal planar Si photoelectrode immersed in an aqueous electrolyte generating O_2 bubbles while being illuminated from the top [53]. Thus, the gas bubbles attached to the photoelectrode surface as well as those dispersed in the electrolyte scatter the incident light, resulting in optical losses.

Additionally, most previous studies [12,52,53] illuminated the photoelectrode with monochromatic light at a wavelength for which the aqueous electrolyte was transparent. They provided limited discussion on the parameters responsible for the bubble-induced optical losses due to difficulties in controlling or characterizing the bubbles experimentally. Specifically, the effects of bubble volume fraction and plume thickness on the optical losses were not quantified. In practice, a higher photocurrent density in a PEC cell increases the gas generation rate, but it also increases the bubble volume fraction and thus the optical losses. In addition, horizontal photoelectrodes may incur more optical losses than vertical ones as bubbles occupy the entire electrolyte thickness (see Figure 3.1) resulting in multiple scattering of the incident light. Finally, the optical losses further increase due to light absorption by the aqueous electrolyte in the near-infrared portion of the solar spectrum.

The present study aims to systematically quantify the optical losses caused by gas bubbles forming at the photoelectrode surface and rising through the semitransparent electrolyte under normally incident sunlight. The Monte Carlo ray-tracing (MCRT) method was used to predict the area-averaged spectral absorptance of an infinitely large photoelectrode surface illuminated through a volume of electrolyte filled with randomly distributed monodisperse or polydisperse gas bubbles for a wide range of bubble diameter, volume fraction, and plume thickness. The predictions were systematically compared with those for a bare photoelectrode without any bubbles in the electrolyte. The results will be instrumental in optimizing the design and improving the performance of PEC cells for their envisioned outdoor operation.

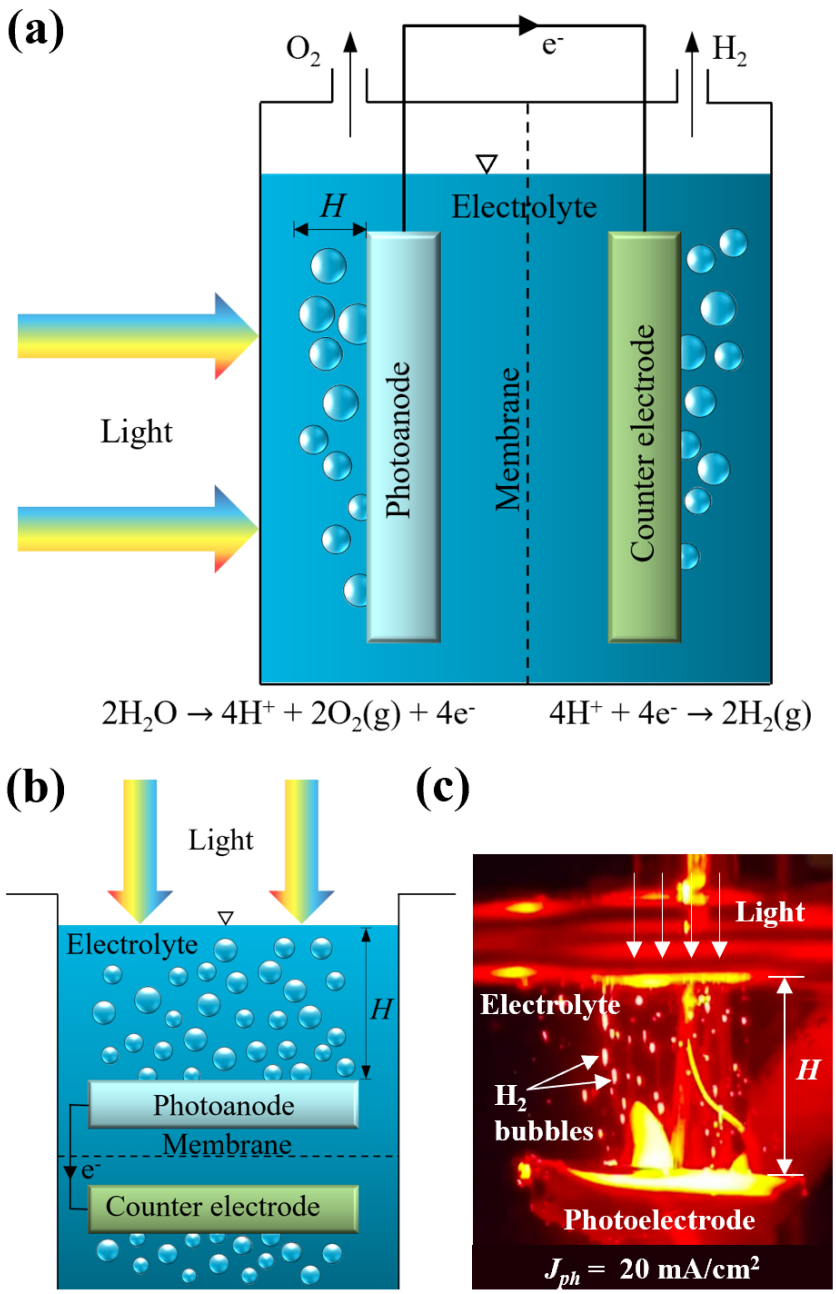

Figure 3.1: Schematic of light transfer to a (a) vertical and (b) horizontal photoelectrode in a PEC cell with a plume of gas bubbles of thickness H scattering the incident sunlight. (c) Photograph of hydrogen gas bubbles dispersed in the electrolyte covering a horizontal Si planar photoelectrode illuminated from the top (reprinted with permission from Ref. [53]. Copyright © 2021 Royal Society of Chemistry).

3.2 Analysis

3.2.1 Problem statement and parametrization

Let us consider a square opaque Si photoelectrode of length L and complex index of refraction $m_{p,\lambda} = n_{p,\lambda} + ik_{p,\lambda}$ immersed in an aqueous electrolyte of complex index of refraction $m_{e,\lambda} = n_{e,\lambda} + ik_{e,\lambda}$. The photoelectrode is subjected to collimated and normally incident polychromatic light through a bubble plume of thickness H. The electrolyte volume contains N_v randomly distributed polydisperse spherical gas bubbles of diameter $(D_{v,i})_{1\leq i\leq N_v}$ following a normal size distribution $f(D)$, as illustrated in Figure 3.2. In addition, N_s polydisperse spherical cap-shaped bubbles having normal size distribution with diameter $(D_{s,j})_{1\leq j\leq N_s}$ and contact angle θ_c are attached to the photoelectrode surface with a contact surface area coverage f_s. The total volume fraction of the bubbles in the electrolyte and on the photoelectrode surface is denoted by f_v. The bubbles scatter light such that only a fraction of the incident light intensity is absorbed in the photoelectrode and converted into photocurrent, as accounted for by the photoelectrode's area-averaged spectral absorptance $\bar{A}_\lambda$. The remaining incident radiation is lost either by (i) backscattering, as quantified by the spectral normal-hemispherical reflectance $R_{nh,\lambda}$, or by (ii) absorption by the electrolyte, as represented by the spectral absorptance $A_{e,\lambda}$. Overall, an energy balance on the radiation incident on an opaque photoelectrode can be written as $R_{nh,\lambda} + A_{e,\lambda} + \bar{A}_\lambda = 1$. The objective of the present study is to quantify the bubble-induced optical losses in a PEC cell represented by $R_{nh,\lambda}$ and $A_{e,\lambda}$ and to assess the effects of bubble size distribution $f(D)$, volume fraction f_v, plume thickness H as well as contact surface area coverage f_s on the photoelectrode performance.

3.2.2 Assumptions

To make the problem mathematically trackable, the following assumptions were made: (1) dimensions of the photoelectrode and bubbles were much larger than the wavelength λ of the incident radiation so that geometric optics was valid and wave effects could be neglected. (2) All surfaces were optically smooth with specular reflection and refraction occurring at all

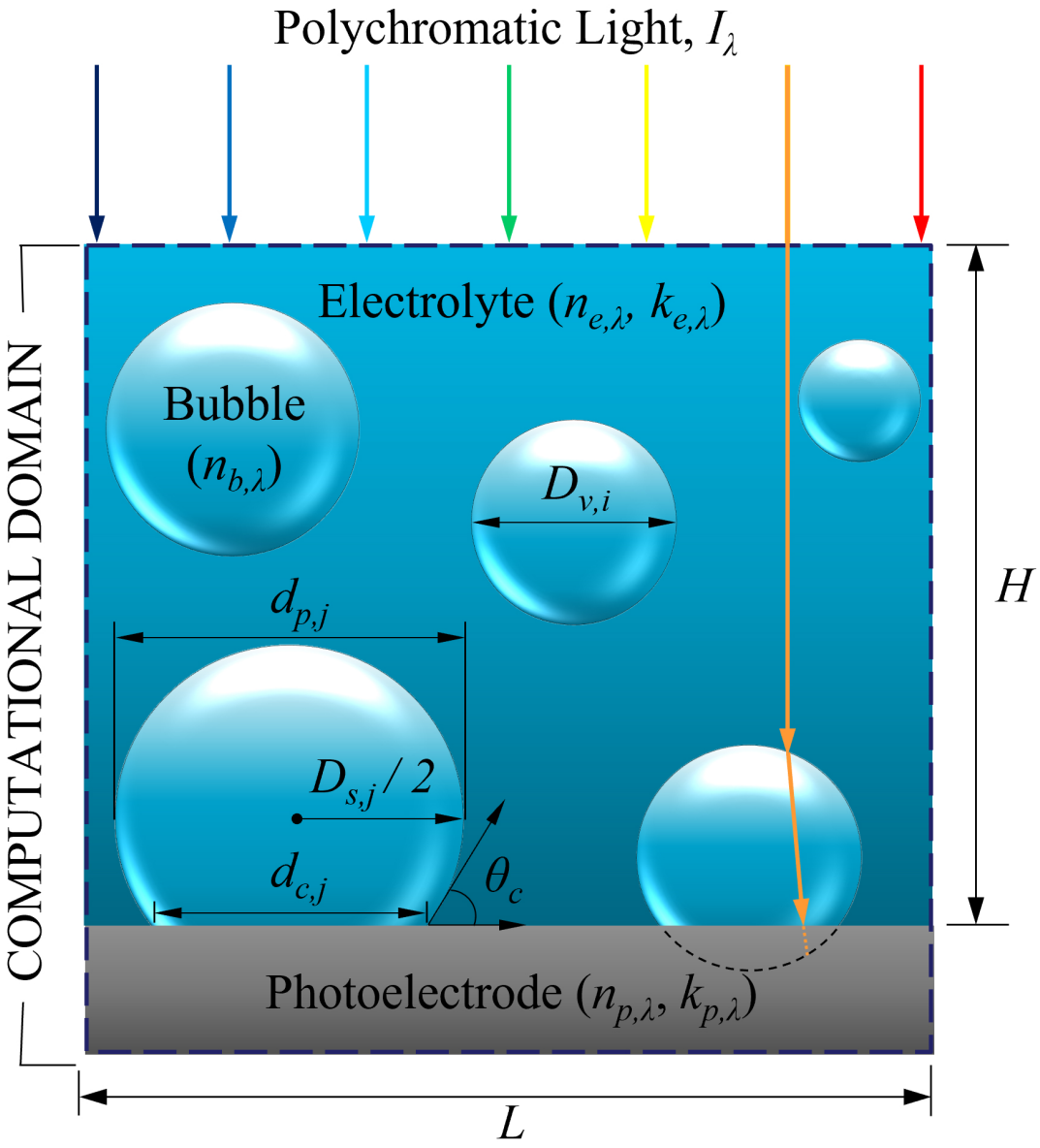

Figure 3.2: Side view of the 3D computational domain considered in this study showing polydisperse spherical bubbles of diameter $(D_{v,i})_{1\leq i\leq N_v}$ dispersed in the electrolyte volume and cap-shaped bubbles of diameter $(D_{s,j})_{1\leq j\leq N_s}$ attached to the photoelectrode surface with contact angle θ_c. Rays reaching a location below the photoelectrode surface, e.g., orange ray, were retraced and either reflected or refracted at the bubble/photoelectrode interface.

interfaces according to Snell's law and Fresnel's equations. (3) Reflection at the top boundary of the computational domain was ignored. (4) Gas bubbles were spherical and randomly distributed in the electrolyte volume. (5) Gas bubbles attached to the photoelectrode surface were spherical cap-shaped and randomly distributed with constant volume and constant contact angle θ_c. (6) The gas inside the bubbles was transparent with $n_{b,\lambda} = 1.0$. (7) The photoelectrode was opaque so that all photons transmitted through the photoelectrode surface were absorbed. (8) The bubble plume thickness H was the same over the entire photoelectrode surface. (9) The thickness of the semitransparent electrolyte layer covering the photoelectrode was equal to the bubble plume thickness H.

3.2.3 Computational bubble generation

Monodisperse or polydisperse spherical bubbles having normal size distribution with mean diameter $\bar{D}$ and standard deviation σ were computationally generated and randomly distributed in the electrolyte volume following a procedure based on our previous study [49]. First, random bubble diameters were generated in accordance with the imposed size distribution until their total volume fraction in the electrolyte reached the desired value. Then, the bubbles were assigned random center locations (x_i, y_i, z_i) while ensuring that they did not overlap and were confined within the electrolyte volume. The corresponding volume fraction f_v for bubbles dispersed in the electrolyte is expressed as

$$f_v = \left(\sum_{i=1}^{N_v} \frac{\pi}{6} D_{v,i}^3 \right) / HL^2, \tag{3.1}$$

where N_v is the number of bubbles dispersed in the electrolyte volume, $D_{v,i}$ is the diameter of the i^{th} bubble, H is the bubble plume thickness, and L is the length of the square photoelectrode.

To simulate the presence of spherical cap-shaped bubbles on the photoelectrode surface, in addition to those in the electrolyte volume, spherical bubbles satisfying an imposed volume fraction were computationally generated and randomly distributed, as previously described. However, this time, the bubbles were allowed to intersect the bottom surface of the electrolyte domain. The resulting cap-shaped bubbles were identified and moved per-

pendicularly to the bottom surface to achieve the desired bubble contact angle θ_c. Then, the total volume fraction f_v of bubbles comprising (i) N_s spherical cap-shaped bubbles of diameter $(D_{s,j})_{1\leq j\leq N_s}$ and contact angle θ_c attached to the photoelectrode surface and (ii) N_v spherical bubbles of diameter $(D_{v,i})_{1\leq j\leq N_v}$ in the electrolyte volume is given by

$$f_v = \left[\sum_{i=1}^{N_v} \frac{\pi}{6} D_{v,i}^3 + \sum_{j=1}^{N_s} \frac{\pi}{24} D_{s,j}^3 (2 + 3cos\theta_c - cos^3\theta_c)\right] / HL^2. \tag{3.2}$$

Moreover, the projected surface area coverage f_A of bubbles attached to the photoelectrode surface is given by

$$f_A = \left(\sum_{j=1}^{N_s} \frac{\pi}{4} d_{p,j}^2\right) / L^2, \tag{3.3}$$

where $d_{p,j}$ is the projected diameter of the j^{th} cap-shaped bubble defined as $d_{p,j} = D_{s,j}$ for $0° \leq \theta_c < 90°$ and $d_{p,j} = D_{s,j}\text{sin}\theta_c$ for $90° \leq \theta_c < 180°$. Similarly, the bubble contact surface area coverage f_s on the photoelectrode can be defined as

$$f_s = \left(\sum_{j=1}^{N_s} \frac{\pi}{4} d_{c,j}^2\right) / L^2, \tag{3.4}$$

where $d_{c,j}$ is the diameter of the contact circle of the j^{th} cap-shaped bubble given by $d_{c,j} = d_{p,j}\text{sin}\theta_c$ for $\theta_c \leq 90°$, and $d_{c,j} = d_{p,j}$ for $\theta_c > 90°$.

3.2.4 Closure laws

Spectral simulations were performed over wavelengths ranging between 300 nm and 3 µm encompassing the solar spectrum. The spectral refractive $n_{e,\lambda}$ and absorption $k_{e,\lambda}$ indices of the aqueous electrolyte were assumed to be that of water reported in Ref. [65]. The photoelectrode material was chosen to be crystalline undoped Si whose spectral refractive $n_{p,\lambda}$ and absorption $k_{p,\lambda}$ indices were obtained from Ref.[66].

Unless otherwise noted, monodisperse bubbles of diameter $D = 1$ mm were simulated based on the values reported in the literature [12,13] and also based on the bubble departure diameter of 1.14 mm at STP predicted by Fritz correlation [67] for a hydrophilic surface with contact angle $\theta_c = 20°$. However, when studying the effect of monodisperse bubble diameter, D was taken as either 0.1, 0.3, 0.5, or 1 mm. The effect of polydispersity was also analyzed

by using normally distributed bubble diameters with a mean value $\bar{D} = 1$ mm and standard deviation $\sigma = 0.25$ mm with bubble diameter $D_{v,i}$ such that $\bar{D} - 3\sigma < D_{v,i} < \bar{D} + 3\sigma$. The bubble volume fraction f_v ranged between 0 and 30% corresponding to the bubbly flow regime [67]. Typically, the bubble volume fraction encountered in water electrolysis varies between 0 and 12% [6]. The bubble plume thickness H varied between 2 and 20 mm according to the typical electrolyte thicknesses used in photoelectrochemical cells [14]. The length of the square photoelectrode was $L = 10$ mm with periodic boundary conditions, unless otherwise noted.

3.2.5 Methods of solution

3.2.5.1 Light transfer

The Monte Carlo ray-tracing method [37, 42] was used to predict the normal-hemispherical reflectance $R_{nh,\lambda}$, the electrolyte absorptance $A_{e,\lambda}$, and the area-averaged absorptance $\bar{A}_\lambda$ of the opaque photoelectrode subjected to normally incident light through a bubble-filled semitransparent electrolyte volume. Collimated photon bundles or "rays" were incident on the computational domain assuming periodic boundary conditions such that the rays reaching any of the four sides of the computational domain re-entered from the opposite side at the same height and in the same direction. The rays were traced until they were either absorbed in the photoelectrode or in the electrolyte, or were backscattered out from the top of the computational domain. The computational steps for each ray are listed in Appendix A.

All the simulations were performed with a total number of incident photon bundles equal to 10^7 necessary to achieve numerical convergence [43]. In order to validate the Monte Carlo ray-tracing (MCRT) code, three cases for which the analytical expressions of the photoelectrode absorptance were known were simulated (see Appendix A).

3.2.5.2 Bubble-induced optical losses

First, the area-averaged photoelectrode absorptance $\bar{A}_\lambda$ was normalized with the absorptance $\bar{A}_{0,\lambda}$ of a photoelectrode in the absence of bubbles. The latter can be written as [37]

$$\bar{A}_{0,\lambda} = (1 - \rho_{ep,\lambda})e^{-\kappa_{e,\lambda}H} \tag{3.5}$$

where H is the thickness (in m) of semitransparent electrolyte covering the photoelectrode, $\kappa_{e,\lambda} = 4\pi k_{e,\lambda}/\lambda$ is the absorption coefficient of the electrolyte (in m^{-1}), and $\rho_{ep,\lambda}$ is the reflectance at the optically smooth interface between the electrolyte and the photoelectrode such that [37]

$$\rho_{ep,\lambda} = \frac{(n_{e,\lambda} - n_{p,\lambda})^2 + (k_{e,\lambda} - k_{p,\lambda})^2}{(n_{e,\lambda} + n_{p,\lambda})^2 + (k_{e,\lambda} + k_{p,\lambda})^2}. \tag{3.6}$$

Then, the bubble-induced optical losses (%) were given by (1 - $\bar{A}_\lambda/\bar{A}_{0,\lambda}$).

3.2.5.3 Photoelectrode efficiency limit

A photoelectrode immersed in an electrolyte behaves in a similar way as a solar cell due to the formation of a semiconductor-electrolyte junction that separates the photogenerated charge carriers [68]. However, the maximum possible efficiency of a photoelectrode is always smaller than or equal to that of a photovoltaic (PV) solar cell made from the same semiconductor and operating at its maximum power point (MPP) due to the photovoltage of 1.23 V required for driving the water splitting reaction [68, 69]. The equality only holds for semiconductors that generate photovoltage exactly equal to 1.23 V at STP. The more commonly cited solar-to-hydrogen (STH) efficiency is only applicable to photoelectrodes if they can generate the photovoltage required for water splitting and compensate for overpotential losses [68, 69]. Here, we used PV efficiency to quantify the impact of bubbles since it corresponds to the upper bound of the photoelectrode efficiency for a given material.

Holmes-Gentle et al. [70] developed an open-source computational tool to predict the PV efficiency limit of a semiconductor based on the detailed-balance model first proposed by Shockley and Quiesser [15]. The model accounts for the spectral irradiance of sunlight and recombination losses. However, it neglects light absorption in the electrolyte and backscat-

tering by the bubbles and photolelectrode surface. Here, we incorporate these optical losses and predict the maximum PV efficiency to quantify the deleterious effect of bubbles on the performance of a photoelectrode. To do so, spectral simulations in wavelength intervals of 10 nm were performed over 1 Sun AM 1.5G reference spectrum, according to standard ASTM G173-3, for different volume fractions f_v and plume thicknesses H considering only bubbles dispersed in the electrolyte. Then, the spectral solar irradiance was multiplied by the photoelectrode's spectral absorptance predicted from MCRT simulations. Finally, the spectral solar flux absorbed in the photoelectrode was used as input into the open-source tool developed by Holmes-Gentle et al. [70] to predict the PV efficiency limit of a Si photoelectrode having a band gap of 1.12 eV.

3.3 Results and discussion

This section presents the effects of (1) bubble size distribution $f(D)$, (2) volume fraction f_v, (3) plume thickness H, and (4) surface area coverage f_s on the normal-hemispherical reflectance $R_{nh,\lambda}$, electrolyte absorptance $A_{e,\lambda}$, and area-averaged absorptance $\bar{A}_\lambda$ of a Si photoelectrode. First, the photoelectrode surface was assumed to be free of cap-shaped bubbles so that $f_s = 0\%$ and bubbles were only present in the electrolyte volume. Then, the effect of surface-attached cap-shaped bubbles on the overall optical losses was quantified. In all cases, the normalized area-averaged absorptance $\bar{A}_\lambda/A_{0,\lambda}$ was used to compare the spectral optical losses in a PEC cell with and without bubbles for given bubble diameter D, volume fraction f_v, and plume thickness H.

3.3.1 Effect of bubble size distribution

Figures 3.3(a) and 3.3(b) respectively plot the spectral normal-hemispherical reflectance $R_{nh,\lambda}$ and area-averaged photoelectrode absorptance $\bar{A}_\lambda$ as functions of wavelength λ for monodisperse bubbles of diameter $D = 1$ mm or polydisperse bubbles with either normal size distribution with mean diameter $\bar{D} = 1$ mm and standard deviation $\sigma = 0.25$ mm, or lognormal size distribution with mean $\mu = 0.05$ and standard deviation $\chi = 0.25$ (see Figure

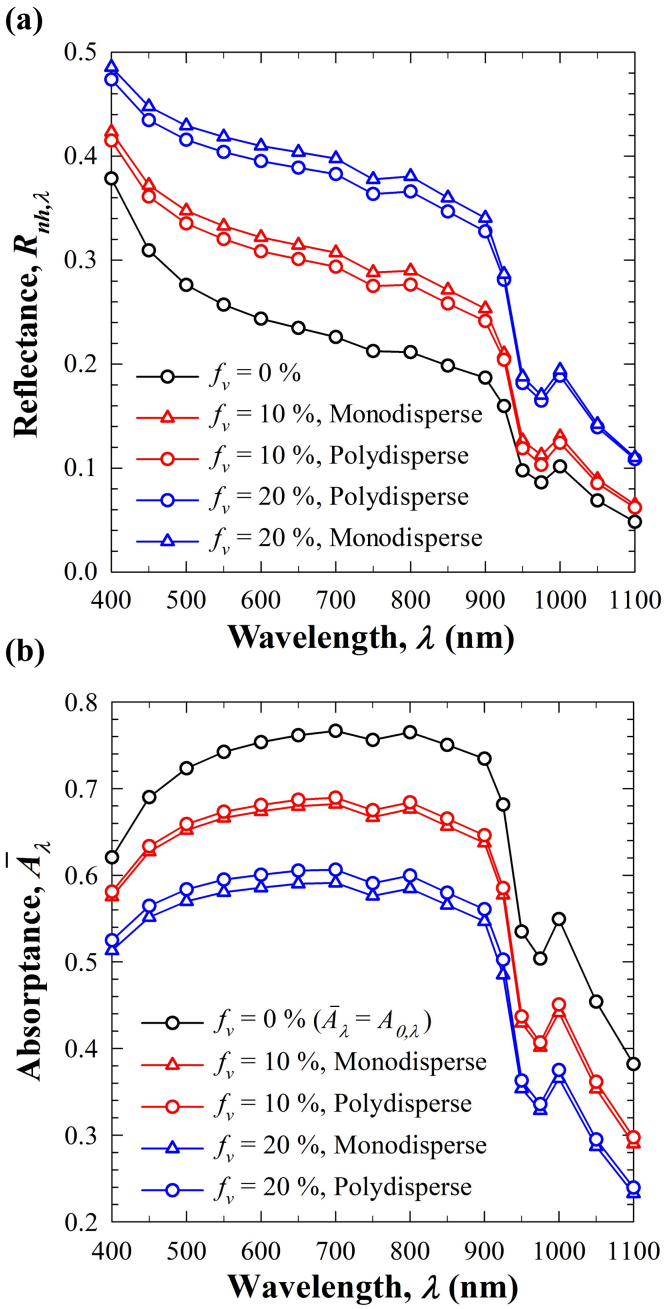

Figure 3.3: Comparison of (a) spectral normal-hemispherical reflectance $R_{nh,\lambda}$ and (b) spectral area-averaged photoelectrode absorptance $\bar{A}_\lambda$ for either monodisperse bubbles or polydisperse bubbles with normal size distribution for bubble volume fractions f_v of 10% or 20%.

S3). The probability density functions for the normal $f_n(D)$ and lognormal size distribution $f_{ln}(D)$ are respectively expressed as

$$f_n(D) = \frac{1}{\sigma\sqrt{2\pi}} e^{-\frac{1}{2}\left(\frac{D-\bar{D}}{\sigma}\right)^2} \; and \; f_{ln}(D) = \frac{1}{D\chi\sqrt{2\pi}} e^{\left(-\frac{(\ln D-\mu)^2}{2\chi^2}\right)}. \tag{3.7}$$

Here, the bubble volume fraction f_v was either 10% or 20% and the bubble plume thickness H was 10 mm. Predictions for a photoelectrode immersed in the electrolyte without any bubbles (i.e., $f_v = 0\%$) are also shown as references. Figure **??** establishes that the presence of bubbles in the electrolyte increased the reflection losses and decreased light absorption in the photoelectrode.

In addition, for a given volume fraction f_v, bubble polydispersity led to a slightly smaller reflectance $R_{nh,\lambda}$ and a larger photoelectrode absorptance $\bar{A}_\lambda$ compared to when the bubbles were monodisperse with the same mean diameter. However, these observations were less pronounced for $\lambda > 900$ nm, when both $R_{nh,\lambda}$ and $\bar{A}_\lambda$ decreased substantially due to light absorption by the aqueous electrolyte. In fact, for a given volume fraction f_v and mean bubble diameter $\bar{D} = 1$ mm, the relative difference between the predictions of $R_{nh,\lambda}$ and $\bar{A}_\lambda$ for polydisperse and monodisperse bubbles was less than 5% at all wavelengths despite a relatively wide bubble size distribution. In addition, spectral predictions for lognormal and normal size distributions were similar for the same mean diameter and range of bubble diameters for all wavelengths. Figures S4(a) and S4(b) show similar trends for smaller polydisperse bubbles having either normal size distribution with mean diameter $\bar{D} = 300$ µm and standard deviation $\sigma = 75$ µm, or lognormal distribution for diameters (in mm) with mean μ = -1.14 and standard deviation $\chi = 0.24$. Figure S5 compares the probability density functions for these two size distributions. Thus, the bubble volume fraction f_v and mean diameter $\bar{D}$ had a dominant effect on $R_{nh,\lambda}$ and $\bar{A}_\lambda$ while the bubble polydispersity had a secondary effect.

Figures A.6(a) and A.6(b) plot the spectral normal-hemispherical reflectance $R_{nh,\lambda}$ and area-averaged photoelectrode absorptance $\bar{A}_\lambda$ as functions of wavelength λ for normally distributed polydisperse bubbles with mean diameter $\bar{D} = 0.3$ or 1 mm for volume fraction $f_v = 10\%$. Here, the standard deviation σ was taken as 0, $\bar{D}/4$, or $\bar{D}/2$ and the bubble

diameters were considered in the range $\bar{D} - 2\sigma < D < \bar{D} + 2\sigma$. Figure S6 shows that the standard deviation had a more pronounced effect on the predictions for bubbles with smaller mean diameter. Overall, the effect of bubble polydispersity should be accounted for, particularly when the bubbles are small.

3.3.2 Effect of bubble diameter D

Figure 3.4(a) presents the normalized area-averaged photoelectrode absorptance $\bar{A}_\lambda/\bar{A}_{0,\lambda}$ as a function of wavelength λ for bubble diameters D = 0.1, 0.3, 0.5, and 1 mm for volume fraction $f_v = 10\%$ and plume thickness $H = 10$ mm. It indicates that the spectral variation of $\bar{A}_\lambda/\bar{A}_{0,\lambda}$ followed a similar trend for all bubble diameters i.e., a slight decrease in magnitude as λ increased from 400 to 900 nm, and a substantial decrease beyond 900 nm. However, the drop was not as sharp as that seen for absorptance $\bar{A}_\lambda$ in Figure 3.3 because the normalization factor $\bar{A}_{0,\lambda}$ accounts for the significant light absorption by the aqueous electrolyte even in the absence of bubbles.

Figure 3.4(a) also shows that the photoelectrode absorptance decreased sharply with decreasing bubble diameter. In fact, for $f_v = 10\%$ and $H = 10$ mm, the optical losses for bubble diameter $D = 100$ µm were nearly 5 times larger than those for diameter D = 1 mm for all wavelengths considered. To identify the different underlying mechanisms, Figure **??**(b) plots the corresponding normal-hemispherical reflectance R_{nh}, the electrolyte absorptance A_e, and the area-averaged photoelectrode absorptance $\bar{A}$ as functions of bubble diameter D at wavelength $\lambda = 950$ nm when absorption by the electrolyte was significant. It indicates that the photoelectrode absorptance $\bar{A}$ decreased with decreasing bubble diameter primarily due to large reflection losses caused by multiple scattering from a large number of bubbles. On the other hand, the electrolyte absorption losses remained nearly constant and independent of bubble diameter since absorption is a volumetric phenomenon and the total electrolyte volume remained constant for given values of volume fraction f_v and plume thickness H.

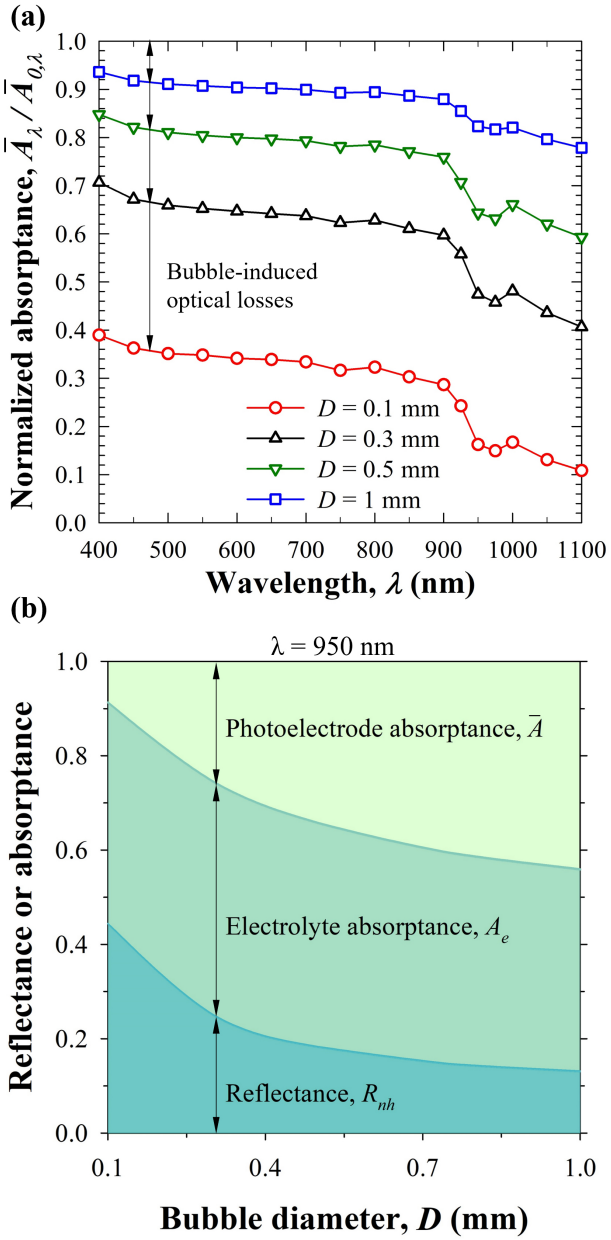

Figure 3.4: (a) Normalized area-averaged photoelectrode absorptance $\bar{A}_\lambda/\bar{A}_{0,\lambda}$ as a function of wavelength for different bubble diameters. (b) Normal-hemispherical reflectance R_{nh}, electrolyte absorptance A_e, and area-averaged photoelectrode absorptance $\bar{A}$ as functions of bubble diameter D at wavelength $\lambda = 950$ nm. In all cases, the bubble volume fraction was $f_v = 10\%$ and the plume thickness was $H = 10$ mm.

3.3.3 Effect of bubble volume fraction f_v

Figure 3.5(a) plots the normalized area-averaged photoelectrode absorptance $\bar{A}_\lambda/\bar{A}_{0,\lambda}$ as a function of wavelength λ for bubble volume fractions f_v = 5%, 10%, 20%, and 30% for bubble diameter $D = 1$ mm and plume thickness $H = 10$ mm. Here, the spectral variation of normalized absorptance $\bar{A}_\lambda/\bar{A}_{0,\lambda}$ was similar to that in Figure 3.4(a) for all volume fractions considered. Interestingly, Figure 3.5(a) shows that light absorption in the photoelectrode decreased substantially with increasing bubble volume fraction f_v. In fact, the bubble-induced optical losses for $f_v = 30\%$ reached as high as 30% in the visible, and up to 50% at wavelength $\lambda = 1100$ nm when the electrolyte was semitransparent. This indicates that, in practice, a high gas generation rate in PEC cells, which results in large bubble volume fraction, also leads to large optical losses. In turn, the generated photocurrent density decreases, as well as the gas generation rate and the bubble volume fraction. Such an oscillatory behavior, caused by light scattering by generated bubbles, may lead to oscillating photocurrent observed in chronoamperometry experiments [12].

Figure 3.5(b) presents the normal-hemispherical reflectance R_{nh}, the electrolyte absorptance A_e, and the area-averaged photoelectrode absorptance $\bar{A}$ as functions of bubble volume fraction f_v for diameter $D = 1$ mm and plume thickness $H = 10$ mm at wavelength $\lambda = 950$ nm. It establishes that the photoelectrode absorptance decreased significantly with increasing volume fraction f_v due to increasing reflection losses and high absorption losses. On one hand, the reflectance R_{nh} increased monotonously with f_v due to backscattering and multiple scattering by the increasing number of bubbles. On the other hand, the electrolyte absorptance A_e first increased slightly and then plateaued with increasing f_v, which can be attributed to the interplay between increasing mean free path of scattered photons and decreasing electrolyte volume.

The trends presented in this study show good qualitative agreement with experimental results reported in Refs. [52, 53] showing larger optical losses at higher gas generation rates. However, a direct comparison of results was not possible owing to a lack of reported bubble volume fraction and plume thickness. Nonetheless, the optical losses predicted in this study

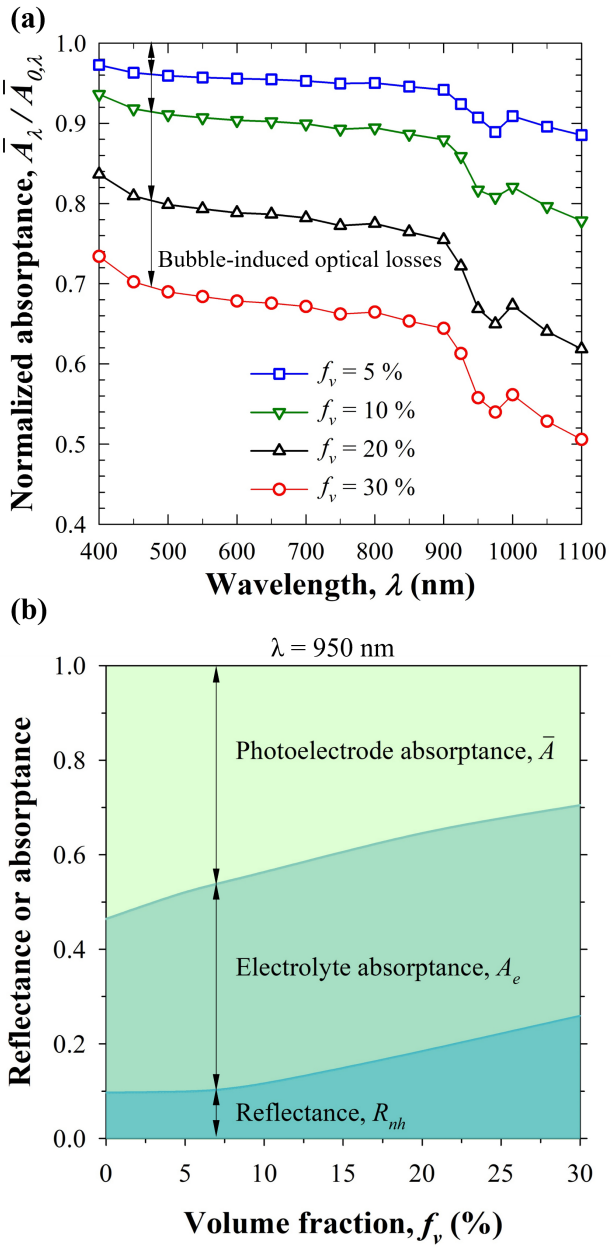

Figure 3.5: (a) Normalized area-averaged photoelectrode absorptance $\bar{A}_\lambda/\bar{A}_{0,\lambda}$ as a function of wavelength for different volume fractions. (b) Normal-hemispherical reflectance R_{nh}, electrolyte absorptance A_e, and area-averaged photoelectrode absorptance $\bar{A}$ as functions of bubble volume fraction f_v at wavelength $\lambda = 950$ nm. In all cases, the bubble diameter was $D = 1$ mm and the plume thickness was $H = 10$ mm.

remained less than 10% for volume fractions $f_v < 10\%$, in agreement with the results reported experimentally [52, 53].

3.3.4 Effect of bubble plume thickness H

Figure 3.6(a) plots the normalized area-averaged photoelectrode absorptance $\bar{A}_\lambda/\bar{A}_{0,\lambda}$ as a function of wavelength λ for bubble plume thicknesses H = 2, 5, 10, and 20 mm for bubble diameter D = 1 mm and volume fraction $f_v = 10\%$. It indicates that the spectral variation of normalized absorptance $\bar{A}_\lambda/\bar{A}_{0,\lambda}$ was similar to those in Figures 3.4(a) and 3.5(a) for all thicknesses. Figure 3.6(a) also shows that the normalized absorptance $\bar{A}_\lambda/\bar{A}_{0,\lambda}$ decreased substantially with increasing thickness for all wavelengths. For $\lambda < 900$ nm, absorption by the electrolyte remained negligible, while the reflection losses increased with increasing plume thickness (see Figure A.3(a)) due to backscattering and multiple scattering. Interestingly, the reflectance R_{nh} decreased with increasing plume thickness H for all $\lambda > 900$ nm because the scattered radiation was more likely to be absorbed in the semitransparent electrolyte volume than to be backscattered. The same observations can be made in Figure 3.6(b) plotting the normal-hemispherical reflectance R_{nh}, the electrolyte absorptance A_e, and the area-averaged photoelectrode absorptance $\bar{A}$ as functions of bubble plume thickness H for diameter D = 1 mm and volume fraction $f_v = 10\%$ at wavelength λ = 950 nm.

3.3.5 Effect of additional bubbles on photoelectrode surface

This section aims to assess the contribution of cap-shaped bubbles attached to the photoelectrode surface to the total optical losses. The bubble contact angle was taken as $\theta_c = 90^\circ$ to maximize the bubble contact surface area coverage f_s and achieve large backscattering [49].

3.3.5.1 Effect of contact surface area coverage f_s

Figures 3.7(a) plots the normalized area-averaged photoelectrode absorptance $\bar{A}_\lambda/\bar{A}_{0,\lambda}$ as a function of wavelength λ for bubble diameter D = 1 mm, plume thickness H = 10 mm, and volume fraction f_v = 5%, 19.3%, and 28.3%, while the contact surface area coverage

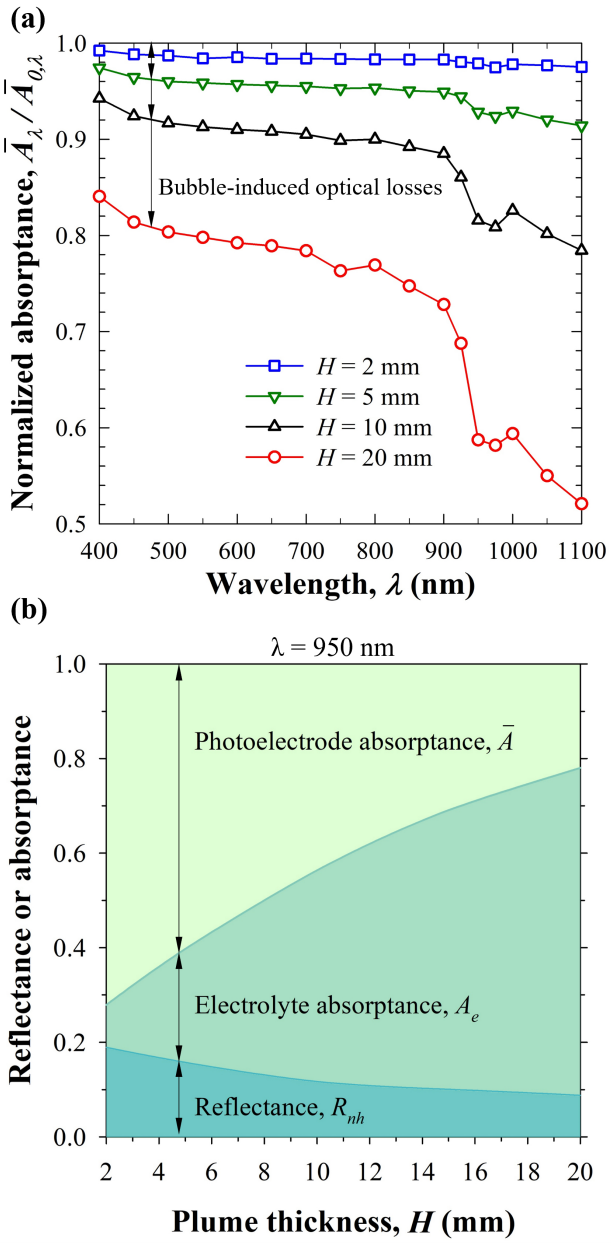

Figure 3.6: (a) Normalized area-averaged photoelectrode absorptance $\bar{A}_\lambda/\bar{A}_{0,\lambda}$ as a function of wavelength for different bubble plume thicknesses. (b) Normal-hemispherical reflectance R_{nh}, electrolyte absorptance A_e, and area-averaged photoelectrode absorptance $\bar{A}$ as functions of bubble plume thickness H at wavelength $\lambda = 950$ nm. In all cases, the bubble diameter was $D = 1$ mm and the volume fraction was $f_v = 10\%$.

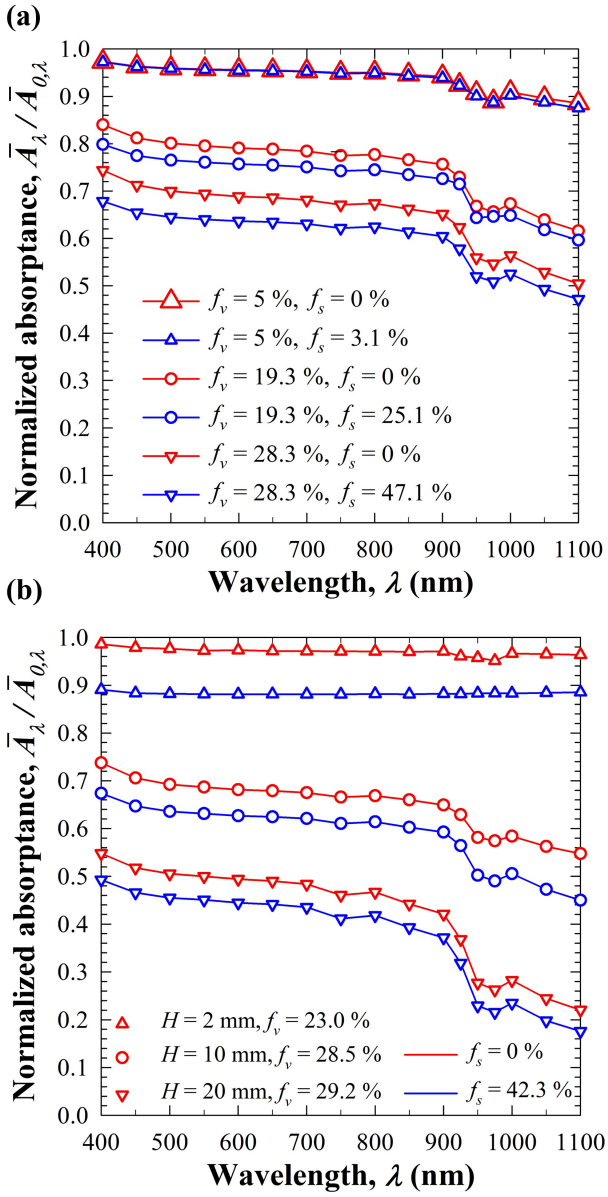

Figure 3.7: (a) Normalized area-averaged photoelectrode absorptance $\bar{A}_\lambda/\bar{A}_{0,\lambda}$ as functions of wavelength for (a) different bubble contact surface area coverages f_s for plume thicknesses H = 10 mm, and (b) different plume thicknesses for f_s = 22.0%. The results for f_s = 0% for the same volume fraction f_v are also presented. In all cases, the bubble diameter was D = 1 mm.

f_s was respectively equal to 3.1%, 25.1%, and 47.1%. Note that the contact surface area coverage f_s increased with increasing bubble volume fraction f_v in qualitative agreement with experimental observations. Results for a bare photoelectrode such that $f_s = 0\%$ at different volume fractions f_v are also shown as references. Figure 3.7(a) establishes that the surface-attached bubbles further increased the optical losses by up to 6% as compared to a bare photoelectrode for $f_v = 28.3\%$. These additional optical losses increased with increasing contact surface area coverage f_s due to the larger reflectance of the bubble/photoelectrode interface compared to the electrolyte/photoelectrode interface. Thus, Figure 3.7(a) confirms that the use of hydrophilic photoelectrodes reduces the optical losses.

3.3.5.2 Effect of plume thickness H

Figure 3.7(b) presents the normalized area-averaged photoelectrode absorptance $\bar{A}_\lambda/\bar{A}_{0,\lambda}$ as a function of wavelength λ for bubble plume thicknesses $H = 2$, 10, and 20 mm for bubble contact angle $\theta_c = 90°$, contact surface area coverage $f_s = 42.3\%$, and bubble diameter $D = 1$ mm. Again, the results were compared with those for the same volume fraction but with $f_s = 0\%$. Figure 3.7(b) indicates that the absolute difference between the predictions for $f_s = 0\%$ and $f_s = 42.3\%$ decreased from about 10% at $H = 2$ mm to less than 4% for $H = 20$ mm. This can be attributed to the reduced photon flux reaching the bubble-covered photoelectrode due to backscattering by the bubbles dispersed in the electrolyte. In other words, the effect of surface-attached bubbles on the overall optical losses decreased with increasing plume thickness H. Thus, photoelectrodes with thin bubble plumes (e.g., vertical photoelectrodes) experience optical losses primarily due to surface-attached cap-shaped bubbles [49]. By contrast, for thicker plumes, the optical losses are governed mainly by the bubbles dispersed in the electrolyte.

3.3.6 Discussion

Overall, the results suggest that in order to minimize the optical losses, the bubble diameter D should be large, while the bubble volume fraction f_v and plume thickness H should

be as small as possible. As per Fritz correlation [67], the bubble departure diameter can be increased by increasing the surface tension γ_{eb} of the electrolyte/bubble interface. This can be achieved by decreasing the operating temperature of the PEC cell [71] and/or by increasing the concentration of salts in the electrolyte [72]. Additionally, the bubble departure diameter can be increased by increasing the bubble contact angle θ_c [67] on the photoelectrode. However, such a strategy increases optical losses due to backscattering at the bubble/photoelectrode interfaces. It also decreases the electrochemically active surface area of the photoelectrode [49, 58]. To address this, it is recommended to use a hydrophilic photoelectrode surface of contact angle $\theta_c \approx 20^\circ$ which results in bubble departure diameter of around 1 mm at STP [67]. Such a bubble size would result in relatively low optical losses for a given gas generation rate.

The bubble-induced optical losses can be further mitigated by continuously removing the generated gas bubbles using forced convection in the electrolyte [6] which decreases both the bubble volume fraction f_v as well as the plume thickness H. The electrolyte layer should also be thin to minimize optical losses by absorption. However, the aqueous electrolyte must be readily available over the entire photoelectrode surface for water splitting to occur in the first place. In addition, the thickness of the electrolyte layer should not be too thin so as not to substantially increase the necessary pumping power. Therefore, the optimum electrolyte layer thickness corresponds to a compromise among optical losses, electrode performance, and process considerations.

One way to control the electrolyte layer thickness is to cover the photoelectrode with windows made of ultra-clear glass with anti-reflective coating that are highly transparent in the UV and visible wavelengths. Then, optical losses due to the presence of the window are negligible compared to those incurred by the presence of bubbles and by reflections at the electrolyte/photoelectrode interface, as predicted in this study. Nishiyama et al. [73] presented such a design with arrangements to adjust the gap between the window and the photocatalyst sheet panels to as low as 100 µm. For such small thickness, the nucleated bubbles coalesced thus decreasing scattering losses.

The results also indicate that horizontal photoelectrodes suffer larger optical losses than

vertical ones due to larger bubble plume thickness H (see Figure 3.1) for given bubble diameter D and volume fraction f_v. As a corollary, tilted photoelectrodes feature optical losses bounded by those for the horizontal and vertical orientations. Thus, the photoelectrode orientation should be optimized to maximize solar irradiation but also reduce the bubble plume thickness and thereby the optical losses.

3.3.7 Maximum achievable photovoltaic efficiency

Figure 3.8 plots the maximum achievable photovoltaic (PV) efficiency (%) as a function of bubble volume fraction f_v and plume thickness H for bubble diameter (a) $D = 1$ mm and (b) $D = 100$ µm, accounting for optical losses due to backscattering from bubbles in the electrolyte volume, absorption by the electrolyte, as well as reflections at the surface of a perfectly hydrophilic Si photoelectrode surface with no bubble coverage, i.e., $f_s = 0$. Indeed, accounting for the effect of surface-attached bubbles fell outside of the scope of the present study since the bubble coverage leads to local variations in the internal quantum efficiency in the photoelectrode causing some of the generated charge carriers to not participate in the redox reactions [12]. Figures 3.8(a) and 3.8(b) indicate that the maximum efficiency significantly decreases with decreasing bubble diameter and increasing volume fraction and/or plume thickness due to increasing optical losses. For example, the PV efficiency limit at $f_v = 10\%$, $H = 10$ mm, and $D = 1$ mm is about 20% compared with the efficiency limit of 33.5% for Si neglecting all optical losses. For small bubbles of diameter $D = 100$ µm, the efficiency limit was less than 10% for most plume thicknesses and volume fractions. In other words, optical losses can significantly reduce the photoelectrode performance.

One of the common ways to mitigate optical losses is to use an antireflective coating (ARC) on the photoelectrode surface. Typically for Si photoelectrodes, TiO_2 thin film can serve both as a protective and an antireflective coating [62, 63]. The effect of bubbles in such a scenario was investigated by assuming an idealized ARC-coated Si photoelectrode surface that was perfectly absorbing over the entire solar spectrum. The effect of ARC was computationally implemented by imposing the reflectance of the electrolyte/photoelectrode

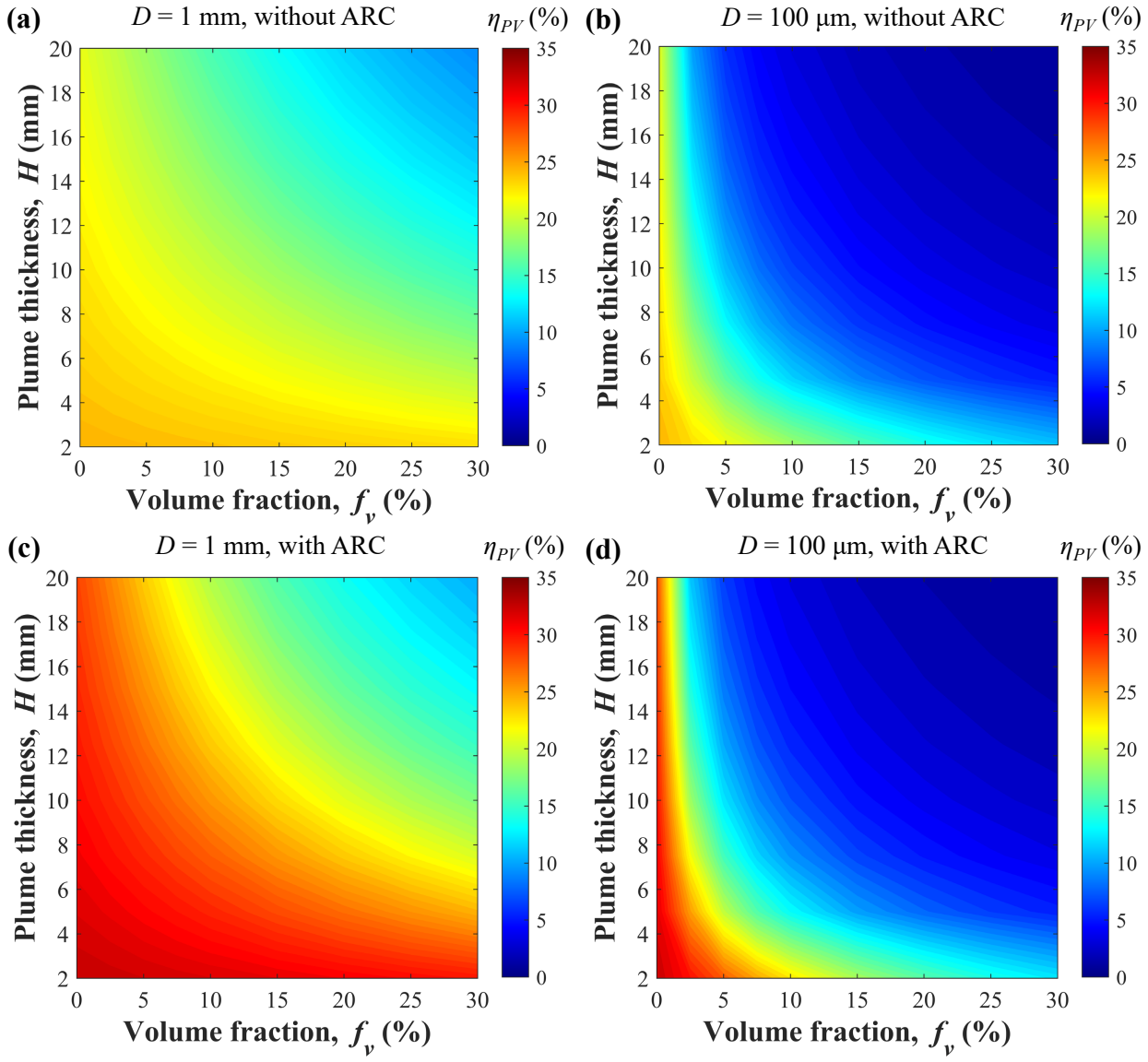

Figure 3.8: (a) Detailed-balance PV efficiency limit (%) incorporating bubble-induced optical losses for a Si photoelectrode immersed in a semitransparent aqueous electrolyte for bubble diameters (a) $D = 1$ mm and (b) $D = 100$ µm. The effect of using an antireflective coating (ARC) on the maximum achievable photoelectrode efficiency is also presented for bubble diameters (c) $D = 1$ mm and (d) $D = 100$ µm.

interface to be zero. Figures 3.8(c) and 3.8(d) plot the maximum achievable PV efficiency for ARC-coated Si photoelectrodes as a function of bubble volume fraction and plume thickness for bubble diameters D = 1 mm and 100 µm, respectively. Figures 3.8(c) and 3.8(d) demonstrate that the use of an antireflective coating increased the efficiency limits of the photoelectrode. However, the effect of bubbles on PV efficiency still remained significant, especially when the bubbles were small, resulting in large optical losses owing to multiple scattering of the incident rays by the bubbles. Overall, this study established that dealing with bubble-induced optical losses is an important issue to be addressed so as to achieve better photoelectrode performance in PEC cells.

3.4 Conclusion

This chapter presented a comprehensive study to quantify the optical losses caused by the presence of non-absorbing gas bubbles in a semitransparent aqueous electrolyte as well as on the surface of a large Si photoelectrode. The Monte Carlo ray-tracing method was developed and validated to predict (i) the normal-hemispherical reflectance, (ii) the electrolyte absorptance, and (iii) the area-averaged absorptance of the photoelectrode for wavelengths between 400 and 1100 nm. The bubble diameter was found to most significantly affect the total optical losses, followed by the plume thickness, the bubble volume fraction, and the contact surface area coverage. Therefore, the bubble departure diameter should be increased to reduce the optical losses using strategies such as increasing the surface tension of the electrolyte/bubble interface by adding salts, for example. Similarly, the thickness of the bubble plume should be minimized by using shallow electrolyte layer and/or by flowing the electrolyte over the photoelectrode. The use of convection also decreases the bubble volume fraction thereby decreasing the optical losses arising from multiple scattering. The PEC cell should be illuminated from the anode size to mitigate optical losses since the oxygen bubbles have a larger diameter and smaller volume fraction as compared to hydrogen bubbles. Hydrophilic photoelectrode surface with bubble contact angle $\theta_c \approx 20^\circ$ should be preferred to minimize the bubble contact surface area coverage and still ensure a large bubble

departure diameter so as to minimize the optical losses. The use of an antireflective coating on a Si photoelectrode can enhance its performance for large bubbles. However, it is much less effective for high volume fraction of small bubbles since the photon flux reaching the photoelectrode decreases substantially due to bubble scattering. The conclusions reached in this study also apply to tandem configurations where the incident light inevitably interacts with bubbles. The trends reported for efficiency should be qualitatively the same despite the lower transmitted light intensity and the different bandgaps of materials. Overall, significant optical losses incurred at high gas generation rates can prove detrimental to the commercial viability of water splitting in PEC cells. Thus, careful design and operation to control bubble size and ensure fast bubble removal is important.

CHAPTER 4

Review and experimental validation of radiative transfer models for semitransparent media containing bubbles with applications in geoengineering

Many materials manufacturing, photobiochemical, and photoelectrochemical processes involve radiation transfer through foams and bubbly fluids. Controlling and optimizing these processes require accurate predictions of radiation transfer through semitransparent media. Previously developed models treated the heterogeneous media as homogeneous plane-parallel slabs with some effective radiation characteristics while radiation transfer was governed by the one-dimensional radiative transfer equation (RTE). Unfortunately, their accuracy and range of validity remains unclear for lack of comparison with one another or against the same set of experimental data. This chapter critically reviews and assesses the validity of these models both numerically and experimentally. First, predictions of the transmittance and reflectance of heterogeneous slabs containing large randomly distributed bubbles were compared with those obtained from Monte Carlo ray-tracing (MCRT) method based on geometric optics. A new hybrid model was proposed that predicts the effective scattering coefficient and asymmetry factor using the Lorenz–Mie theory and the effective absorption coefficient as the volume-weighted sum of the bubbles and medium absorption coefficients and solves the RTE using the Monte Carlo method. Its predictions showed excellent agreement with those by the MCRT method for a wide range of bubble volume fractions (0%–30%) as well as slab thicknesses (2–40 mm) and medium absorption coefficients (0.1–100 m^{-1}). Second, microcomputed X-ray tomography scans were performed on a fused silica sample containing bubbles with mean radius of 480 µm to retrieve the exact locations, diameters, and total

volume fraction of bubbles. Here also, predictions of the hybrid model using the retrieved data agreed well with experimental measurements of the spectral normal-hemispherical reflectance and transmittance of the sample for wavelengths between 0.4 and 3 μm when silica ranges from weakly absorbing to absorbing.

Having identified the appropriate model, this chapter then investigates the use of seafoam generated in ship wakes to partially counter global radiative forcing, i.e., the energy imbalance caused by the presence of greenhouse gases (GHGs) in the atmosphere. This chapter shows that wake albedo can be substantially increased to about 0.9 by generating seafoam in the wake with controlled bubble size distribution and volume fraction. Such high albedo, combined with extended wake lifetime of several hours that can be achieved using natural ocean-based surfactants, can enable substantial backscattering of solar radiation and counteract part of the radiative forcing caused by the increasing presence of greenhouse gases in the atmosphere.

4.1 Background

Gas bubbles dispersed in a medium significantly change its thermophysical properties including its radiation characteristics [74]. In fact, bubbles substantially affect radiation transfer through a semitransparent medium by scattering the radiation and by increasing the absorption losses by lengthening the mean free path of photons [75]. For example, light scattering by artificial seafoams covering the surface of oceans could potentially minimize absorption of the solar radiation by the Earth's surface by backscattering sunlight [76–78]. Indeed, seafoams are much more reflective than the bare ocean surface and thus appear white [see Figure 4.1(a)] [76]. Given that oceans constitute nearly 71% of the Earth's surface, seafoams offer an efficient way of reducing the Earth's net heat input. However, concerns regarding the long-term effects of ocean albedo manipulation on marine life and ecosystems remain [76].

There are many other applications that deal with radiation transfer through a semitransparent medium containing scatterers. For instance, scattering of solar radiation by gas bubbles trapped in ice sheets could accelerate melting of ice during polar summers [79]. Likewise,

solar water splitting involves generation of hydrogen or oxygen bubbles from semiconductor photoelectrodes immersed in an aqueous electrolyte, as depicted in Figure 4.1(b) [12]. The bubbles scatter the incident sunlight and substantially decrease light absorption and photocurrent generation by the photoelectrode [12, 49, 52, 53, 58, 80]. In glass manufacturing, gas bubbles are generated due to various chemical reactions taking place in the glassmelt [74, 81]. The bubbles rise to the surface and may form a glass foam layer, reducing radiative heat transfer from the combustion space to the glassmelt [82, 83], as illustrated in Figure 4.1(c). Similarly, air bubbles trapped in glass panes used in doors and windows give them a hazy appearance coveted for decorative and privacy purposes, as illustrated in Figure 4.1(d).

It is often difficult to experimentally quantify the effect of bubbles on radiation transfer in the aforementioned situations owing to the complexity in characterizing the gas bubbles. Additionally, the effective radiation characteristics of a semitransparent medium containing gas bubbles cannot be predicted by the Lorenz-Mie theory since it is based on the assumption that the host medium is non-absorbing. This study aims to combine numerical, theoretical, and experimental methods to identify appropriate models capable of accurately predicting radiation transfer through bubble-filled semitransparent slabs [86]. First, the predictions of reflectance and transmittance by different models proposed in the literature were compared with those by the Monte Carlo ray-tracing method based on geometric optics for a large number of bubble volume fractions, slab thicknesses, and absorption coefficients of the continuous phase. Then, the models were experimentally validated by comparing their predictions with the measurements of the spectral normal-hemispherical reflectance and transmittance of a fused silica sample containing gas bubbles in the visible and near infrared. Finally, the most accurate model was used to simulate the interaction of seafoams with solar radiation to calculate their albedo over a day for a wide range of bubble radii and seafoam thicknesses.

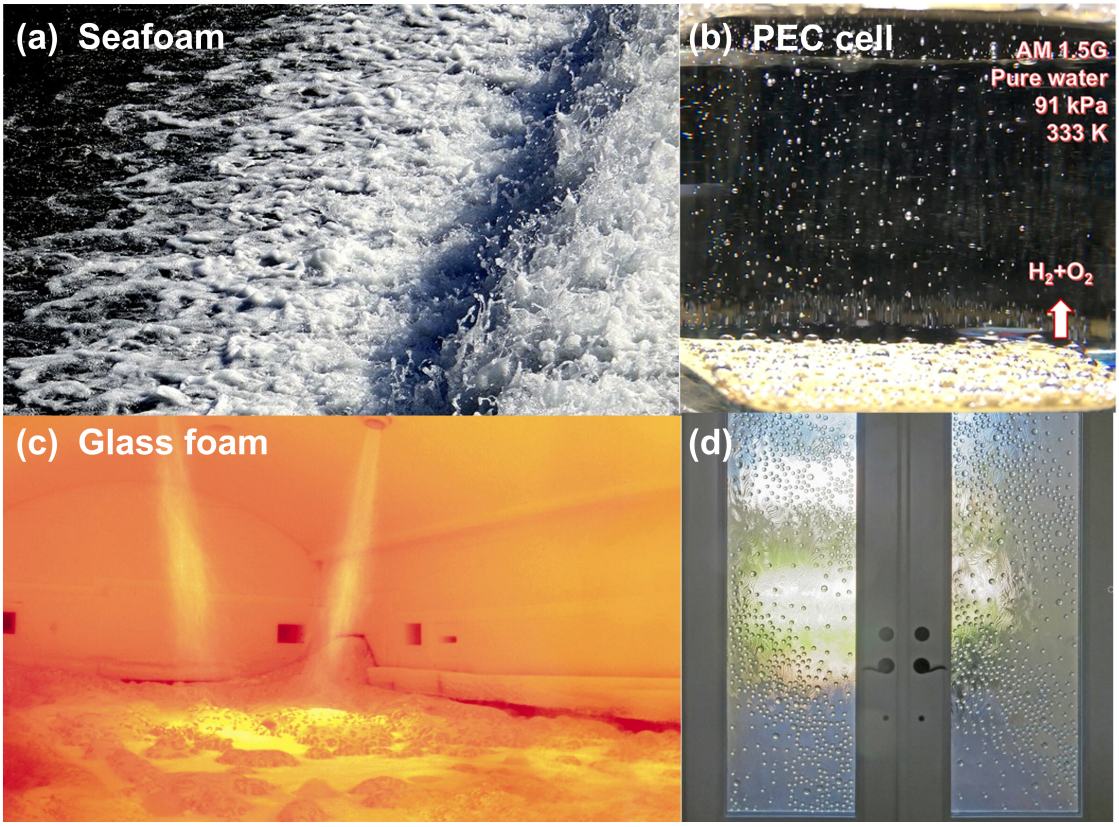

Figure 4.1: Examples of bubbles in semitransparent media interacting with incident radiation in various applications. (a) Seafoams generated to increase the ocean surface albedo and reduce solar absorption of Earth (credit: Stiller Beobachter [22]). (b) Gas bubbles generated during photoelectrochemical water splitting (reprinted with permission from Ref. [84]. Copyright © 2020 American Chemical Society). (c) Foams in glass melting furnaces (credit: http://www.boconline.co.uk). (d) Glass containing bubbles for decorative and privacy purposes in buildings [85].

4.2 Analysis

4.2.1 Problem statement

Let us consider an infinitely long and wide plane-parallel slab of semitransparent continuous medium of thickness H and spectral refractive $n_{c,\lambda}$ and absorption $k_{c,\lambda}$ indices, as illustrated in Figure 4.2. The slab is surrounded by air ($n_{a,\lambda} = 1$) and contains randomly distributed polydisperse spherical and non-absorbing gas bubbles of refractive index $n_{d,\lambda} = 1.0$ occu-

pying a volume fraction f_v and having normal size distribution $f(\bar{r}, \sigma)$ with mean radius $\bar{r}$ and standard deviation σ. The heterogeneous slab is subjected to collimated and normally incident radiation of wavelength λ. The bubbles are much larger than the wavelength λ so that geometric optics prevails while dependent scattering effects can be neglected due to the large interbubble distance compared with the wavelength [87]. The slab thickness and/or the bubble volume fraction are sufficiently large such that multiple scattering occurs. Bubbles scatter the radiation strongly forward such that a fraction of the incident intensity is transmitted through the slab in various directions, as quantified by the normal-hemispherical transmittance $T_{nh,\lambda}$. The remaining incident radiation is either back-scattered, as accounted for by the normal-hemispherical reflectance $R_{nh,\lambda}$, or absorbed by the continuous phase, as represented by the absorptance $A_{n,\lambda}$. Overall, an energy balance on the incident radiation can be written as $R_{nh,\lambda} + A_{n,\lambda} + T_{nh,\lambda} = 1$.

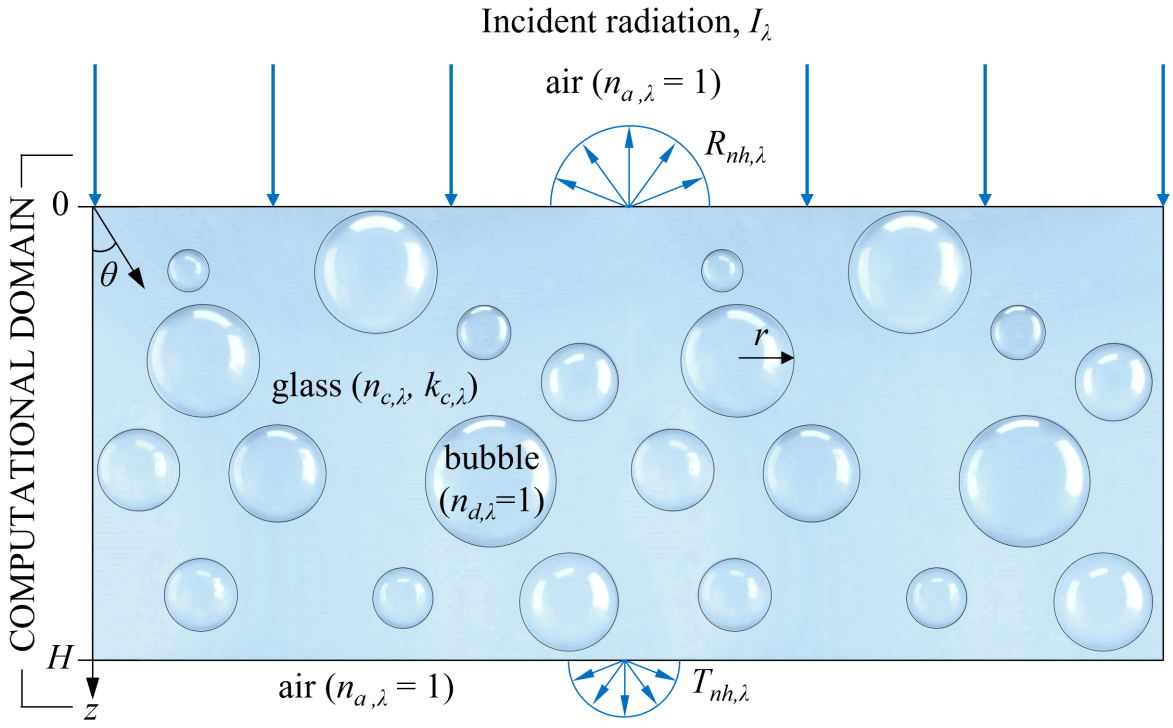

Figure 4.2: Schematic of a plane-parallel slab of semitransparent medium ($n_{c,\lambda}$, $k_{c,\lambda}$) containing randomly distributed polydisperse spherical gas bubbles ($n_{d,\lambda} = 1$) and exposed to normally incident radiation.

4.3 Radiative Transfer Models

Most studies investigating radiation transfer through absorbing media containing spherical particles (or bubbles) have modeled them as homogeneous with some effective radiation characteristics κ_λ, $\sigma_{s,\lambda}$, and $\Phi_\lambda(\theta', \theta)$ assuming independent scattering [88–98], as reviewed in the next sections.

4.3.0.1 Fedorov-Viskanta model

Fedorov and Viskanta [93, 94] developed a theoretical framework for predicting radiation transfer through glass foams consisting of monodisperse bubbles of radius r with volume fraction $f_v \leq 0.74$. First, the effective scattering $\sigma_{s,\lambda}$ and absorption κ_λ coefficients of a layer of foams made of monodisperse bubbles were based on the anomalous diffraction theory and given by [99]

$$\sigma_{s,\lambda} = 0.75 Q^d_{sca,\lambda} \frac{f_v}{r} \quad \text{and} \quad \kappa_\lambda = \frac{4\pi k_{c,\lambda}}{\lambda} - 0.75(Q^c_{abs,\lambda} - Q^d_{abs,\lambda})\frac{f_v}{r}. \tag{4.1}$$

The expression of the effective absorption coefficient κ_λ was obtained by subtracting the absorption coefficient of spherical glass particles in air from that of a glass slab and adding the absorption coefficient of spherical gas bubbles in glass using their respective absorption efficiency factors $Q^c_{abs,\lambda}$ and $Q^d_{abs,\lambda}$ given by [99]

$$Q^d_{abs,\lambda} = 1 + \frac{e^{-2\rho_d tan(y_d)}}{\rho_d tan(y_d)} + \frac{e^{-2\rho_d tan(y_d)} - 1}{2[\rho_d tan(y_d)]^2}, \tag{4.2}$$

$$Q^c_{abs,\lambda} = 1 + \frac{e^{-2\rho_c tan(y_c)}}{\rho_c tan(y_c)} + \frac{e^{-2\rho_c tan(y_c)} - 1}{2[\rho_c tan(y_c)]^2}, \tag{4.3}$$

where ρ_d and ρ_c are the Van de Hulst's normalized size parameters defined as [99]

$$\rho_{d,\lambda} = \frac{4(n_d - 1)\pi r}{\lambda} \quad \text{and} \quad \rho_{c,\lambda} = \frac{4(n_c - 1)\pi r}{\lambda}. \tag{4.4}$$

The corresponding normalized absorption parameters y_d and y_c were given by [99]

$$y_{d,\lambda} = tan^{-1}\left(\frac{k_d}{n_d - 1}\right) \quad \text{and} \quad y_{c,\lambda} = tan^{-1}\left(\frac{k_c}{n_c - 1}\right). \tag{4.5}$$

Additionally, the extinction efficiency factor $Q^d_{ext,\lambda}$ of a bubble in glass was expressed by [99]

$$\begin{aligned} Q^d_{ext,\lambda} = 2 - 4\frac{cos(y_d)}{\rho_d}\left[e^{-\rho_d tan(y_d)} sin(\rho_d - y_d)\right] \\ + 4\left[\frac{cos(y_d)}{\rho_d}\right]^2 \left[cos(2y_d) - e^{-\rho_d tan(y_d)} cos(\rho_d - 2y_d)\right]. \end{aligned} \tag{4.6}$$

The corresponding scattering efficiency factor of a bubble in glass $Q^d_{sca,\lambda}$ was written as

$$Q^d_{sca,\lambda} = Q^d_{ext,\lambda} - Q^d_{abs,\lambda}. \tag{4.7}$$

Finally, the RTE was solved using the two-flux approximation method to obtain closed form analytical expressions for the normal-hemispherical transmittance $T_{nh,\lambda}$, reflectance $R_{nh,\lambda}$, and absorptance $A_{n,\lambda}$ of an absorbing and scattering glass slab containing bubbles. The model assumed isotropic radiation field inside the glass slab owing to the large bubble volume fraction. Therefore, the model calculated the reflectance at the glass slab/air interface using a correlation applicable for any diffuse media-to-air interface [100, 101]. The reflectance at air/glass slab interface was calculated using Fresnel's equation [37]. In the present study, the glass slabs containing gas bubbles were free-standing with air on both sides and the interface reflectances were calculated accordingly.

4.3.0.2 Dombrovsky model

Dombrovsky et al. [95, 96] used Lorenz-Mie theory to calculate the spectral transport scattering $Q^{tr}_{sca,\lambda}$ and absorption $Q_{abs,\lambda}$ efficiency factors of large bubbles of size parameter $\chi_d = 2\pi r/\lambda$ embedded in a semitransparent medium of complex refractive index $m_{c,\lambda} = n_{c,\lambda} + ik_{c,\lambda}$ given by

$$Q^{tr}_{sca,\lambda} = 0.9(n_{c,\lambda} - 1) \quad \text{and} \quad Q_{abs,\lambda} = -\frac{8}{3} k_{c,\lambda} \chi_d. \tag{4.8}$$

The effective scattering $\sigma_{s,\lambda}$, transport scattering $\sigma^{tr}_{s,\lambda}$, and absorption κ_λ coefficients of the heterogeneous medium were given by [95]

$$\sigma_{s,\lambda} = \frac{3f_v}{2r}, \quad \sigma^{tr}_{s,\lambda} = 0.675(n_{c,\lambda} - 1)\frac{f_v}{r}, \quad \text{and} \quad \kappa_\lambda = (1 - f_v)\kappa_{c,\lambda} \tag{4.9}$$

where $\kappa_{c,\lambda} = 4\pi k_{c,\lambda}/\lambda$ is the absorption coefficient of the continuous semitransparent medium. In addition, the authors used the so-called "transport approximation" to simplify the radia-

tive transfer equation by replacing the scattering phase function by a sum of the isotropic component and the term denoting the peak of forward scattering given by [102, 103]

$$\Phi_{\lambda}^{tr}(\theta_0) = 1 - g_{\lambda} + 2g_{\lambda}\delta(1 - \cos\theta_0), \tag{4.10}$$

where δ is the Kronecker-delta function, θ_0 is the angle between the radiation incident on the scatterer along direction $\mu' = \cos\theta'$ and the intensity scattered in direction $\mu = \cos\theta$. The asymmetry factor g_{λ} was given by [95]

$$g_{\lambda} = 1 - 0.45(n_{c,\lambda} - 1). \tag{4.11}$$

The RTE was then solved using the modified two-flux approximation method accounting for boundary reflections at the surfaces of the plane-parallel slab surrounded by air. Analytical expressions for $T_{nh,\lambda}$ and $R_{nh,\lambda}$ were derived. The authors reported an error of less than 5% when compared with the numerical calculations based on the composite discrete ordinate method for the range of size parameter $20 \ll \chi_d \ll 1/(2k_{c,\lambda})$.

4.3.0.3 Modified Lorenz-Mie theory

Yang et al. [97] established that the scattering and extinction efficiencies of a spherical particle embedded in an absorbing medium presented by Sudiarta et al. [90] and Fu et al. [91] were inherent properties derived from the near-field at the particle surface. Yang et al. [97] further noted that the corresponding scattering and extinction cross-sections could not be calculated by multiplying these efficiencies with the geometric projected area of the spherical particle since the host medium was absorbing. Therefore, the authors derived the expressions for apparent scattering and absorption cross-sections based on the far-field information to determine the effective radiation characteristics [97]. The apparent scattering cross-section was scaled by a factor $e^{\kappa_{c,\lambda}r}$ to facilitate radiative transfer calculations involving a polydisperse particle system. This scaled apparent scattering cross-section was used to determine the effective scattering coefficient $\sigma_{s,\lambda}$ of a semitransparent glass slab containing gas bubbles. The corresponding effective absorption coefficient κ_{λ} was equal to the absorption coefficient of glass $\kappa_{c,\lambda}$ regardless of the volume fraction f_v of bubbles [97]. The asymmetry parameter

g_λ was the same as that predicted by Lorenz-Mie theory for bubbles in a non-absorbing medium. These radiation characteristics were input into a 1D RTE solver based on the Monte Carlo ray-tracing method to calculate the normal-hemispherical reflectance R_{nh} and transmittance T_{nh} while also accounting for boundary reflections at air/glass slab interfaces.

4.3.0.4 Hybrid model

Here, we propose a hybrid model in which (i) the effective scattering coefficient $\sigma_{s,\lambda}$ and asymmetry factor g_λ of the heterogeneous medium were predicted by the Lorenz-Mie theory assuming the continuous medium was non-absorbing and (ii) the effective absorption coefficient κ_λ was expressed as a weighted sum of the absorption coefficients of the dispersed and continuous phases as used in the literature [95, 104]

$$\kappa_\lambda = (1 - f_v)\kappa_{c,\lambda}. \tag{4.12}$$

The Henyey-Greenstein phase function was used to model the scattering phase function using the asymmetry parameter g_λ. Yalcin et al. [105] developed a code available online [106] that computes these radiation characteristics and predicts the normal-hemispherical reflectance R_{nh} and transmittance T_{nh} by solving the one-dimensional RTE [Equation (1.4)] using the Monte Carlo method. The code also accounts for reflection and refraction at the boundaries of the plane-parallel heterogeneous slab. Typically, about 10^6 rays are necessary to achieve numerical convergence.

The objective of the study is to assess the validity of the above theoretical models for simulating radiation transfer in semitransparent media containing large gas bubbles. To do so, predictions of the effective radiation characteristics κ_λ, $\sigma_{s,\lambda}$, and $\Phi_\lambda(\theta', \theta)$ of a glass sample containing bubbles as well as its normal-hemispherical reflectance $R_{nh\lambda}$ and transmittance $T_{nh\lambda}$ predicted by the different models were compared with those predicted by the Monte Carlo ray-tracing method based on geometric optics. Furthermore, experimental measurements of the spectral normal-hemispherical reflectance $R_{nh\lambda}$ and transmittance $T_{nh\lambda}$ of a thick fused silica sample containing bubbles between 0.4 and 3 µm were compared with predictions by the different models as well as by the Monte Carlo ray-tracing method for the

sample's digital twin generated from microcomputed X-ray tomography (microCT) scans. Finally, spectral simulations were performed over the solar spectrum using the most accurate model to compute the spectral normal-hemispherical reflectance of seafoams containing microbubbles covering ocean surface for different solar zenith angles. The predicted reflectance was integrated over the day to determine the albedo.

4.4 Materials and methods

4.4.1 Glass sample containing bubbles

A glass sample made of Osram Sylvania SG25 Lightning grade fused silica and containing gas bubbles was analyzed [107]. The sample was cut with a diamond saw from a large piece of fused silica collected during shutdown of a glass melting furnace [107]. The sample had a thickness of 10 mm and a 43 mm × 38 mm cross-section. The gas bubbles were spherical and appeared to be randomly distributed in the sample. The optical properties ($n_{c,\lambda}$, $k_{c,\lambda}$) of fused silica were obtained from Refs. [107–109].

4.4.2 Bubble characterization

To characterize the bubbles present in the glass sample, microCT scans were performed on the CrumpCAT scanner at UCLA Crump Institute of Molecular Imaging having a resolution of 125 µm. The scans achieved excellent contrast between the bubbles and the glass [see flythrough video in Supplementary Material] which allowed them to be easily distinguished during post-processing. The scans also confirmed that the bubbles were spherical owing to the high surface tension of glassmelt. Any conjoined bubbles were separated by fitting two separate spheres. The diameter and coordinates of each bubble were extracted from the tomographic data using the open-source medical imaging data analysis software AMIDE [110]. The normal size distribution $f(\bar{r}, \sigma)$ was fitted to be used in the radiation transfer models previously described.

4.4.3 Reflectance and transmittance measurements

A double-beam ultraviolet-visible (UV-Vis) spectrophotometer (Evolution^{TM} 220, Thermo Scientific Fisher, USA) equipped with an integrating sphere (Evolution^{TM} ISA-200 Integrating Sphere Accessory, Thermo Scientific Fisher, USA) was used for measuring the normal-hemispherical reflectance $R_{nh,\lambda}$ and transmittance $T_{nh,\lambda}$ of the glass sample containing bubbles over the wavelength range 0.4 to 1 µm when glass is transparent. The diameter of the spectrophotometer beam was relatively small compared to the sample dimensions (43 mm × 38 mm). Therefore, measurements were taken at 10 different locations over the sample surface to correct for local variations in bubble volume fraction. A similar procedure was repeated for the measurements of reflectance $R_{nh,\lambda}$ and transmittance $T_{nh,\lambda}$ over the 2 to 3 µm spectral range when glass is absorbing. The measurements were performed on a nitrogen-purged Fourier transform infrared (FTIR) spectrometer (Nicolet^{TM} iS50, Thermo Scientific Fischer, USA) equipped with an MCT detector and a KBr beamsplitter, along with an integrating sphere (Upward IntegratIR^{TM}, PIKE Technologies, USA).

4.5 Results and discussion

4.5.1 Validation of models

Figure 4.3 shows a flowchart detailing the different methods and models used in this study to predict the spectral normal-hemispherical reflectance $R_{nh,\lambda}$, transmittance $T_{nh,\lambda}$, and absorptance $A_{n,\lambda}$ of a fused silica glass slab containing bubbles. The bubbles were non-absorbing and had a refractive index $n_{d,\lambda} = 1.0$, volume fraction f_v, and size distribution $f(\bar{r}, \sigma)$. Predictions by the different models were evaluated against those by the Monte Carlo ray-tracing method, as previously described.

4.5.1.1 Effective radiation characteristics

Figure 4.4 compares the effective spectral (a) scattering $\sigma_{s,\lambda}$ and (b) absorption κ_λ coefficients as functions of wavelength λ as predicted by the four different models for monodisperse

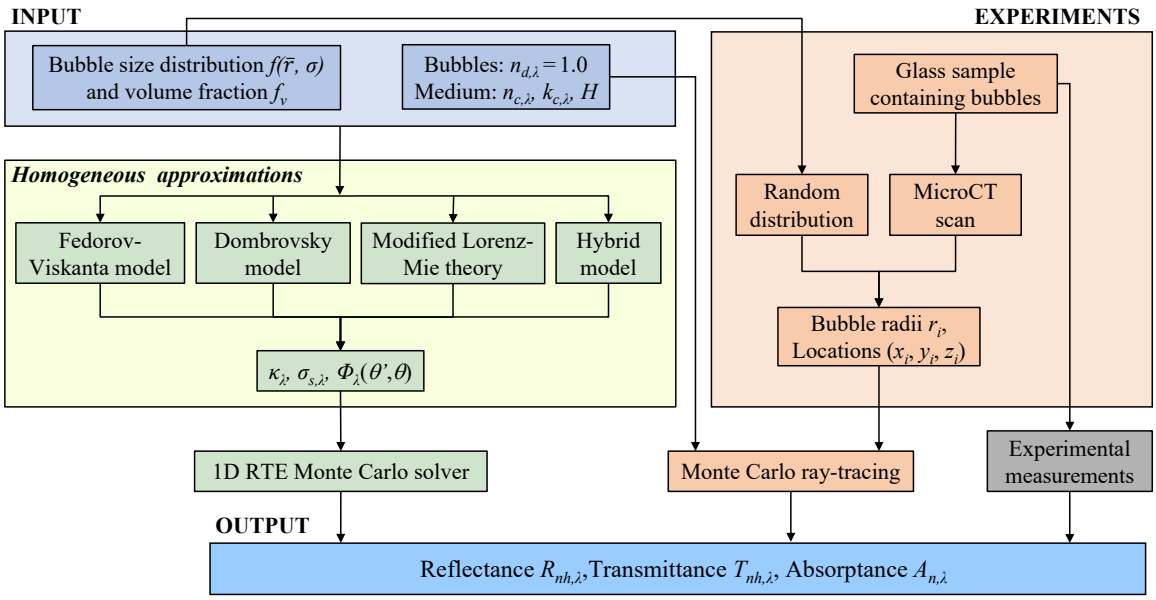

Figure 4.3: Different numerical, theoretical, and experimental approaches to determine the spectral normal-hemispherical reflectance $R_{nh,\lambda}$, transmittance $T_{nh,\lambda}$, and absorptance $A_{n,\lambda}$ of semitransparent media containing gas bubbles.

bubbles of radius $r = 0.5$ mm and volume fraction $f_v = 20\%$. Figure 4.4(a) shows that the effective scattering coefficient $\sigma_{s,\lambda}$ predicted by the hybrid model and by the Dombrovsky model [see Equation (4.9)] remained nearly constant over the spectral range considered. This can be attributed to the large size parameter that caused the scattering and extinction efficiency factors $Q^d_{ext} = Q^d_{sca}$ to reach a value of 2 [37]. The predictions of $\sigma_{s,\lambda}$ by the modified Lorenz-Mie theory agreed well with those by the Lorenz-Mie theory. However, the predicted scattering coefficient $\sigma_{s,\lambda}$ exhibited a peak when absorption by the host medium peaked at around $\lambda = 2.73$ µm. Such a behavior seems erroneous and may be attributed to the large bubble radius r that increased the magnitude of the exponential scaling factor $e^{\kappa_{c,\lambda} r}$ used in the modified Lorenz-Mie theory model. On the other hand, the effective scattering coefficient predicted by the Fedorov-Viskanta model oscillated around the predictions by the Lorenz-Mie theory. Such oscillations can be attributed to wave effects captured by the anomalous diffraction theory [99].

Figure 4.4(b) shows that predictions of the effective absorption coefficients κ_λ by the hy-

brid model, the Dombrovsky model, and the Fedorov-Viskanta model were all in agreement. However, predictions by the modified Lorenz-Mie theory were uniformly larger than the other models by 25% at all wavelengths since it considered $\kappa_\lambda = \kappa_{c,\lambda}$ instead of $\kappa_\lambda = \kappa_{c,\lambda}(1 - f_v)$. Figure 4.4(b) also highlights that the medium was weakly absorbing up to $\lambda = 2$ µm. Beyond that wavelength, the absorption of the medium consistently increased, exhibiting an absorption peak at about $\lambda = 2.73$ µm.

4.5.1.2 Effect of volume fraction f_v

Figure 4.5 compares the normal-hemispherical (a) reflectance $R_{nh,\lambda}$ and (b) transmittance $T_{nh,\lambda}$ predicted as functions of bubble volume fraction f_v by the four different models for monodisperse bubbles of radius $r = 0.5$ mm, slab thickness $H = 10$ mm, and wavelength $\lambda = 2$ µm when the medium was weakly absorbing ($k_{c,\lambda} = 7.3 \times 10^{-7}$). Similarly, Figures 4.5(c) and 4.5(d) respectively present the normal-hemispherical reflectance $R_{nh,\lambda}$ and transmittance $T_{nh,\lambda}$ but at wavelength $\lambda = 2.73$ µm when the medium was significantly more absorbing ($k_{c,\lambda} = 3.27 \times 10^{-5}$). Figure 4.5 shows that all the models predicted a similar trend of increasing reflectance $R_{nh,\lambda}$ and decreasing transmittance $T_{nh,\lambda}$ with increasing bubble volume fraction f_v for both wavelengths considered. It also shows that the Fedorov-Viskanta model consistently overpredicted the reflectance $R_{nh,\lambda}$ and underestimated the transmittance $T_{nh,\lambda}$ for all volume fractions considered. This can be attributed to the fact that the Fedorov-Viskanta model assumed isotropic radiation field inside the medium to calculate the reflectance of medium/air interface [93]. Such an assumption is valid for foams that have bubble volume fraction $f_v \sim 74\%$ but may not be realistic for smaller f_v. Interestingly, the predictions by the Dombrovsky model were in agreement with those by the MCRT method at wavelength $\lambda = 2$ µm when fused silica was weakly absorbing. However, the model overestimated considerably the transmittance $T_{nh,\lambda}$ as well as the reflectance $R_{nh,\lambda}$ at $\lambda = 2.73$ µm when fused silica was more absorbing. Similarly, the predictions of reflectance $R_{nh,\lambda}$ and transmittance $T_{nh,\lambda}$ by the modified Lorenz-Mie theory agreed well with those by the MCRT method for a weakly absorbing glass medium at wavelength $\lambda = 2$ µm. However, when the medium was more absorbing at $\lambda = 2.73$ µm, the predictions of transmittance $T_{nh,\lambda}$ were

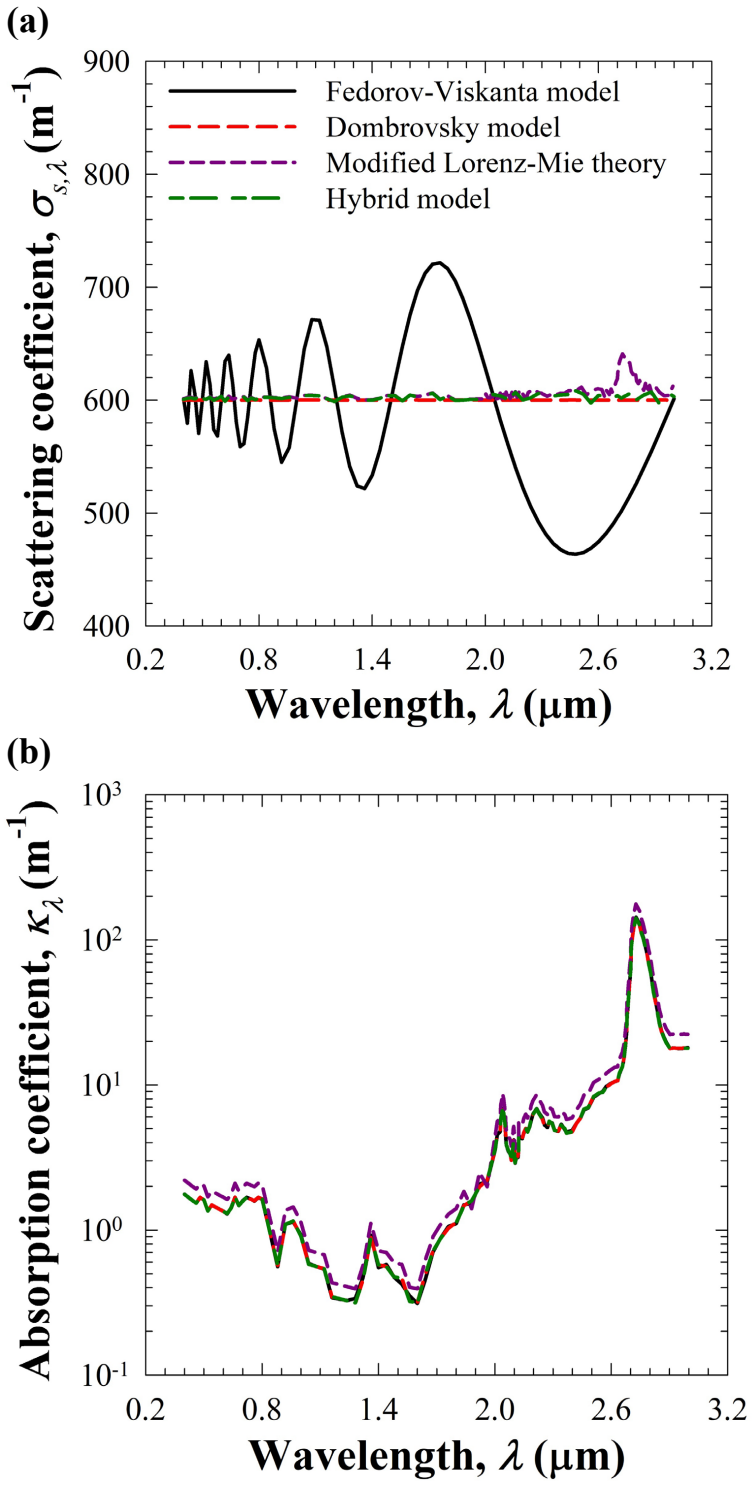

Figure 4.4: Comparison of the effective spectral (a) scattering $\sigma_{s,\lambda}$ and (b) absorption κ_λ coefficients predicted by four different models as functions of the wavelength of incident radiation for monodisperse bubbles of radius $r = 0.5$ mm and volume fraction $f_v = 20\%$.

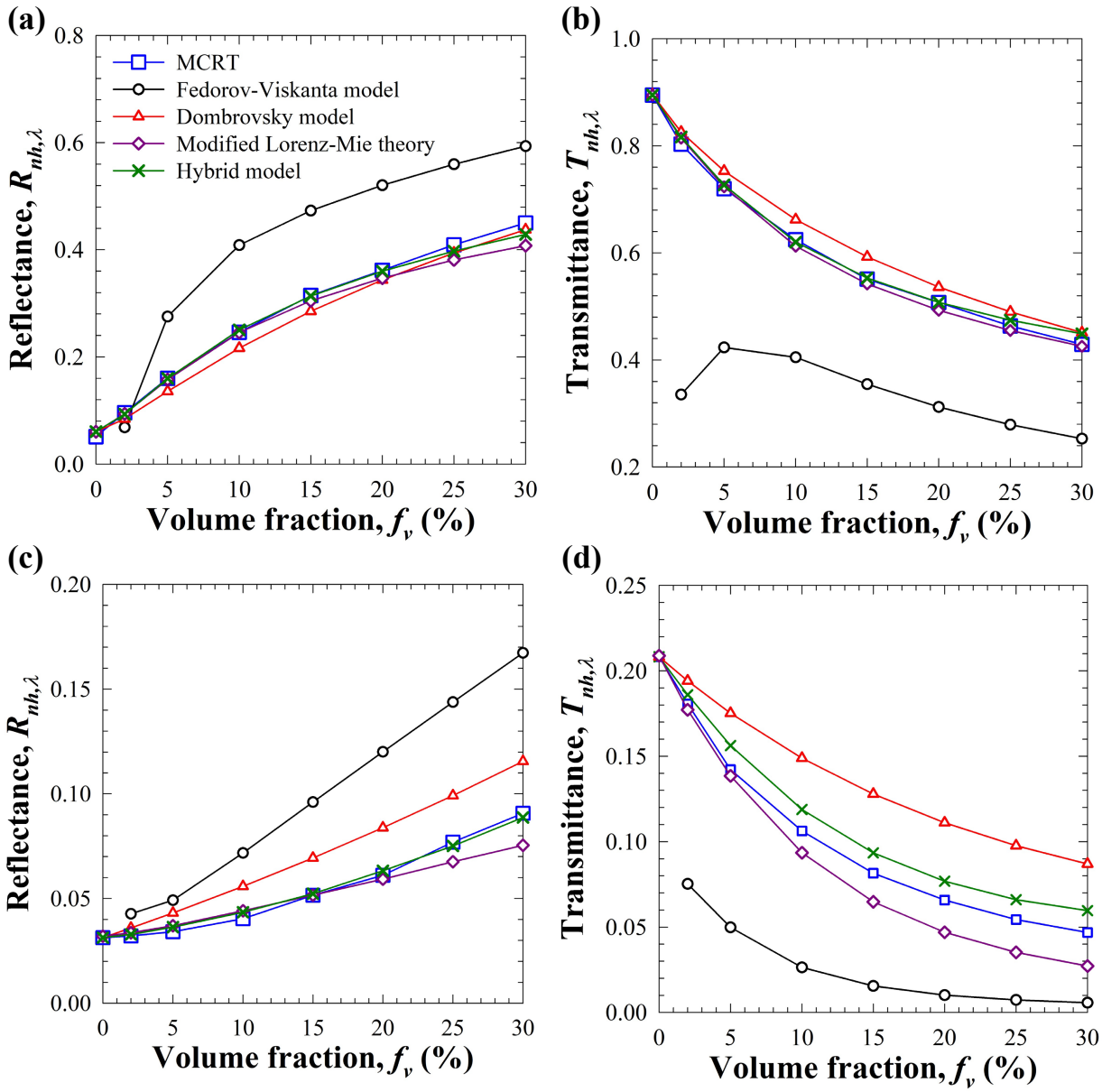

Figure 4.5: Comparison of predictions of the normal-hemispherical reflectance $R_{nh,\lambda}$ and transmittance $T_{nh,\lambda}$ as functions of bubble volume fraction f_v for (a)-(b) wavelength $\lambda = 2$ μm when fused silica was weakly absorbing and (c)-(d) at $\lambda = 2.73$ μm when fused silica was more absorbing. The bubbles were monodisperse with radius $r = 0.5$ mm and the slab's thickness was $H = 10$ mm. Predictions by the MCRT method are used as reference.

slightly smaller than those predicted by the MCRT method. This deviation can also be attributed to the fact that the modified Lorenz-Mie theory did not take into account the bubble volume fraction f_v for predicting the effective absorption coefficient κ_λ of the glass slab containing bubbles, as previously discussed. Finally, Figure 4.5 establishes that the predictions of $R_{nh,\lambda}$ and $T_{nh,\lambda}$ by the hybrid model were in excellent agreement with those by the MCRT method for all volume fractions and for both wavelengths considered.

4.5.1.3 Effect of continuous phase absorption coefficient $\kappa_{c,\lambda}$

Figure 4.6 compares the predictions of the normal-hemispherical (a) reflectance $R_{nh,\lambda}$ and (b) transmittance $T_{nh,\lambda}$ by the four different models against predictions by the MCRT method as functions of the absorption coefficient $\kappa_{c,\lambda}$ of the continuous phase for monodisperse bubbles of radius $r = 0.5$ mm and volume fraction $f_v = 20\%$ in a slab of thickness $H = 10$ mm. Here again, the Fedorov-Viskanta model overestimated the reflectance $R_{nh,\lambda}$ and underestimated the transmittance $T_{nh,\lambda}$ as compared with predictions by the MCRT method. The Dombrovsky model slightly overestimated the transmittance $T_{nh,\lambda}$ by an absolute error of about 6% while the predicted reflectance $R_{nh,\lambda}$ fell within an absolute difference of 5% of that predicted by the MCRT method for all absorption coefficients $\kappa_{c,\lambda}$ considered. The predictions of $R_{nh,\lambda}$ and $T_{nh,\lambda}$ by the modified Lorenz-Mie theory agreed well with those by the MCRT method for small absorption coefficients such that $\kappa_{c,\lambda} \leq 5$ m^{-1}. However, for larger absorption coefficients, the predicted transmittance $T_{nh,\lambda}$ was slightly smaller than that predicted by the MCRT method. On the other hand, the hybrid model accurately predicted the reflectance $R_{nh,\lambda}$ and transmittance $T_{nh,\lambda}$ for the range of absorption coefficients $\kappa_{c,\lambda}$ between 10^{-1} to around 10^2. This model was able to accurately predict radiation transfer in a semitransparent medium containing bubbles when absorption was negligible and scattering dominated, and also when absorption dominated and scattering was negligible. In the latter case, potential errors made in predicting the effective scattering coefficient $\sigma_{s,\lambda}$ had no effect in the predictions of $R_{nh,\lambda}$ and $T_{nh,\lambda}$.

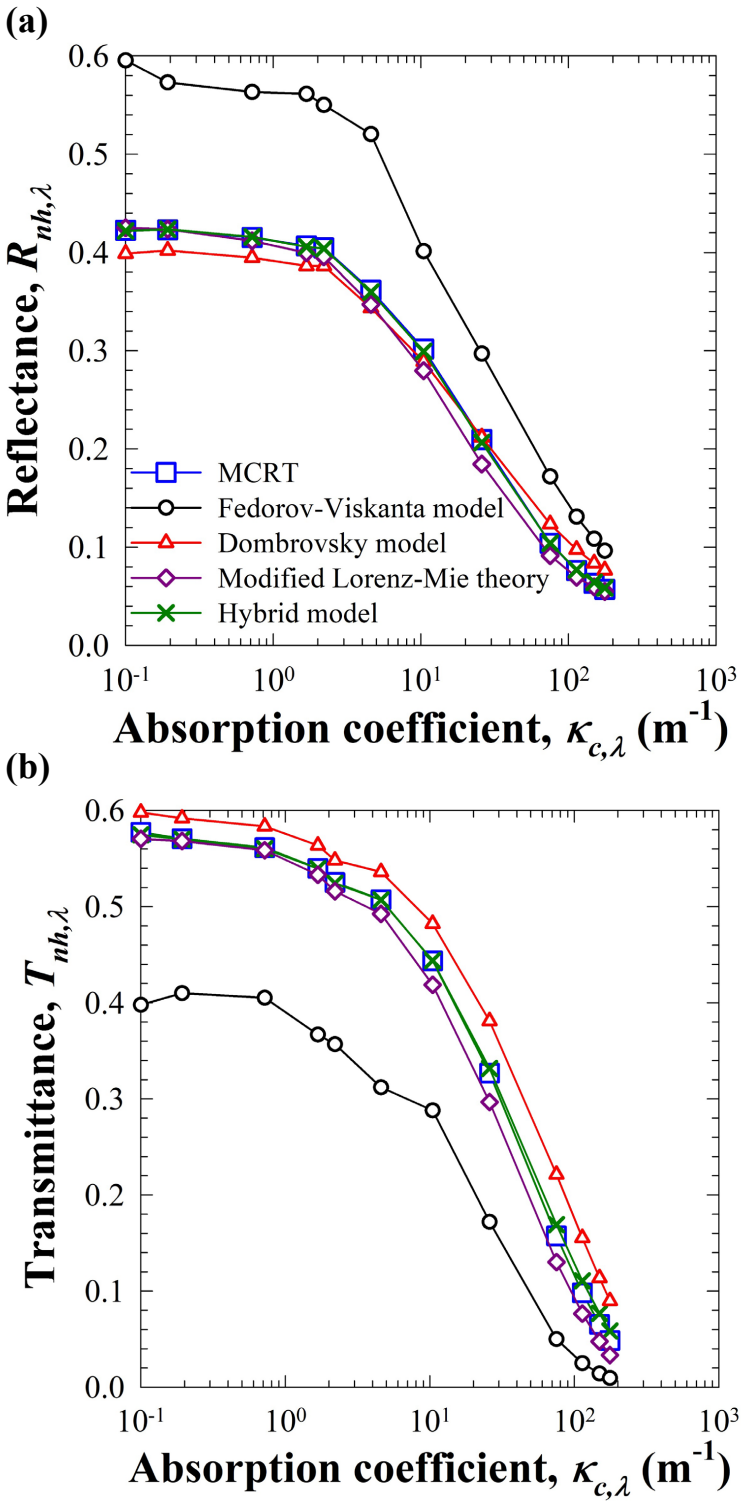

Figure 4.6: Comparison of predictions of the normal-hemispherical (a) reflectance $R_{nh,\lambda}$ and (b) transmittance $T_{nh,\lambda}$ as functions of continuous phase absorption coefficient $\kappa_{c,\lambda}$. The bubbles were monodisperse with radius $r = 0.5$ mm and volume fraction $f_v = 20\%$ while the slab's thickness was $H = 10$ mm.

4.5.1.4 Effect of slab thickness H

Figure 4.7 compares the normal-hemispherical (a) reflectance $R_{nh,\lambda}$ and (b) transmittance $T_{nh,\lambda}$ predicted by the four different models as functions of the slab's thickness H for monodisperse bubbles of radius $r = 0.5$ mm and volume fraction $f_v = 20\%$ at wavelength $\lambda = 2$ µm. Here again, the Fedorov-Viskanta model overestimated $R_{nh,\lambda}$ and underestimated $T_{nh,\lambda}$ for all thicknesses H considered except for $H < 5$ mm. In addition, the Dombrovsky model slightly underestimated the reflectance $R_{nh,\lambda}$ for thickness $H < 15$ mm but overpredicted it as the thickness increased. However, its predictions of transmittance $T_{nh,\lambda}$ agreed reasonably well with the predictions by the MCRT method for all thicknesses. Similarly, the modified Lorenz-Mie theory slightly underestimated the reflectance $R_{nh,\lambda}$ and transmittance $T_{nh,\lambda}$ as the slab thickness increased due to its overestimation of the effective absorption coefficient κ_λ. Finally, the reflectance $R_{nh,\lambda}$ and transmittance $T_{nh,\lambda}$ predicted by the hybrid model were in excellent agreement with those predicted by the MCRT method even for sample thicknesses on the same order of magnitude as the bubble radius. This may seem surprising because defining effective radiation characteristics may not be valid for such small thicknesses given the few bubbles interacting with the incident light. However, the simulated samples had infinite cross-sectional area thanks to the periodic boundary conditions. Thus, averaging was achieved over a large surface area. Similar considerations were made experimentally by using a wide beam compared with the sample thickness [107].

4.5.1.5 Comparison with experimental measurements

Bubble characterization

Figure 4.8 shows (a) the photograph of the sample's top view with (b) the corresponding image of the sample's digital twin created from microCT scans, indicating an excellent 3D reconstruction. Figure 4.8(c) shows a screenshot from the user interface of imaging software AMIDE, highlighting the identified bubbles in the sample at a depth of 7 mm from the top of the sample. Finally, Figure 4.8(d) shows the retrieved bubble size distribution from the 636 bubbles contained in the sample with the best fit provided by a normal distribution with

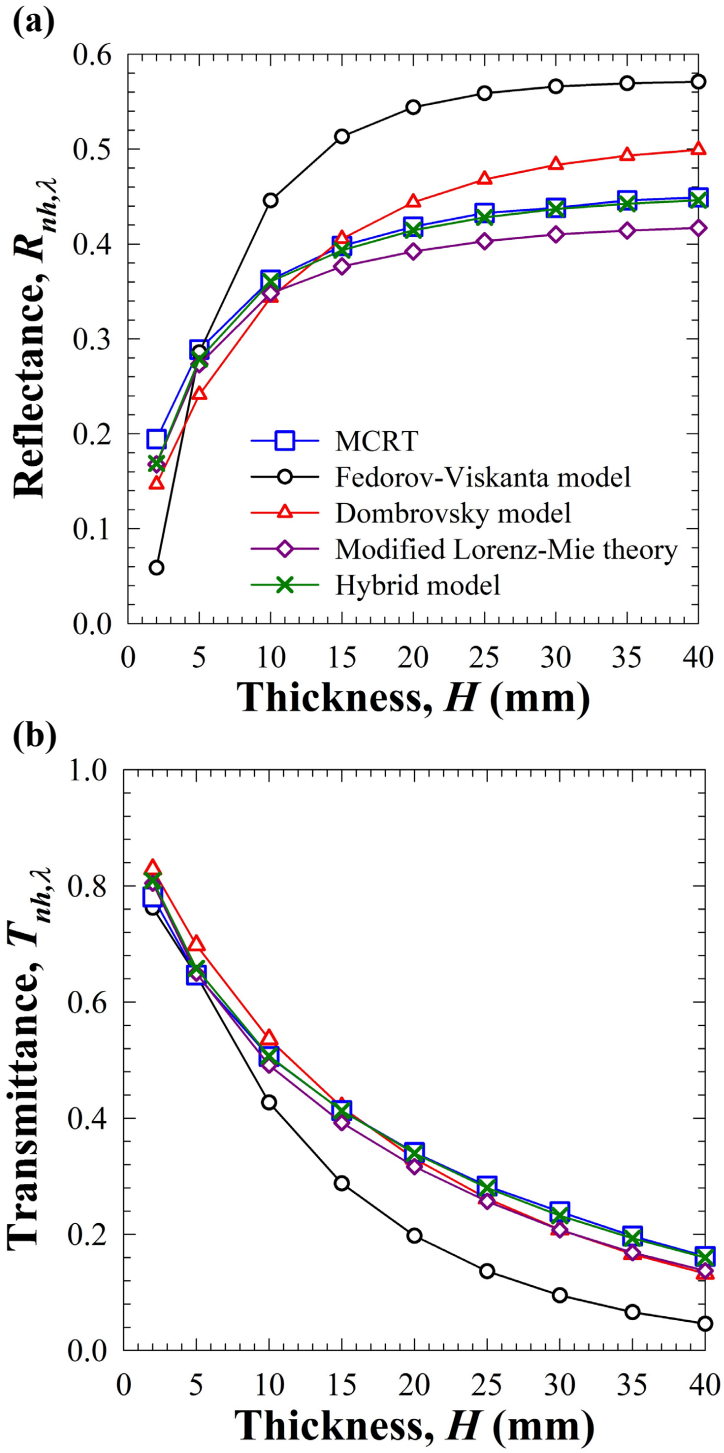

Figure 4.7: Comparison of predictions of the normal-hemispherical (a) reflectance $R_{nh,\lambda}$ and (b) transmittance $T_{nh,\lambda}$ as functions of slab's thickness H for monodisperse bubbles of radius $r = 0.5$ mm and volume fraction $f_v = 20\%$ at wavelength $\lambda = 2$ µm.

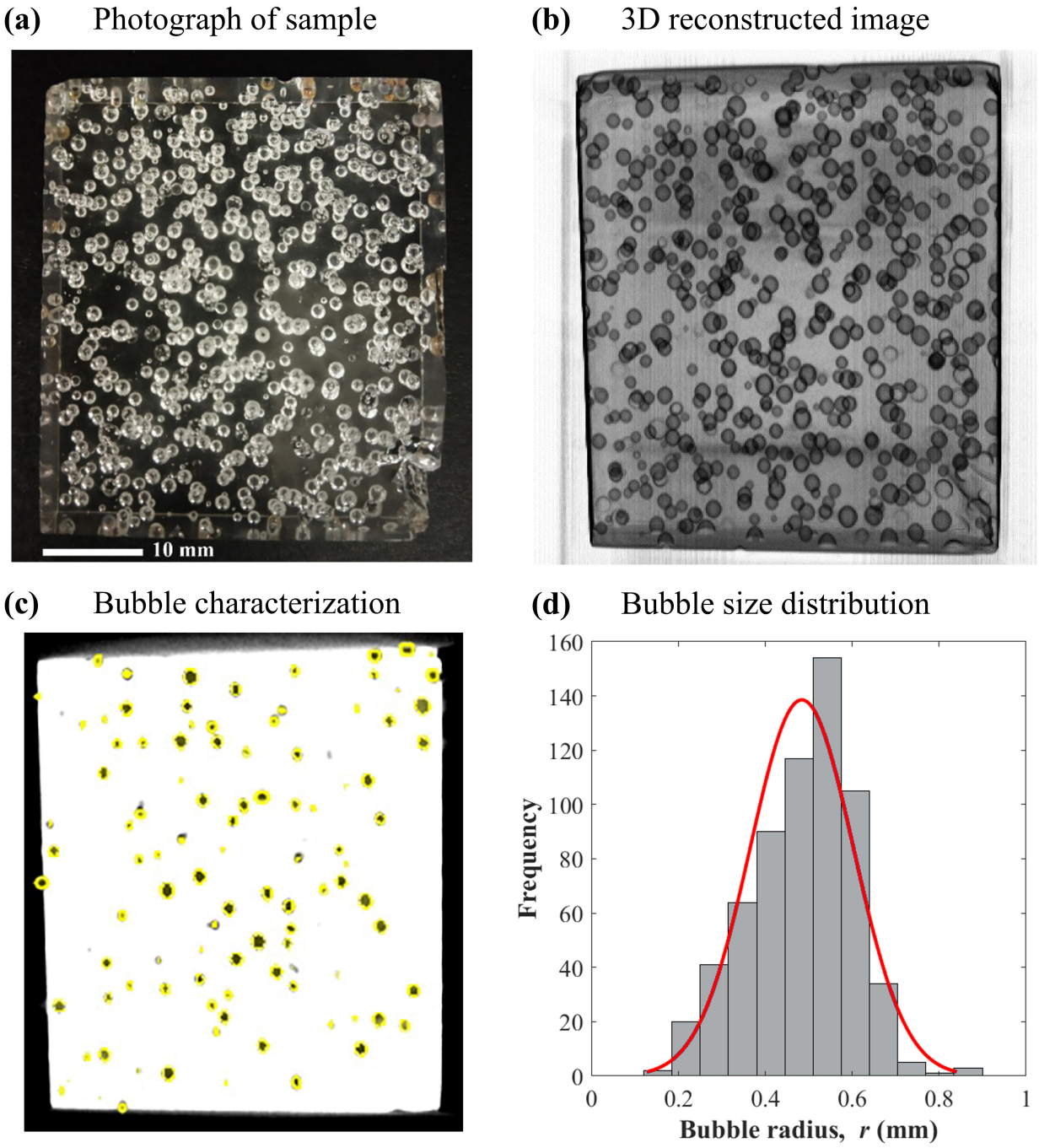

Figure 4.8: (a) Photograph of the glass sample containing gas bubbles and (b) its 3D reconstructed image obtained from microcomputed X-ray tomography. (c) The radius and location of each bubble was identified using medical imaging software AMIDE. (d) Retrieved bubble size distribution fitted with a normal distribution $f(\bar{r}, \sigma)$ with mean bubble radius $\bar{r} = 0.48$ mm and standard deviation $\sigma = 0.12$ mm.

a mean bubble radius $\bar{r} = 0.48$ mm and standard deviation $\sigma = 0.12$ mm. The total bubble volume fraction f_v in the sample was determined to be 2%.

The sample was sufficiently thick and the bubble volume fraction large enough for multiple scattering to prevail. Thus, the selected sample and the selected wavelength range captured different light transfer phenomena such as absorption and multiple scattering. However, retrieving the location and size distribution of the bubbles was challenging because the microCT scans had multiple slices containing portions of the same bubble which prevented the use of image processing programs that use Hough circle transform to quickly extract circular objects from a single slice. Instead, medical imaging tools that can identify and characterize volumes from microCT scans were necessary. However, most open source medical imaging tools did not automatically detect the volumes and required manual identification which was challenging and tedious when dealing with a large number of scattering bubbles.

Normal-hemispherical reflectance and transmittance

Figure 4.9 compares the experimental measurements of the normal-hemispherical (a) reflectance $R_{nh,\lambda}$ and (b) transmittance $T_{nh,\lambda}$ over the wavelength range $\lambda = 0.4$ - 1 µm when the glass was weakly absorbing with those predicted numerically by the MCRT method using the specific locations and radii of the bubbles extracted from microCT scan. Similarly, Figures 4.9(c) and 4.9(d) present the corresponding results over the wavelength range $\lambda =$ 2 - 3 µm when the glass was absorbing. Note that the reported experimental measurements for the glass sample covered a wide range of glass absorption coefficients. The experimental measurements had a small relative error of around 2% and the error bands are shown in gray. The predictions by the hybrid model using the bubble size distribution reported in Figure 4.8(d) for volume fraction $f_v = 2\%$ are also presented. In addition, the results for the case without bubbles (i.e., $f_v = 0\%$) are provided as a reference. Here again, the predictions by the hybrid model combined with 1D Monte carlo simulations agreed very well with predictions by the MCRT model using periodic boundary conditions. The absolute differences of about 6-7% in the reflectance $R_{nh,\lambda}$ and of about 3-4% in the transmittance $T_{nh,\lambda}$ predicted by the hybrid model and experimental measurements were most likely due to radiation losses through the edges of the sample after scattering by bubbles. This is confirmed by the predic-

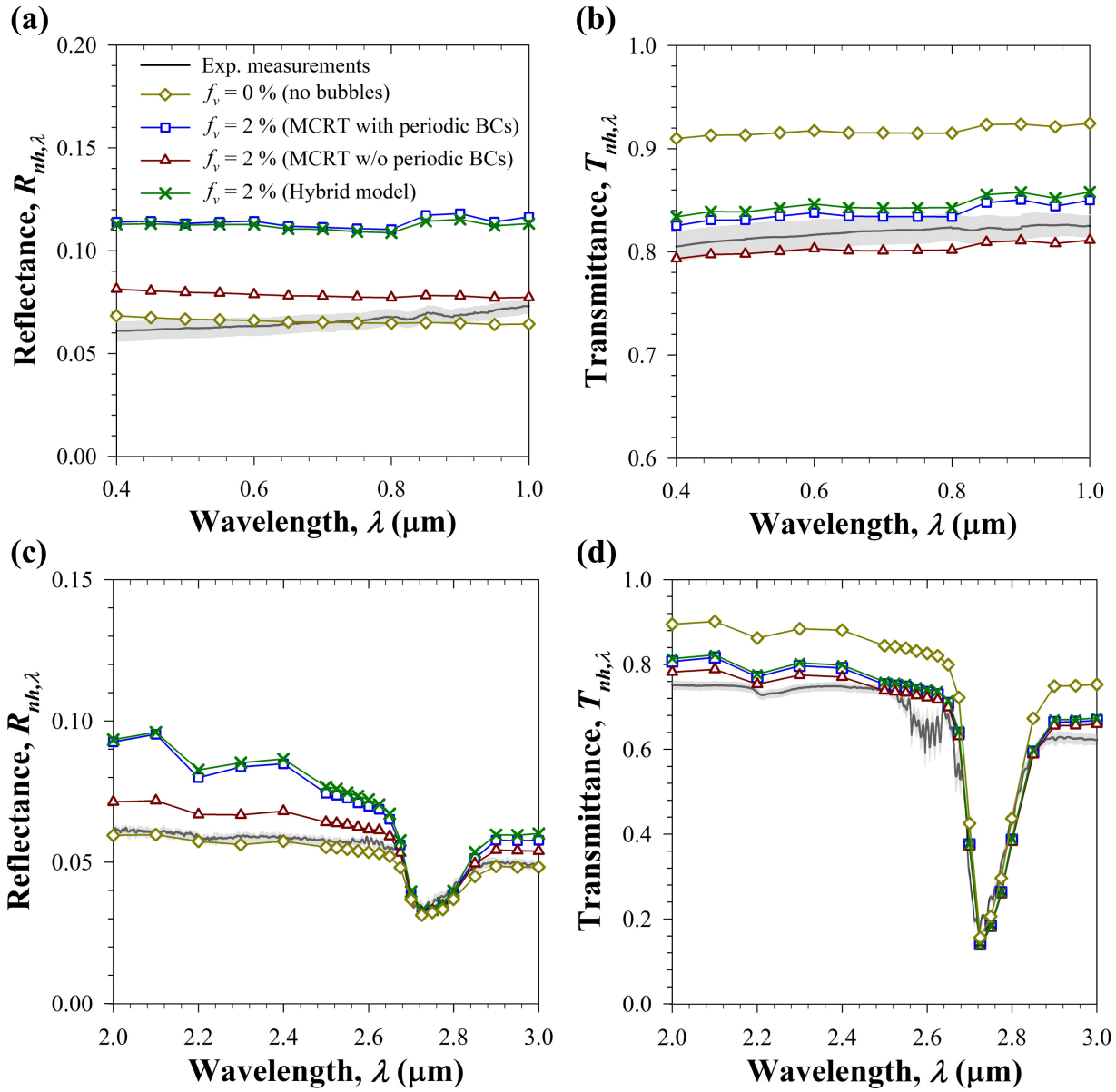

Figure 4.9: Comparison of the experimentally measured spectral normal-hemispherical reflectance $R_{nh,\lambda}$ and transmittance $T_{nh,\lambda}$ as functions of wavelength λ with the predictions by Monte Carlo ray-tracing method with and without periodic boundary conditions for wavelength range (a-b) λ = 0.4 - 1 μm and (c-d) λ = 2 - 3 μm. Predictions for the case without bubbles ($f_v = 0\%$) are also provided as a reference.

tions by the MCRT method without periodic boundary conditions (BCs) which agree better with the experimental measurements across the spectral range considered. In addition, the trends in the spectral variations of the predicted reflectance and transmittance differ slightly from their experimental measurements. This was most likely due to differences between the actual optical properties of the glass sample and those used in the simulations and obtained from the literature for fused silica [108, 109].

4.5.2 Reflectance of seafoam

Having identified the hybrid model as the most accurate, this chapter now focuses on simulating radiation transfer through seafoams by solving the 1D radiative transfer equation (RTE) using the hybrid model. To do so, an infinitely long and wide plane-parallel patch of seawater of complex index of refraction $m_{w,\lambda} = n_{w,\lambda} + ik_{w,\lambda}$ was assumed to be covered with a layer of seafoam of thickness H containing non-absorbing monodisperse air bubbles of diameter D, as illustrated in Figure 4.10. The seafoam was subjected to direct and diffuse solar radiation from the top. The bubbles in the seafoam backscattered some of the incident sunlight, given by the spectral normal-hemispherical reflectance $R_{nh,\lambda}$. The remaining fraction of incident radiation was assumed to be absorbed in the seawater, represented by the spectral absorptance $A_{n,\lambda}$.

The spectral refractive $n_{w,\lambda}$ and absorption $k_{w,\lambda}$ indices of water were obtained from Ref. [65]. The air bubbles were non-absorbing and had a refractive index $n = 1.0$ for all wavelengths. The volume fraction of bubbles inside seafoam was assumed to be constant at 74%. The spectral normal-hemispherical reflectance $R_{nh,\lambda}$ of the ocean surface covered with seafoam containing microbubbles was computed over wavelengths ranging between 0.3 and 3 µm spanning the solar spectrum. The simulations were performed for solar zenith angles θ varying between -90°and 90°.

The direct solar reflectance $R_{s,d}$ for a particular zenith angle θ was calculated by inte-

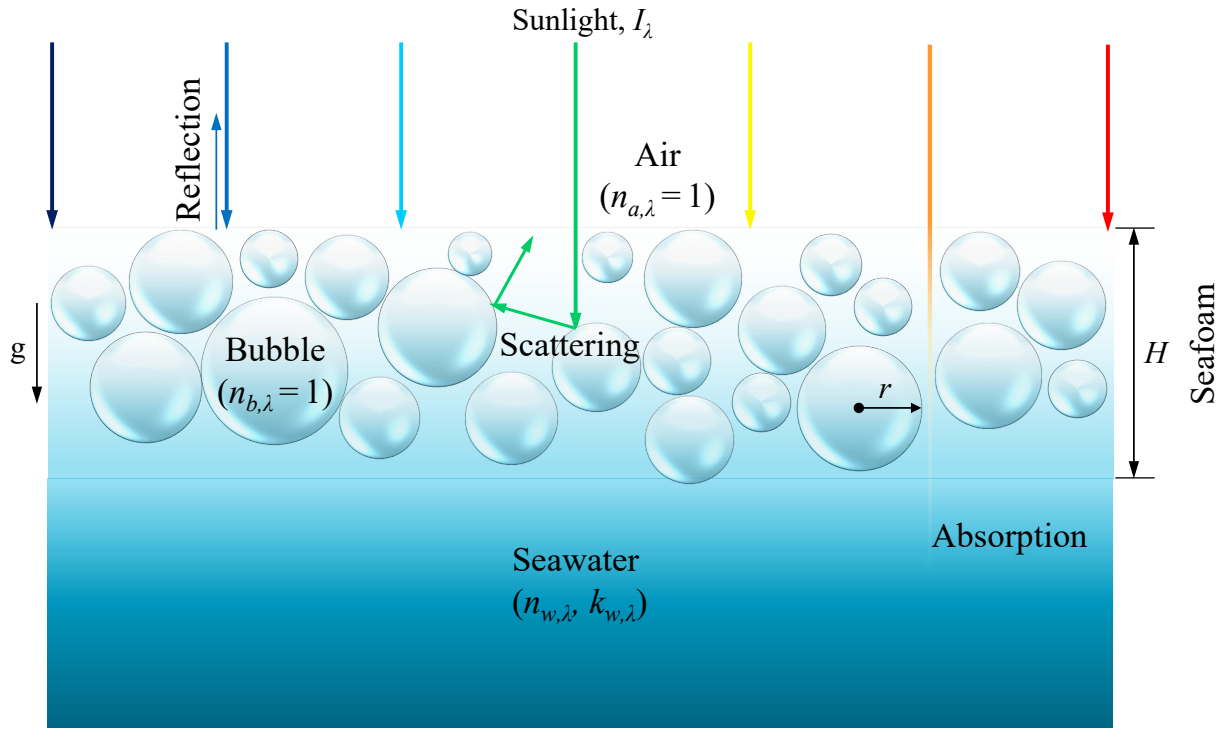

Figure 4.10: Schematic of seafoam layer composed of seawater ($n_{w,\lambda}$, $k_{w,\lambda}$) containing randomly distributed polydisperse spherical gas bubbles ($n_{b,\lambda} = 1$) on ocean surface and exposed to normally incident solar radiation.

grating the spectral reflectance over all wavelengths in the solar spectrum, as follows

$$R_{s,d}(\theta) = \frac{\int_{0.3\mu m}^{3.0\mu m} R_{dh,\lambda}(\theta) I_{s,\lambda} d\lambda}{\int_{0.3\mu m}^{3.0\mu m} I_{s,\lambda} d\lambda}, \tag{4.13}$$

where $I_{s,\lambda}$ is the spectral solar radiation intensity corresponding to AM 1.5G reference spectrum, according to standard ASTM G173-3. The diffuse solar reflectance $R_{s,diff}$ was computed by integrating the direct solar reflectance over all solar zenith angles given by

$$R_{s,diff} = \int_{-90^\circ}^{90^\circ} R_d(\theta) d\theta. \tag{4.14}$$

Then, the albedo of seafoam for a specific location was calculated using

$$\alpha = \frac{\int_{h_i}^{h_f} G_{DNI,h} cos\theta R_{s,d}(\theta) + G_{DHI,h} R_{s,diff} dh}{\int_{h_i}^{h_f} G_{DNI,h} cos\theta + G_{DHI,h} dh}, \tag{4.15}$$

where $G_{DNI,h}$ and $G_{DHI,h}$ are respectively the instantaneous direct normal and diffuse horizontal irradiance (in W/m^2) corresponding to sunshine hours h varying from h_i to h_f for that location.

4.5.2.1 Effect of bubble radius r and foam thickness H

Figure 4.11 plots the normal-hemispherical reflectance $R_{nh,\lambda}$ of seafoam (a) as a function of bubble radius r for different foam thicknesses and (b) as a function of foam thickness H for different bubble radii predicted by the hybrid model for monodisperse bubbles occupying volume fraction $f_v = 74\%$. The simulations were performed for wavelength $\lambda = 0.5$ µm as a representative of the visible portion of the solar radiation when water is weakly absorbing. Figure 4.11(a) shows that the reflectance $R_{nh,\lambda}$ increased exponentially as the bubble radius r decreased for a given foam thickness H. The reflectance was greater than 80% even for foam thicknesses as low as 5 mm. This is attributed to the large total scattering cross-section of the numerous bubbles present in seafoam when the bubble radius is small. On the other hand, for bubble radii $r \geq 1$ mm, the foam thickness needed to be significantly large to achieve a large reflectance. Figure 4.11(b) establishes that the reflectance $R_{nh,\lambda}$ increased initially with increasing foam thickness before plateauing for all considered bubble radii. The thickness after which the reflectance plateaus decreased with decreasing bubble radii due to increasing total scattering cross-section of bubbles. Indeed, for bubbles of radius $r = 0.1$ mm, the reflectance plateaued after just a thickness of 20 mm.

Figures 4.11(c) and 4.11(d) present the corresponding results for $\lambda = 1$ µm as a representative of the near-infrared portion of solar radiation when water is significantly absorbing. Figures 4.11(c) and 4.11(d) show trends similar to those in Figures 4.11(a) and 4.11(b) respectively, albeit with smaller magnitudes of reflectance $R_{nh,\lambda}$ due to absorption by water surrounding the bubbles in the seafoam layer. Figure 4.11(d) indicates that the reflectance plateaued after even smaller thicknesses when water was absorbing.

Overall, these results suggest that the bubble radius needs to be as small as possible and the foam thickness as large as possible to achieve the maximum reflectance. However,

practically, bubbles smaller than 10 µm in radius are very difficult to generate and sustain. Moreover, there is minimal gain in the achieved reflectance past a thickness $H = 20$ mm when the bubble radius $r \leq 100$ µm.

4.5.2.2 Effect of solar zenith angle θ

Figure 4.12 plots the direct reflectance R_d of seafoam calculated over the solar spectrum using Equation (4.13) as a function of solar zenith angle θ of solar radiation for bubble radii $r = 10$, 50, and 100 µm for foam thickness $H = 10$ mm and volume fraction $f_v = 0.74$. Figure 4.12 shows that the reflectance R_d was symmetric with respect to the solar zenith angle θ, as expected. It establishes that the reflectance R_d for small bubbles was consistently larger than that for larger bubbles for all solar zenith angles θ. This can be attributed to the large total scattering cross-section of the small bubbles as compared to larger bubbles for a given volume fraction f_v and foam thickness H. Moreover, the reflectance was nearly constant for θ ranging between the -60° and 60° for all bubble radii. However, as the solar zenith angle increased further, the reflectance R_d increased for all bubble radii and approached unity as θ was close to 90° or -90°.

4.5.2.3 Albedo calculation

Figure 4.13 presents a contour plot showing the albedo of ocean surface covered with seafoam computed using Equation (4.15) for bubble radius r ranging between 10 and 1000 µm and seafoam thickness H varying from 0 to 20 mm. The albedo was calculated using the instantaneous direct normal G_{DNI} and diffuse horizontal G_{DHI} irradiance values corresponding to June 21, 2023 in Hong Kong obtained from the National Oceanic and Atmospheric Administration's (NOAA) solar calculator [111]. The location was chosen given the significant shipping traffic density in Hong Kong. Figure 4.13 shows that for bubble radii $r \leq 100$ µm, the albedo was larger than 0.8 for foam thickness H as low as 5 mm. In fact, for bubble radius $r = 10$ µm, the ocean albedo increased dramatically from about 0.06 to around 0.8 for foam thickness less than 1 mm. This establishes the efficacy of introducing seafoams filled

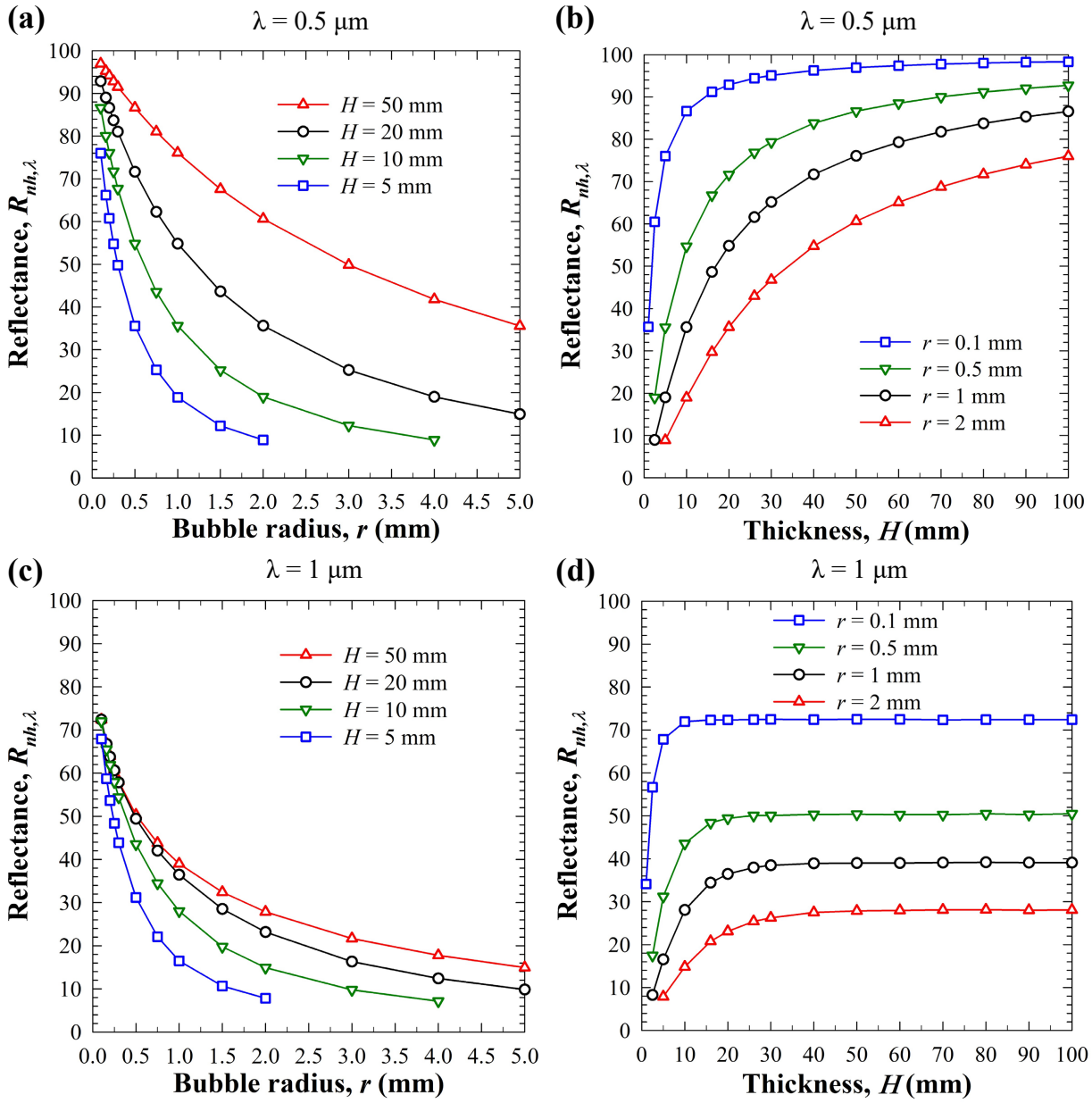

Figure 4.11: Normal-hemispherical reflectance $R_{nh,\lambda}$ of seafoams containing bubbles (a,c) as a function of bubble radius r for different foam thicknesses, and (b,d) as a function of foam thickness H for different bubble radii for seafoams exposed to monochromatic radiation of wavelength (a,b) $\lambda = 0.5$ μm and (c,d) $\lambda = 1$ μm. The bubble volume fraction was $f_v = 74\%$ in all the cases. The simulations were performed using hybrid model identified earlier in the chapter.

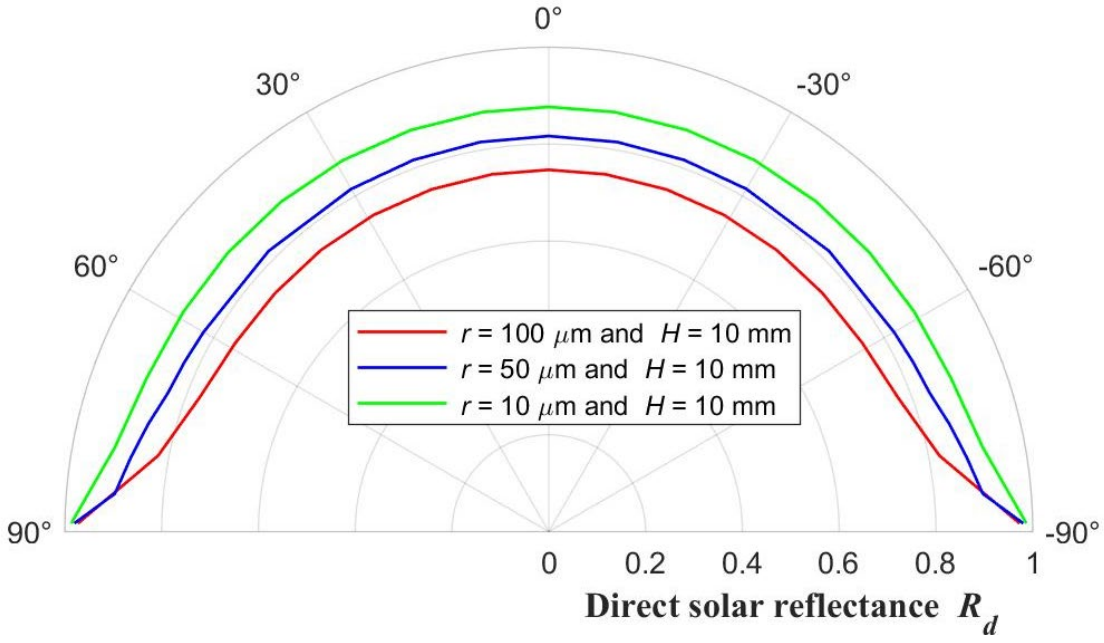

Figure 4.12: Direct solar reflectance $R_{s,d}$ of seafoams computed as a function of solar zenith angle θ using Equation (4.13) for different bubble radii for bubble volume fraction $f_v = 74\%$.

with microbubbles over ocean surfaces to reflect sunlight.

4.5.2.4 Radiative forcing calculation

The global impact of any geoengineering technique is quantified using radiative forcing, which is the change in Earth's energy balance due to a forcing agent in Earth's natural systems. Geoengineering techniques are specifically designed to partially counter the global radiative forcing from greenhouse gases, which is approximately 3.5 W/m^2 since the pre-industrial era (1750) [112]. Popular geoengineering techniques such as stratospheric aerosol injection or marine cloud brightening have the potential to achieve a radiative forcing of about 4 W/m^2, enough to counter the global radiative forcing from greenhouse gases lenton2009radiative. However, both these techniques require significant infrastructure that is not yet existent. On the other hand, existing cargo ships can be easily modified to generate high albedo seafoams in shipping lanes worldwide.

A typical cargo ship of width 25 to 50 m moving at a speed of about 30 km/h leaves

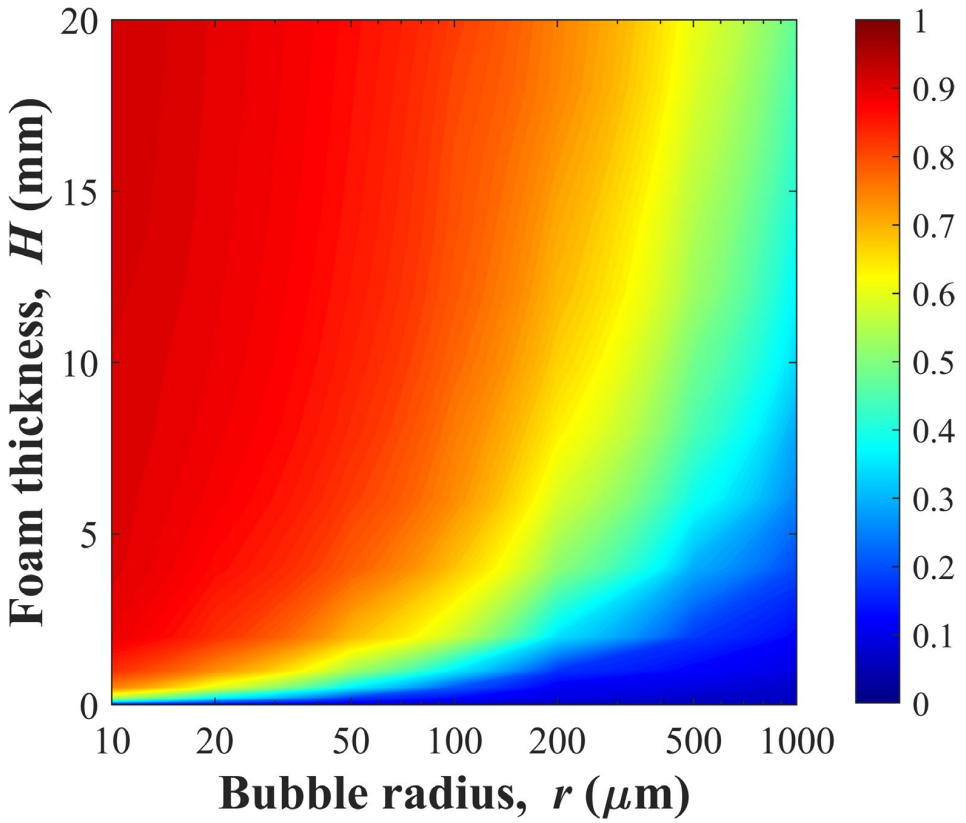

Figure 4.13: Contour plot of seafoam albedo calculated using Equation (4.15) for a wide range of bubble radii r and foam thicknesses H using the instantaneous direct normal G_{DNI} and diffuse horizontal G_{DHI} irradiance values corresponding to June 21, 2023 in Hong Kong [111].

behind a wake that is 50 to 100 m wide and extends for about 10 kilometers [24]. Here, we assume the width of ship wake to be 75 m. Assuming that the lifetime of bubbles in the wake can be increased to about 10 hours using ocean-based natural surfactants and assuming that the wake thickness remains constant throughout its lifetime, the wake area from a single ship can be calculated as $A_{wake} = 30 \times 10 \times 0.075 = 22.5$ km^2. Then, increasing the ship wake albedo from $\alpha_{w,i} = 0.06$ to $\alpha_{w,f} = 0.9$ using microbubbles as described in Section 4.5.2.3 could result in radiative forcing $f = (A_{wake} \times G_{solar} \times (\alpha_{w,f} - \alpha_{w,i}))/A_{earth} = 3.67 \times 10^{-5}$ W/m^2 for a single ship, where G_{solar} is the solar irradiance and assumed to be 1000 W/m^2 and $A_{earth} = 5.1 \times 10^8$ km^2 is the total surface area of Earth. Given that there are 55,000 ships at sea each day [23], the total achievable radiative forcing could be about $f_{total} = 2$

W/m^2. Such a large radiative forcing could lead to substantial mitigation of climate change resulting from greenhouse gases.

The above calculations were performed to estimate the achievable radiative forcing by ocean albedo enhancement in ship wakes. However, the actual radiative forcing could significantly differ from the calculated value since the solar irradiance and the shipping traffic density vary substantially with geographic location. Moreover, the Earth's climate could respond to the climate intervention strategy in unexpected ways, resulting in a significantly higher or substantially lower radiative forcing than predicted. Therefore, detailed simulations using a fully-coupled, global climate model are necessary to accurately predict the impact of ocean albedo enhancement in ship wakes on the global climate.

4.6 Conclusion

This study combined experimental, numerical, and theoretical methods to assess the validity of three previously proposed models predicting radiation transfer through semitransparent slabs containing large non-absorbing gas bubbles. These different models were critically reviewed and their limitations were unequivocally established. A hybrid model was also proposed predicting the scattering coefficient and the asymmetry factor by Lorenz-Mie theory while the absorption coefficient was expressed as the sum of absorption coefficients of the bubbles and the medium weighted by their respective volume fractions. Unlike previous models, the new hybrid model showed excellent agreement with rigorous Monte Carlo ray-tracing results based on geometric optics in predicting the reflectance and transmittance for a wide range of bubble volume fractions, slab thicknesses, and absorption coefficients. In addition, a digital twin of a thick glass sample containing large number of gas bubbles was constructed using a microCT scan of the sample to extract bubble locations, size distribution, and volume fraction for input into the models. The predictions by the hybrid model were also in good agreement with the experimental measurements of the normal-hemispherical transmittance and reflectance in the spectral window between 0.4 and 3 µm when silica ranges from weakly absorbing to absorbing. These results highlight the adequacy and robustness of

the hybrid model in rapidly simulating radiation transfer through a semitransparent medium containing spherical bubbles with a wide range of bubble volume fraction and size distribution as well as different thicknesses and medium compositions. Finally, the hybrid model was used to perform spectral simulations of solar radiation transfer through ocean surfaces covered with seafoams containing microbubbles to quantify the ocean albedo enhancement. It was found that just introducing 10 mm thick seafoams containing bubbles of radius around 10 µm and volume fraction 74% increased the ocean albedo from about 0.06 to around 0.9. Such a large albedo could be realistically achieved in ship wakes by using microbubble generators in ships along with natural ocean-based surfactants. Therefore, this climate intervention strategy could be a simple and cost-effective approach to partially counter global radiative forcing from greenhouse gases.

CHAPTER 5

Optically-clear mesoporous silica aerogels for passive radiative cooling

This chapter demonstrates the use of mesoporous silica aerogels as optically transparent radiative cooling materials exhibiting emissivity near unity in the long wave infrared radiation (LWIR) atmospheric transparency window between 8-13 µm. Silica is a popular radiative cooling material due to its favorable optical properties in the visible and infrared parts of the electromagnetic spectrum. However, it exhibits a reflectance peak and low emittance around 9 - 9.5 µm resulting from Reststrahlen effect. Consequently, the maximum achievable radiative cooling power decreases significantly for silica-based radiative cooling surfaces at 300 K corresponding to a peak blackbody spectral emissive power at $\lambda = 9.7$ µm. Previous studies have attempted to maximize the emissivity of silica-based radiative coolers using complex photonic structures. In this study, we utilize the mesoporous microstructure of ambiently dried and hydrophobic silica aerogels to eliminate the reflectance peak of silica around 9 - 9.5 µm. The aerogels were composed of silica nanoparticles (radius $\sim$ 2 nm) with a narrow pore size distribution below 20 nm. Both the particles and the pores were much smaller than the visible wavelengths resulting in minimal scattering and high transmittance ($>$ 95%). The emissivity and solar absorptance of these silica aerogels with/without aluminum substrates were experimentally determined over the spectral range from 0.3 - 20 µm. The results establish that aerogels can be used on top of metallic surfaces for daytime radiative cooling applications. Additionally, they can be used as covers for applications that require solar transmission such as thermophotovoltaic (TPV) cells and glazings.

5.1 Background

Several studies [36, 113, 114] have attempted to increase the emittance of silica for radiative cooling applications. Blandre et al. [36] used surface texturing in the form of 1D lamellar and 2D cubic gratings on silica coatings on top of Ag substrates. The gratings' dimensions were designed to scatter evanescent waves and couple them with propagating modes thereby increasing the emittance value from about 0.3 to 0.85 around $\lambda = 9$ µm. The net daytime radiative cooling power $q^{"}_{cool}$ achievable with the 1D lamellar and 2D cubic grating design were calculated to be 98 W/m^2 and 114 W/m^2 respectively. These results should be compared with $q^{"}_{cool} = 89$ W/m^2 achieved using a planar silica coating. However, the proposed design also increased absorption of the solar radiation which is undesirable.

Chillón et al. [113] demonstrated a scalable fabrication technique to etch nanopillars of diameter $\sim$ 300 nm and depth $\sim$ 1.25 µm on fused silica glass slab that increased its emittance from about 0.3 to 0.8 around $\lambda = 9$ µm by coupling light with surface phonon-polariton (SPhP) modes [115, 116]. However, this approach significantly decreased the slab's transmittance in the UV and visible wavelengths due to scattering by the nanopillars. The authors showed that coating the nanopillars with a 1.5 µm thick layer of PMMA minimized the visible haze by reducing the refractive index mismatch. However, the PMMA coating led to significant absorption of UV radiation that could result in heating.

Akerboom et al. [114] patterned a silica slab with silica microcylinders to enhance the radiative cooling power of a silicon solar module. The authors used photonic structures and finite-difference time-domain (FDTD) simulations to optimize the microcylinder array design to maximize the emittance of the glass cover. The fabricated microstructured glass cover was placed on top of a silicon substrate coated with gold at its back to mimic an opaque silicon solar module. This new module exhibited an average emittance of 0.97 between $\lambda =$ 7.5-16 µm, which was significantly higher than the average emittance of 0.84 achieved with planar silica glass cover. However, the emittance around $\lambda = 9$ µm was only around 0.7.

This study presents multifunctional optically transparent silica-based aerogels with controlled mesoporous structure to maximize the spectral emittance in the atmospheric trans-

parency window near room temperature and minimize solar absorptance. These ambiently-dried aerogel monoliths can be used on top of metallic surfaces for passive daytime radiative cooling applications. Additionally, the aerogels could be used as covers for thermophotovoltaic (TPV) cells, glazings, as well as windows of vehicles to achieve both radiative cooling and visible light transmission.

5.2 Materials and methods

5.2.1 Sample preparation

Aerogels of porosity $\phi = 72.5\%$, 80.9%, and 87.5% and thickness $H = 1.15$ mm were synthesized by an ambient drying procedure in which complex mesoporous organo-silica monoliths were prepared using an acid-base-catalyzed sol-gel synthesis [117]. First, a solution was prepared containing tetraethoxysilane (TEOS) (Sigma-Aldrich), methyl triethoxysilane (MTES) (Sigma-Aldrich), ethanol (EtOH), deionized water, and formamide (Sigma-Aldrich) in molar ratios of 1.5:1:6.25:6.25:5, respectively. Then, a base catalyst of 2M NH_4OH was added at a volume ratio of 6 mL base to 17 mL sol before transferring to a 10 cm $\times$ 10 cm $\times$ 1.5 mm plastic cassette. After ageing for two days, gel monoliths were removed from the cassettes, and submerged in ethanol. The ethanol was then exchanged with n-heptane, which was the final drying solvent. The samples were then dried at ambient temperature and pressure by draining the solvent and allowing slow evaporation of the pore solvent in a sealed container over $\sim$1 week.

Finally, the prepared aerogel monoliths of porosity $\phi = 72.5\%$, 80.9%, and 87.5% were adhered to the top of separate aluminum wafers of radius $r_d = 12.5$ mm using an optically clear adhesive film (3M) to prepare radiative cooling Samples 1, 2, and 3, respectively. Sample 4 corresponds to the aerogel of porosity $\phi = 87.5\%$ without any substrate. The details of all samples are summarized in Table 1.

Table 5.1: Details of radiative cooling samples

Samples	Emitter	Emitter thickness H (mm)	Emitter porosity ϕ (%)	Reflector (Substrate)
Sample 1	Silica aerogel	1.15	87.5%	None
Sample 2	Silica aerogel	1.15	72.5%	Aluminum
Sample 3	Silica aerogel	1.15	80.9%	Aluminum
Sample 4	Silica aerogel	1.15	87.5%	Aluminum

5.2.2 Simulations

The effective spectral refractive $n_{eff,\lambda}$ and absorption $k_{eff,\lambda}$ indices of mesoporous silica aerogel of thickness H and porosity ϕ were determined using the Maxwell-Garnett effective medium theory [50]. Using these optical properties, the spectral normal-hemispherical transmittance $T_{nh,\lambda}$ and reflectance $R_{nh,\lambda}$ of silica aerogels with or without an aluminum substrate were predicted using the transfer matrix method (TMM) [51]. Finally, using Kirchhoff's law of thermal radiation and energy balance, the spectral normal emittance of the opaque radiative cooling surfaces was given by $\varepsilon_{n,\lambda} = A_{n,\lambda} = 1 - R_{nh,\lambda} - T_{nh,\lambda}$.

5.2.3 Transmittance and reflectance measurements

A double-beam ultraviolet-visible (UV-Vis) spectrophotometer (Evolution^{TM} 220, Thermo Scientific Fisher, USA) equipped with an integrating sphere (Evolution^{TM} ISA-200 Integrating Sphere Accessory, Thermo Scientific Fisher, USA) was used for measuring the normal-hemispherical transmittance $T_{nh,\lambda}$ and reflectance $R_{nh,\lambda}$ of the samples over the wavelength range $\lambda = 0.3$ to 1.1 µm. Measurements for wavelengths $\lambda = 1.1$ µm to 20 µm were performed using a nitrogen-purged Fourier transform infrared (FTIR) spectrometer (Nicolet^{TM} iS50,

Thermo Scientific Fischer, USA) equipped with an integrating sphere (Upward IntegratIR^{TM}, PIKE Technologies, USA). An InGaAs detector with a CaF_2 beam-splitter was used for the IR measurements over wavelengths 1.1 to 2 µm while an MCT detector with a KBr beam-splitter was used for wavelengths ranging from 2 to 20 µm.

5.2.4 Emittance and solar absorptance

Based on Kirchoff's law of thermal radiation [118], the spectral directional emittance of a material $\varepsilon_{\theta,\lambda}$ is equal to its spectral directional absorptance $A_{\theta,\lambda}$ under thermal equilibrium. Therefore, the spectral normal emittance $\varepsilon_{n,\lambda}$ of the aerogel can be experimentally determined by measuring its spectral normal-hemispherical transmittance $T_{nh,\lambda}$ and reflectance $R_{nh,\lambda}$ according to the energy balance expressed as [119]

$$\varepsilon_{n,\lambda} = A_{n,\lambda} = 1 - R_{nh,\lambda} - T_{nh,\lambda}. \tag{5.1}$$

Furthermore, the normal emittance of the aerogels in the LWIR atmospheric transparency window $\varepsilon_{n,LWIR}$ can be defined as [120]

$$\varepsilon_{n,LWIR} = \frac{\int_{8\mu m}^{13\mu m} \varepsilon_{n,\lambda} E_{b,\lambda}(T) d\lambda}{\int_{8\mu m}^{13\mu m} E_{b,\lambda}(T) d\lambda} \tag{5.2}$$

where $E_{b,\lambda}(T)$ is the spectral blackbody emissive power (in W/m^{2}µm) at temperature T. Similarly, the normal solar absorptance α_s of the sample exposed to collimated and normally incident spectral solar radiation intensity $I_{s,\lambda}$ (AM 1.5G reference spectrum, according to standard ASTM G173-3) is defined as [119]

$$\alpha_s = \frac{\int_{0.3\mu m}^{3.0\mu m} A_{n,\lambda} I_{s,\lambda} d\lambda}{\int_{0.3\mu m}^{3.0\mu m} I_{s,\lambda} d\lambda}. \tag{5.3}$$

5.2.5 Radiative cooling power

The radiative cooling surface of unit surface area absorbs solar radiation at a rate of q''_{solar} given by

$$q''_{solar} = \int_0^\infty I_{s,\lambda} A_{n,\lambda} d\lambda. \tag{5.4}$$

The surface also absorbs atmospheric radiation at a rate of q''_{atm} given by

$$q''_{atm} = \int_{2\pi}\int_{0}^{\infty} E_{b,\lambda}(T_o)\alpha_{\theta,\lambda}\varepsilon_{atm,\theta,\lambda}cos\theta d\lambda d\Omega, \tag{5.5}$$

where T_o is the ambient temperature, θ is the angle of incidence/emission, and $\varepsilon_{atm,\lambda,\theta} = 1 - T_\lambda^{1/cos\theta}$ is the spectral directional emittance of the Earth's atmosphere having spectral transmittance T_λ [121]. The radiative cooling surface loses heat by emitting thermal radiation at a rate of q''_{rad} given by

$$q''_{rad} = \int_{2\pi}\int_{0}^{\infty} E_{b,\lambda}(T_e)\varepsilon_{\theta,\lambda}cos\theta d\lambda d\Omega, \tag{5.6}$$

where T_e is the temperature of the top surface of emitter. Therefore, the net radiative cooling power q''_{cool} can be written as [28]

$$q''_{cool} = q''_{rad} - q''_{solar} - q''_{atm} \tag{5.7}$$

Here, the contribution from convective heat transfer was ignored by assuming the emitter surface temperature to be the same as ambient temperature such that $T_e = T_o = 300$ K. Note that the net radiative cooling power q''_{cool} can vary substantially with the thickness H of the emitter. This is because the rate of absorption of solar q''_{solar} and atmospheric radiation q''_{atm} as well as the rate of emission from the radiative cooling surface q''_{rad} increase with increasing emitter thickness H before plateauing [122].

5.3 Results and discussion

5.3.1 Aerogel as a transparent cover

5.3.1.1 Spectral transmittance and normal emittance

Figure 5.1(a) plots the spectral normal-hemispherical transmittance $T_{nh,\lambda}$ measured over the solar spectrum for radiative cooling Sample 1 consisting of mesoporous silica aerogel of porosity $\phi = 87.5\%$ and thickness $H = 1.15$ mm without any substrate. The spectral transmittance of non-porous silica slab of the same thickness predicted using transfer matrix method and the spectral solar irradiance (AM 1.5G spectrum) are also provided as references.

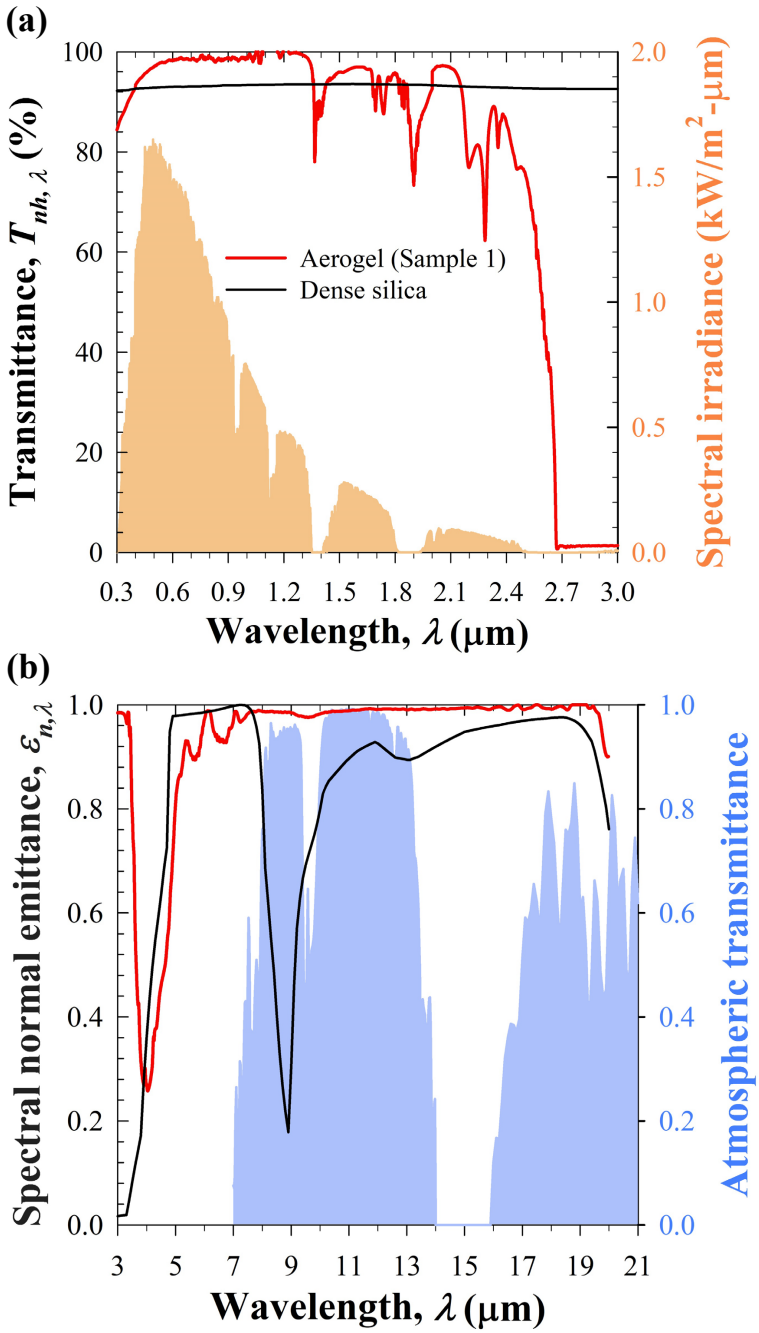

Figure 5.1: (a) Comparison of spectral normal-hemispherical transmittance $T_{nh,\lambda}$ of a stand-alone silica aerogel slab (Sample 1) of porosity $\phi = 87.5\%$ and thickness $H = 1.15$ mm measured over the solar spectrum with that of a non-porous silica slab of identical thickness predicted using transfer matrix method. (b) Comparison of their corresponding spectral normal emittance $\varepsilon_{n,\lambda}$ in the spectral window 3 to 20 μm. The spectral solar irradiance (AM 1.5G reference spectrum) and the spectral transmittance of atmosphere are provided as references in (a) and (b), respectively.

Figure 5.1(a) shows that the aerogel was highly transparent over the solar spectrum, with a solar transmittance $T_{s,a} = 0.9$, comparable to that of a non-porous silica slab of identical thickness ($T_{s,g} = 0.92$). Here again, some absorption peaks were observed due to the presence of surface hydroxyl groups and water adsorbed on the surface of aerogels.

Figure 5.1(b) plots the spectral normal emittance $\varepsilon_{n,\lambda}$ of Sample 1 determined experimentally over the wavelength window 3 to 20 µm in which the transmittance vanishes. The spectral normal emittance of dense silica slab and the spectral transmittance of the atmosphere are also provided as references. Figure 5.1(b) establishes that the aerogel exhibited an emittance approaching unity in the atmospheric transparency window of 8-13 µm without any substrate. The highly porous aerogel microstructure nearly eliminated the characteristic reflectance peak of silica around 9 µm.

Overall, Figure 5.1 demonstrates that silica aerogels can be used as optically transparent radiative cooling covers where visible light transmission is essential such as for photovoltaic solar cells. However, such aerogels covers could act as thermal insulator if they are too thick due to their significantly low thermal conductivity < 50 mW/mK [117]. Therefore, their thickness should be optimized to minimize the thermal insulation from aerogels and retain their high emittance and radiative cooling power.

5.3.2 Aerogel on top of aluminum substrate

5.3.2.1 Effect of porosity on emittance and radiative cooling power

Figure 5.2(a) compares the experimentally determined spectral normal emittance $\varepsilon_{n,\lambda}$ of Samples 2-4 described in Table 5.1 with their corresponding predictions by the transfer matrix method for wavelengths ranging from 5 to 20 µm. Predictions of the emittance for a 1.15 mm thick non-porous silica slab on top of aluminum substrate are also provided as reference. Figure 5.2(a) establishes that the experimental measurements were in relatively good agreement with the spectral predictions for all aerogel porosities. This can be attributed to the fact that the radii of the silica nanoparticles ($r_s \sim 2$ nm) and pores ($r_p \sim 25$ nm) constituting the aerogel samples were much smaller compared to the wavelengths considered

so that aerogel could be treated as homogeneous with effective refractive $n_{eff,\lambda}$ and absorption $k_{eff,\lambda}$ indices given by Maxwell-Garnett effective medium approximation. Figure 5.2(a) also shows that as the porosity increased from $\phi = 0\%$ to 72.5%, the emittance around $\lambda = 9$ µm significantly increased from about 0.18 to around 0.8. This can be attributed to the fact that the refractive index mismatch between the effective medium and surrounding air decreased as porosity increased. In fact, for Sample 4 with very large porosity $\phi = 87.5\%$, the characteristic reflectance peak of silica was effectively eliminated and the emittance approached unity.

Figure 5.2(b) presents the radiative cooling power q''_{cool} corresponding to Samples 2-4 and to dense silica on top of aluminum substrate as a function of emitter thickness H calculated using Equation (5.7) assuming emitter surface temperature to be the same as ambient temperature, i.e., $T_e = T_o = 300$ K. Predictions of the radiative cooling powers q''_{cool} of each sample when the aluminum substrate is replaced with a silver substrate are also provided as references. Figure 5.2(b) establishes that having a porous microstructure for the silica coating significantly enhanced its radiative cooling power compared to non-porous coating. Here, the increase in emittance $\varepsilon_{n,\lambda}$ around $\lambda = 9$ µm contributed significantly to the total radiative cooling power for bodies at temperature $T = 300$ K that exhibit peak blackbody spectral emissive power around the same wavelength. Figure 5.2(b) also shows that the radiative cooling power of the surfaces with aerogel slabs was nearly constant for thickness $H \geq 100$ µm since the aerogels were opaque to LWIR radiation beyond this thickness. Additionally, the minimum thickness H beyond which the radiative cooling power plateaued decreased with decreasing porosity. This was expected since aerogels with lower porosity absorb more infrared radiation than more porous aerogels with the same thickness. Therefore, both porosity and thickness can be adjusted to maximize radiative cooling power knowing that it is harder to dry thicker monoliths without cracking. Additionally, Figure 5.2(b) shows that using a silver substrate can lead to substantially larger radiative cooling power compared to aluminum substrate. However, the high cost of silver substrates may not justify the potential benefits in terms of radiative cooling power.

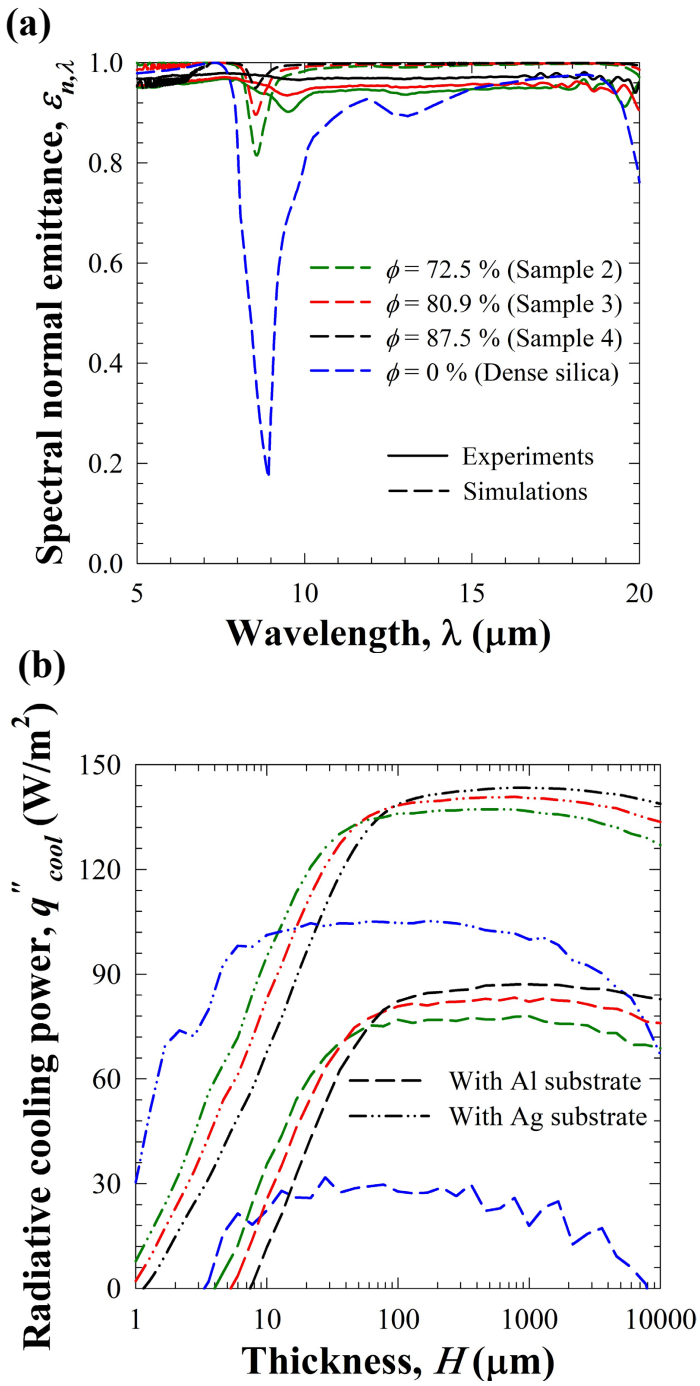

Figure 5.2: (a) Comparison of experimentally measured and simulated spectral normal emittances $\varepsilon_{n,\lambda}$ of radiative cooling Samples 2-4 (see Table 5.1) consisting of mesoporous silica aerogels of thickness $H = 1.15$ mm and porosity ϕ placed on top of aluminum substrate. (b) Corresponding radiative cooling power q''_{cool} of the radiative cooling surfaces calculated as a function of emitter thickness H with aluminum/silver substrates. The predictions for a non-porous silica slab on top of aluminum/silver substrate are provided as references.

5.3.2.2 Solar spectral reflectance and normal emittance

Figure 5.3(a) plots the spectral normal-hemispherical reflectance $R_{nh,\lambda}$ of radiative cooling Sample 4 with porosity $\phi = 87.5\%$ measured over the solar spectrum. The spectral reflectance of a bare aluminum substrate and the spectral solar irradiance (AM 1.5G spectrum) are also provided as references. Figure 5.3(a) shows that the radiative cooling surface exhibited a large solar spectral reflectance $R_{nh,\lambda}$, similar to that of bare aluminum. In fact, the normal solar absorptance α_s [Equation (5.3)] of the radiative cooling surface was calculated to be 0.10 similar to that of bare aluminum estimated as 0.09. This difference can be attributed to absorption of UV radiation and multiple scattering by silica nanoparticles in the aerogel [108]. The aerogel also exhibited some absorption peaks in the UV and near-IR wavelengths due to the presence of surface hydroxyl groups as well as water adsorbed on the surface of aerogels [117]. However, these peaks contributed minimally to the average solar absorptance of the aerogels because the spectral solar irradiance was small at those wavelengths.

Figure 5.3(b) plots the spectral normal emittance $\varepsilon_{n,\lambda}$ of the radiative cooling Sample 4 determined experimentally over the wavelengths ranging between 3 and 20 µm. The spectral transmittance of the Earth's atmosphere is provided as a reference. Figure 5.3(b) establishes that the Sample 4 exhibited a near-unity emittance ($\varepsilon_{n,LWIR} = 0.99$) in the atmospheric transparency window of 8-13 µm, significantly higher than those previously reported in literature for silica-based radiative cooling surfaces [36, 113, 114]. The highly porous microstructure of the aerogel nearly eliminated the characteristic reflectance peak of non-porous silica slab around 9 µm. These results establish the efficacy of the proposed aerogel-based radiative cooling surface in minimizing solar heat gain.

5.3.2.3 Average directional LWIR emittance

Figure 5.4 plots the directional emittance $\varepsilon_{d,LWIR}$ of radiative cooling Sample 4 ($\phi = 87.5\%$) and dense silica ($\phi = 0\%$) on aluminum substrate simulated using the transfer matrix method and averaged over the LWIR atmospheric transparency window between 8-13 µm. The method was validated by comparing predictions of $\varepsilon_{n,\lambda}$ with experimental measurements.

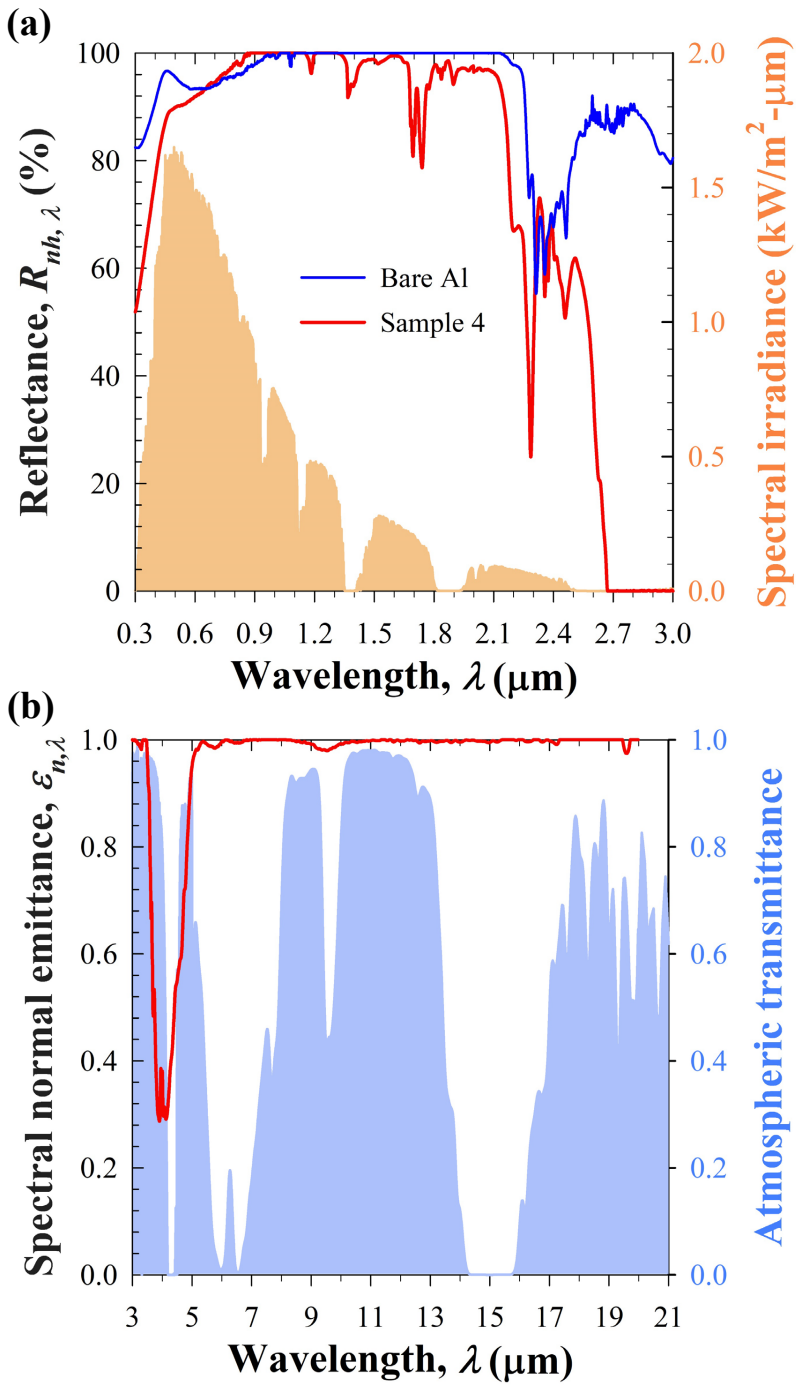

Figure 5.3: (a) Spectral normal-hemispherical reflectance $R_{nh,\lambda}$ of Sample 4 ($\phi = 87.5\%$) and bare aluminum measured over the solar spectrum. (b) Corresponding spectral normal emittance $\varepsilon_{n,\lambda}$ of the radiative cooling surface computed from the measurements in the wavelength window 3 to 20 μm. The spectral solar irradiance (AM 1.5G reference spectrum) and the spectral transmittance of atmosphere are provided as references in (a) and (b), respectively.

Figure 5.4 shows that the average emittance of dense silica was only about 0.83 for emission angles less than about 30°, and decreased significantly for larger angles due to substantial surface reflection. By contrast, the average emittance of Sample 3 exceeded 0.97 for angles up to 60°, and decreased thereafter for larger angles due to the aerogel porosity and the smaller refractive index mismatch with the surrounding air. Such large and broad directional emittance is beneficial in maximizing its radiative cooling power [123].

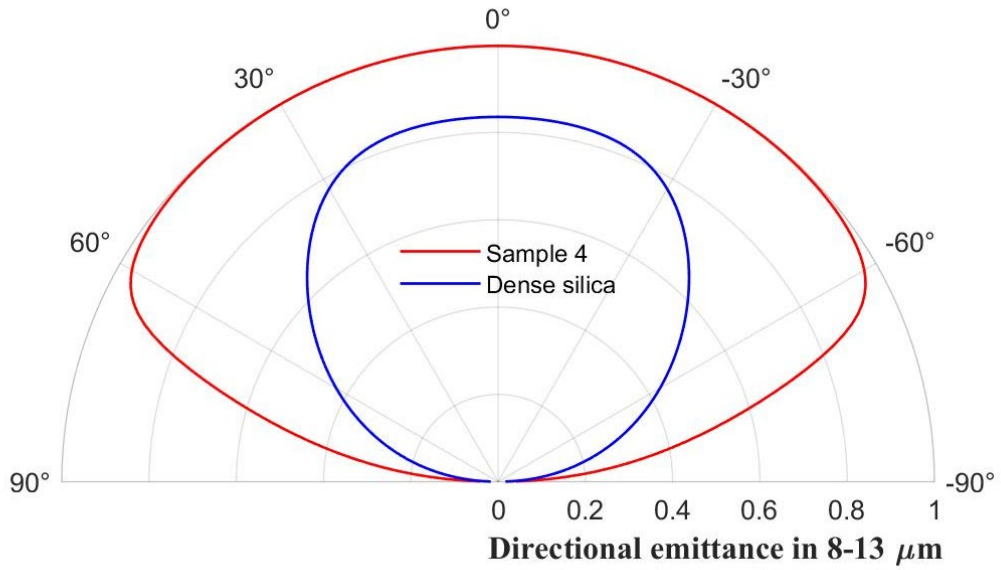

Figure 5.4: Predictions of the LWIR-averaged directional emittance $\varepsilon_{d,LWIR}$ of radiative cooling Sample 4 [see Table 5.1] and dense silica on aluminum substrate in the LWIR atmospheric transparency window ranging between 8-13 μm.

5.4 Conclusion

This study experimentally demonstrated a novel approach to maximize the emittance of silica-based radiative cooling surfaces that can be used on top of reflective substrates made of metals such as aluminum or silver for daytime radiative cooling applications. The aerogel

monoliths exhibited emissivities approaching unity in the atmospheric transparency window. Their radiative cooling power was significantly larger than those of dense silica covers of identical thickness at near room temperature. Additionally, the samples could be used alone as transparent covers in applications requiring solar transmission such as solar cell covers, glazings, and window solutions.

CHAPTER 6

Conclusions and Future work

6.1 Conclusions

The objectives of this dissertation were (i) to systematically quantify the optical losses caused by gas bubbles during photoelectrochemical water splitting, (ii) to critically review and validate different radiative transfer models for semitransparent media containing scatterers and use the most accurate model to predict albedo of ship wakes containing microbubbles, and (iii) to demonstrate the use of mesoporous silica aerogels as optically transparent radiative cooling materials.

The first objective was achieved in Chapters 2 and 3. In Chapter 2, Monte Carlo ray-tracing model was developed to simulate the scattering of solar radiation by cap-shaped gas bubbles attached to horizontal Si photoelectrode surface. Such a scenario corresponds to the onset of water splitting reaction and/or to PEC cells having horizontal photoelelectrodes covered by a very thin layer of electrolyte. Overall, optical losses up to 18% were predicted for Si photoelectrodes covered with bubbles having a contact angle of $\theta_c = 120°$and a projected area coverage of 78.5%. Additionally, scattering by bubbles led to significant local variations in the absorbed photon flux, with substantial light concentration - by a factor of up to two - outside the bubbles' projected footprint as compared to a bare photoelectrode. In Chapter 3, the Monte Carlo ray-tracing model was expanded to account for scattering by detached spherical gas bubbles and absorption by the aqueous electrolyte. It was found that the bubble diameter most significantly impacted optical losses, followed by plume thickness, bubble volume fraction, and surface area coverage. Overall, to minimize optical losses, it was recommended to use hydrophilic photoelectrodes to minimize the bubble contact surface

area coverage, increase bubble departure diameter by increasing the surface tension of the electrolyte/bubble interface, employ convection to flow electrolyte and decrease bubble plume thickness, and illuminate the PEC cell from the anode side since oxygen bubbles are larger yet fewer than hydrogen bubbles.

The second objective was achieved in Chapter 4. Different radiative transfer models were critically reviewed and their limitations were unequivocally established. The normal-hemispherical reflectance and transmittance predictions of these models were compared against the predictions by the Monte Carlo ray-tracing (MCRT) method for a wide range of bubble volume fractions, slab thicknesses, and medium absorption coefficients. For experimental validation, first, a fused silica sample containing bubbles was characterized using microcomputed X-ray tomography scans to retrieve the exact locations, diameters, and total volume fraction of bubbles. The predictions of different models using the retrieved data were compared with the normal-hemispherical reflectance and transmittance of the fused silica sample measured experimentally using UV-visible and FTIR spectrophotometers. Overall, the predictions of hybrid model, that predicts the effective scattering coefficient and asymmetry factor using the Lorenz–Mie theory and the effective absorption coefficient as the volume-weighted sum of the bubbles and medium absorption coefficients and solves the radiative transfer equation using the Monte Carlo method, showed excellent agreement with both the predictions by the MCRT method and with experimental measurements. Finally, the hybrid model was used to simulate radiation transfer through seafoams in ship wakes containing microbubbles to predict their albedo and estimate radiative forcing.

The third objective was achieved in Chapter 5. A new method to enhance the emittance of silica-based radiative cooling surfaces was introduced and experimentally validated. The mesoporous aerogel monoliths demonstrated near-unity emissivities within the atmospheric transparency window, achieving significantly greater radiative cooling power than dense silica covers of the same thickness at near room temperature while transmitting more than 95% of solar radiation. These aerogel monoliths could be used atop reflective metal substrates like aluminum or silver for daytime radiative cooling applications. Additionally, these samples could serve independently as transparent covers in applications that require

solar transmission, such as solar cell covers, glazings, and window solutions.

6.2 Future work

6.2.1 Predicting the effect of bubble shape and experimentally validating the effect of bubble contact angle on light absorption during photoelectrochemical water splitting

The simulations presented in Chapter 2 assumed that the bubbles attached to the photoelectrode surface were spherical cap-shaped during photoelectrochemical water splitting. However, during bubble growth from nucleation to departure, the bubble shape may change and deviate from cap-shaped due to surface tension and buoyancy forces. Indeed, bubble shape changes substantially during a growth cycle in photoelectrochemical water splitting, similar to that during nucleate pool boiling [6], as shown in Figure 6.1.

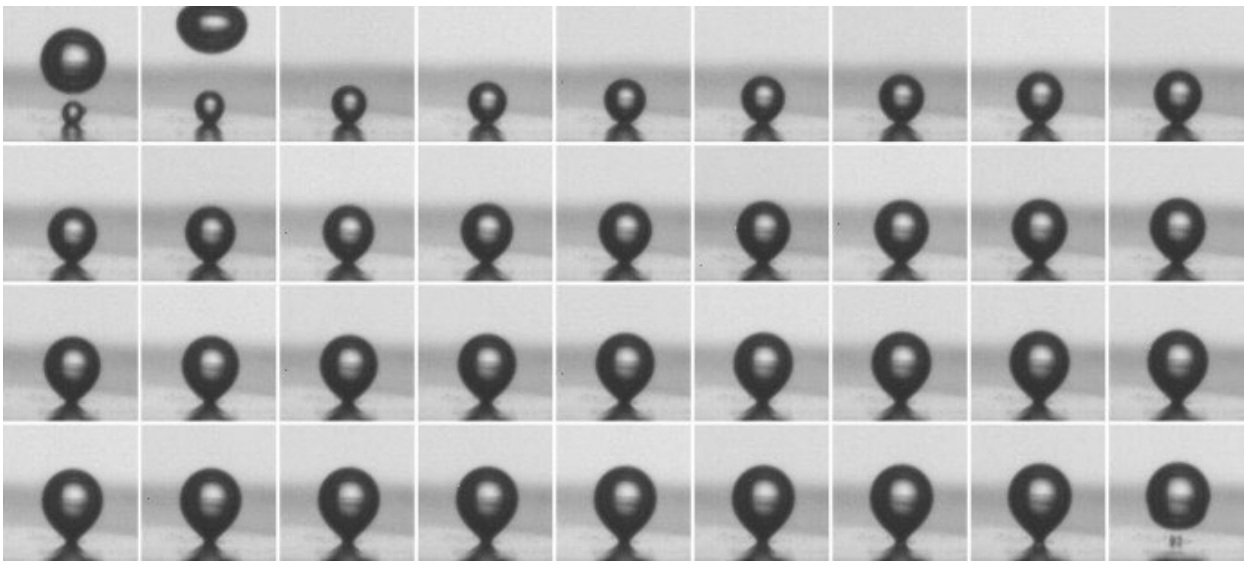

Figure 6.1: Bubble shape during a growth cycle in nucleate pool boiling. (reprinted from Ref. [124], Copyright © 2008 with permission from Elsevier.)

Moreover, in Chapter 2, the effect of bubble contact angle θ_c on the optical losses in a PEC cell was predicted. However, there was no experimental data available in the literature to compare these predictions. Therefore, to fill this gap, experiments should be performed

with different coatings on the photoelectrode surface to vary bubble contact angles and study its effect on light absorption in the photoelectrode.

6.2.2 Assessing the global impact of ocean albedo enhancement in ship wakes using climate model

Chapter 5 established the achievable albedo values using seafoams containing microbubbles, and identified the required bubble diameters, volume fractions, and seafoam thickness. However, to accurately assess the potential of ocean albedo enhancement in global shipping lanes and quantify its global impact, it is important to simulate the climate intervention strategy using an appropriate climate model, while also accounting for the climate's response to it. This could be achieved using the latest Community Earth System Model (CESM2) [125], which is a fully-coupled, global climate model that delivers cutting-edge computer simulations of the Earth's climate across past, present, and future scenarios.

Here, the global maritime traffic density data (in monthly hours/km^2) for cargo ships was obtained from Ref. [126] and analyzed using the open-source geographic information system software QGIS [127]. The data was composed of pixels representing a geographical area of 1 km $\times$ 1 km. The geospatial variation of shipping traffic density was fractionalized by enforcing traffic density of more than 1 monthly hours/km^2 to be 1, while those below 1 were kept unchanged. Then, the albedo for each pixel was calculated by

$$\alpha_p = s\alpha_w + (1 - s)\alpha_o, \tag{6.1}$$

where s is the fraction of shipping traffic density (varying between 0 and 1) corresponding to that pixel, $\alpha_w = 0.9$ is the albedo of seafoam in ship wake, and $\alpha_o = 0.06$ is the albedo of bare ocean surface. Figure 6.2 presents the corresponding geospatial variation in ocean albedo obtained by following the procedure described above. Future work should modify the CESM2 codes to enable using the data plotted in Figure 6.2 as input. Such simulations could help quantify the radiative forcing achieved using ship wake albedo enhancement, and analyze its corresponding effects on local and global climate over the years.

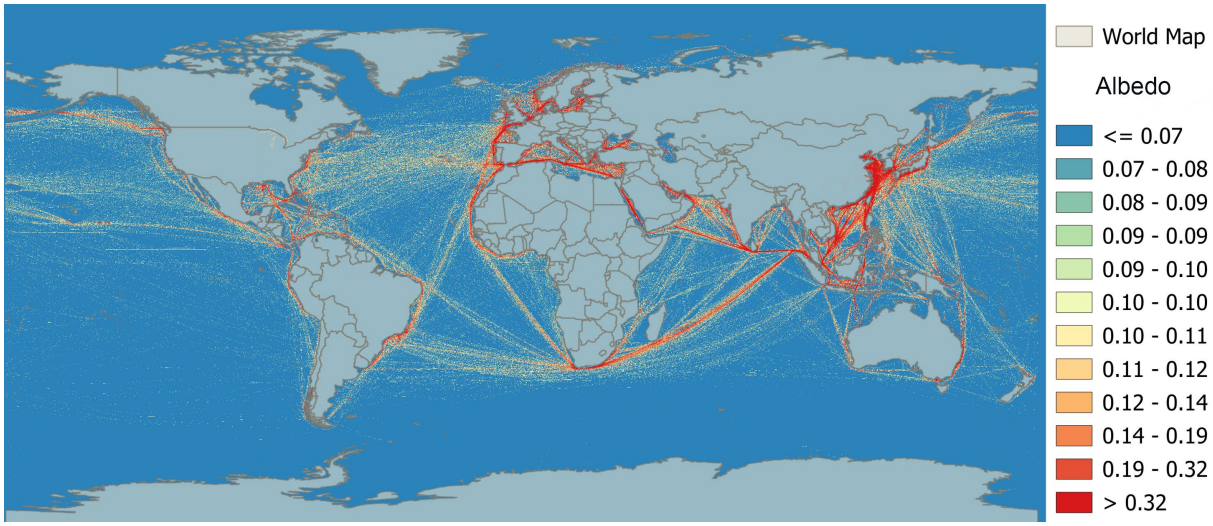

Figure 6.2: Geospatial variation in ocean albedo obtained by transforming shipping traffic density data obtained from Ref. [126] into albedo data using Equation (6.1) using QGIS software [127].

6.2.3 Embedding large silica nanoparticles in silica aerogels for passive daytime radiative cooling

Chapter 6 demonstrated that a mesoporous microstructure eliminated the characteristic reflectance peak of silica, thereby allowing to achieve near-unity emittance in the long wave IR spectrum. However, the silica aerogels exhibited a substantially large transparency to solar radiation, and thus required a metallic substrate as a reflector for daytime radiative cooling applications. Eliminating this need for a reflective substrate could minimize the cost of daytime radiative cooling surfaces, while also minimizing the solar absorption in aerogel. Notably, the porous microstructure in silica aerogels could be leveraged to embed large silica nanoparticles. These particles could substantially scatter solar radiation while also contributing to the emittance in the atmospheric transparency window.

APPENDIX A

Supplementary Materials for Chapter 3

S1. Computational Monte Carlo ray-tracing procedure

i. Generate a random initial position in the x-y plane on top of the computational domain for the normally incident ray.

ii. Determine the next location reached by the ray at either the electrolyte/bubble interface, the electrolyte/photoelectrode interface, or the bubble/photoelectrode interface. If that location was inside the photoelectrode e.g., for rays refracted into surface-attached bubbles (see Figure 2), update it to a location on the photoelectrode surface by retracing the ray while maintaining the same direction.

iii. Calculate the distance l travelled by the ray through the medium from the previous location to the final position.

iv. Generate a random number rd between 0 and 1 following a uniform distribution to calculate a random path length l'_m given by $l'_m = ln(rd/\kappa_{m,\lambda})$ where $\kappa_{m,\lambda} = 4\pi k_{m,\lambda}/\lambda$ is the absorption coefficient of the medium. If $l > l'_m$, count the ray as absorbed in the medium. If $l < l'_m$, calculate the interface reflectance ρ using Fresnel's equations.

v. Again, generate a random number rd between 0 and 1 following a uniform distribution. If $rd < \rho$, then the ray was reflected, else it was refracted. For either case, update the ray direction accordingly using the generalized Snell's law [43].

vi. With this new position and updated direction, trace the ray again in its onward journey to another interface by repeating steps 2-5.

vii. If the ray reached the top surface of the computational domain, count it as reflected. If it was refracted into the photoelectrode through either the bubble/photoelectrode or the electrolyte/photoelectrode interface, count it as absorbed in the photoelectrode.

S2. Validation of MCRT code

Figure A.1 schematically shows the three simulation cases for which the the analytical expressions for the area-averaged photoelectrode absorptance $\bar{A}_\lambda$ were available from Refs. [37, 42]. The three simulation cases are detailed below.

Case I

Here, the refractive and absorption indices of the bubbles were chosen to be the same as that of the electrolyte, equivalent to having a semitransparent electrolyte of thickness H_e = 10 mm covering the photoelectrode without any bubbles, as shown schematically in Figure A.1(a). Thus, the photoelectrode absorptance was given by [37]

$$\bar{A}_{I,\lambda} = (1 - \rho_{ep,\lambda}) e^{-\kappa_{e,\lambda} H_e}, \tag{A.1}$$

where the subscripts I refers to Case I, $\kappa_{e,\lambda} = 4\pi k_{e,\lambda}/\lambda$ and $\rho_{ij,\lambda}$ is the reflectance at the optically smooth interface between media i and j under normal incidence, given by [37]

$$\rho_{ij,\lambda} = \frac{(n_{i,\lambda} - n_{j,\lambda})^2 + (k_{i,\lambda} - k_{j,\lambda})^2}{(n_{i,\lambda} + n_{j,\lambda})^2 + (k_{i,\lambda} + k_{j,\lambda})^2} \tag{A.2}$$

Case II

Here, a gas film of thickness H_b = 1 mm having refrative index same as the bubbles was embedded between the Si photoelectrode and a non-absorbing electrolyte of thickenss H_e = 9 mm, as shown schematically in Figure A.1(b). Here, the photoelectrode absorptance was given by [37]

$$\bar{A}_{II,\lambda} = \frac{(1 - \rho_{eb,\lambda})(1 - \rho_{bp,\lambda})}{1 - \rho_{eb,\lambda}\rho_{bp,\lambda}}, \tag{A.3}$$

where the subscripts e, b, and p respectively represent the electrolyte, the bubble and the photoelectrode and $\rho_{ij,\lambda}$ is given by Eq. A.3.

Case III

Here, a gas film of thickness $H_b = 1$ mm having refrative index same as the bubbles was embedded between two non-absorbing layers of electrolyte, each having thickenss $H = 4.5$ mm, as shown schematically in Figure A.1(c). Here, the photoelectrode absorptance was given by [42]

$$\bar{A}_{III,\lambda} = \frac{(1-\rho_{eb,\lambda})(1-\rho_{be,\lambda})(1-\rho_{ep,\lambda})}{(1-\rho_{eb,\lambda}\rho_{be,\lambda})(1-\rho_{be,\lambda}\rho_{ep,\lambda}) - (1-\rho_{be,\lambda})\rho_{eb,\lambda}\rho_{ep,\lambda}}. \tag{A.4}$$

Here again, the subscripts e, b, and p respectively represent the electrolyte, the bubble and the photoelectrode and $\rho_{ij,\lambda}$ is given by Eq. A.3.

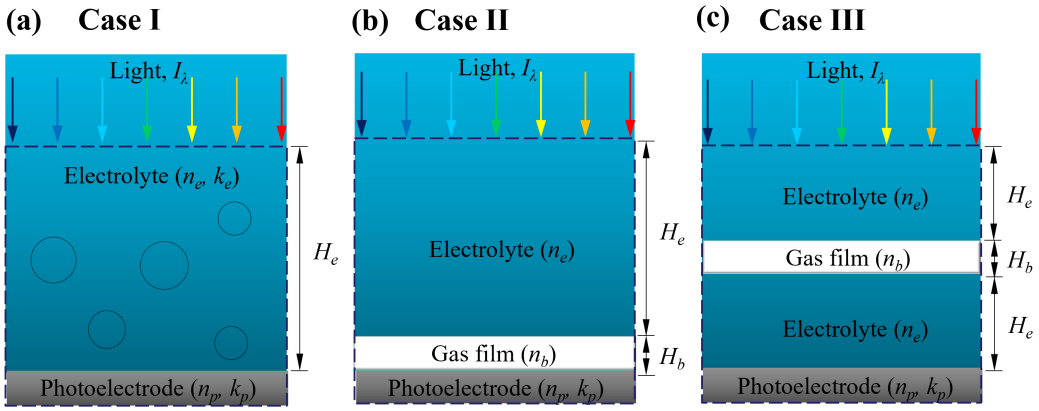

Figure A.1: Schematics for (a) Case I, (b) Case II, and (c) Case III chosen for validating the MCRT code.

Figure A.2(a) plots the area-averaged photoelectrode absorptance $\bar{A}_\lambda$ as a function of wavelength λ of the incident radiation for the three cases considered. It shows excellent agreement between the analytical and numerical predictions for all wavelengths, thus validating that reflection and refraction at the electrolyte/bubble, bubble/photoelectrode, and electrolyte/bubble interfaces, as well as absorption by the electrolyte were accurately accounted for.

Moreover, the area-averaged absorptance of a bubble-covered horizontal Si photoelectrode subjected to normally incident monochromatic radiation of wavelength $\lambda = 630$ nm was predicted and compared with those reported in Ref.[49] assuming no bubbles dispersed in

the transparent electrolyte volume. For these simulations, the bubble plume thickness H and the bubble diameter D were chosen to be 1 mm such that the code computationally generated only a monolayer of bubbles attached to the photoelectrode surface having a contact angle θ_c and projected surface area coverage f_A. The refractive and absorption indices of the photoelectrode were respectively taken as $n_p = 3.88$ and $k_p = 0.016$. The electrolyte and bubbles were non-absorbing with their respective refractive indices taken as $n_e = 1.33$ and $n_b = 1.0$. Figure A.2(b) compares the area-averaged photoelectrode absorptance $\bar{A}$ predicted from our study with that reported in Ref.[49] for different projected surface area coverages f_A for bubble contact angle $\theta_c = 0^\circ$ or 90°. Here also, excellent agreement was observed, validating the accurate prediction of the effect of surface-attached bubbles on light transfer.

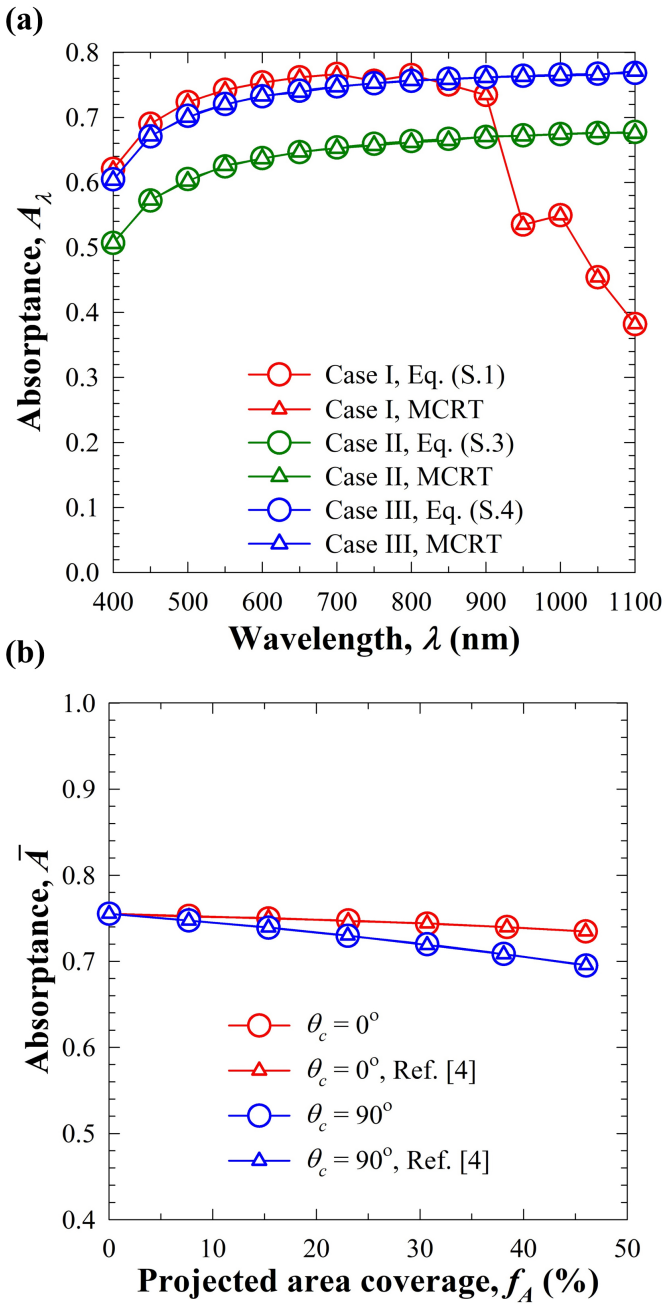

Figure A.2: (a) Comparison of predicted area-averaged photoelectrode absorptance $\bar{A}_\lambda$ with the results from analytical expressions for Cases I, II, and III. (b) Comparison of predicted photoelectrode absorptance with the results reported in Ref.[49] for different projected surface area coverages f_A.

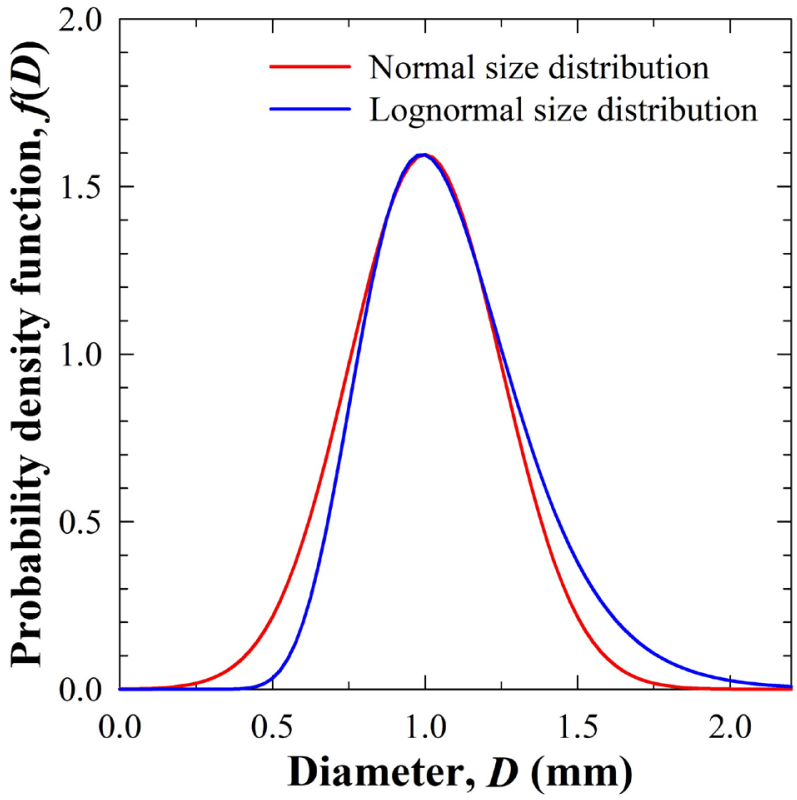

Figure A.3: Comparison of probability density functions for polydisperse bubbles having either normal size distribution with mean diameter $\bar{D} = 1$ mm and standard deviation $\sigma = 0.25$ mm, or lognormal size distribution with mean $\mu = 0.05$ and standard deviation $\chi = 0.25$.

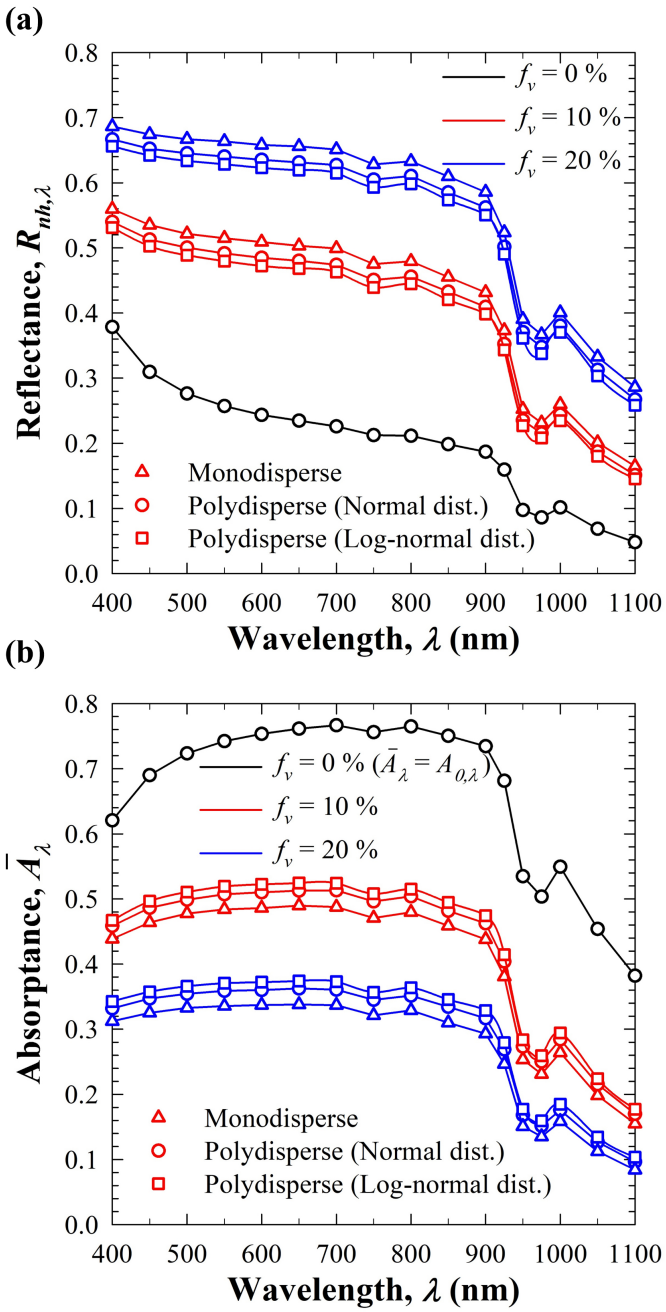

Figure A.4: Comparison of (a) spectral normal-hemispherical reflectance $R_{nh,\lambda}$ and (b) spectral area-averaged photoelectrode absorptance $\bar{A}_\lambda$ for either monodisperse bubbles or polydisperse bubbles with normal or lognormal size distribution for mean bubble diameter of 300 µm and bubble volume fractions f_v of 10% or 20%.

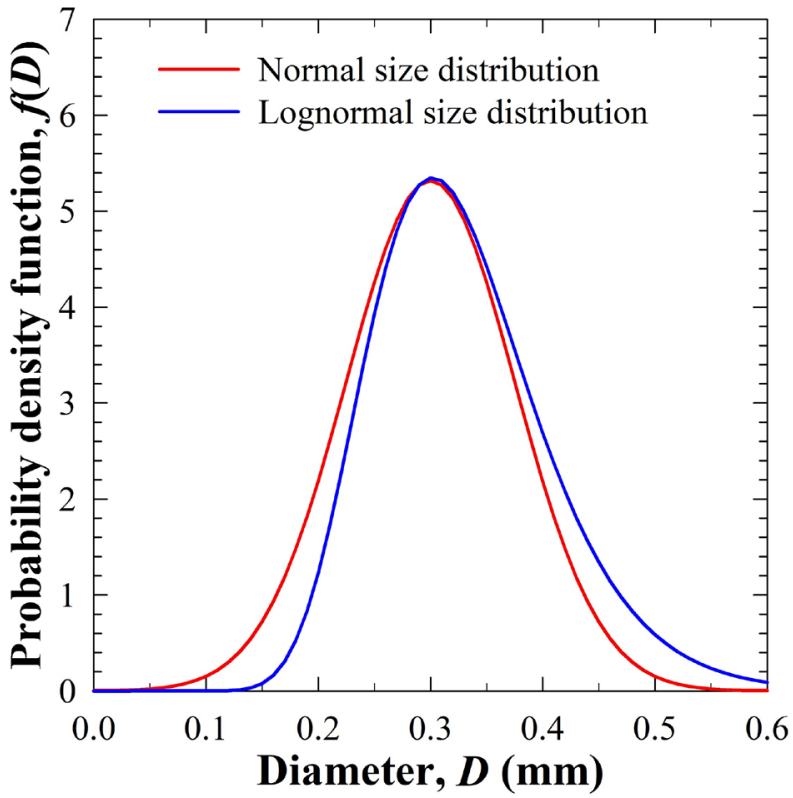

Figure A.5: Comparison of probability density functions for polydisperse bubbles having either normal size distribution with mean diameter $\bar{D}$ = 300 µm and standard deviation σ = 75 µm, or lognormal size distribution with mean μ = -1.14 and standard deviation χ = 0.24.

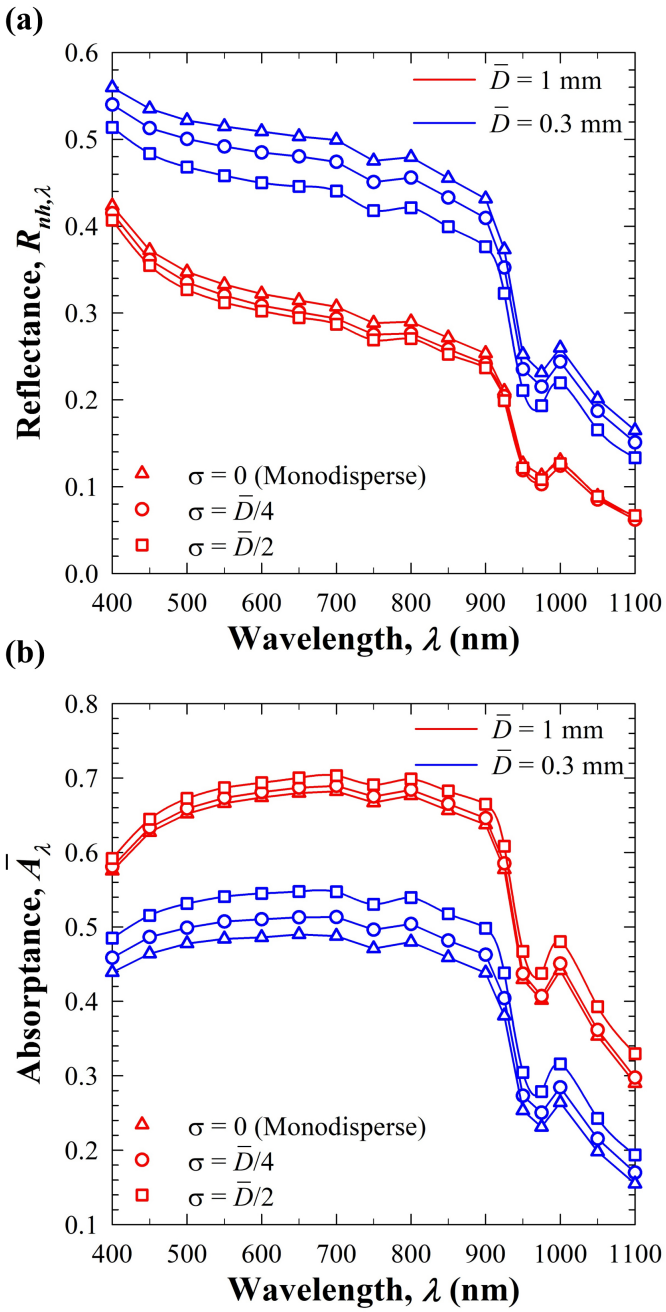

Figure A.6: Comparison of (a) spectral normal-hemispherical reflectance $R_{nh,\lambda}$ and (b) spectral area-averaged photoelectrode absorptance $\bar{A}_\lambda$ for normally distributed polydisperse bubbles having mean bubble diameter $\bar{D} = 0.3$ or 1 mm and different standard deviations $\sigma = 0$, $\bar{D}/4$, or $\bar{D}/2$ for bubble volume fraction $f_v = 10\%$

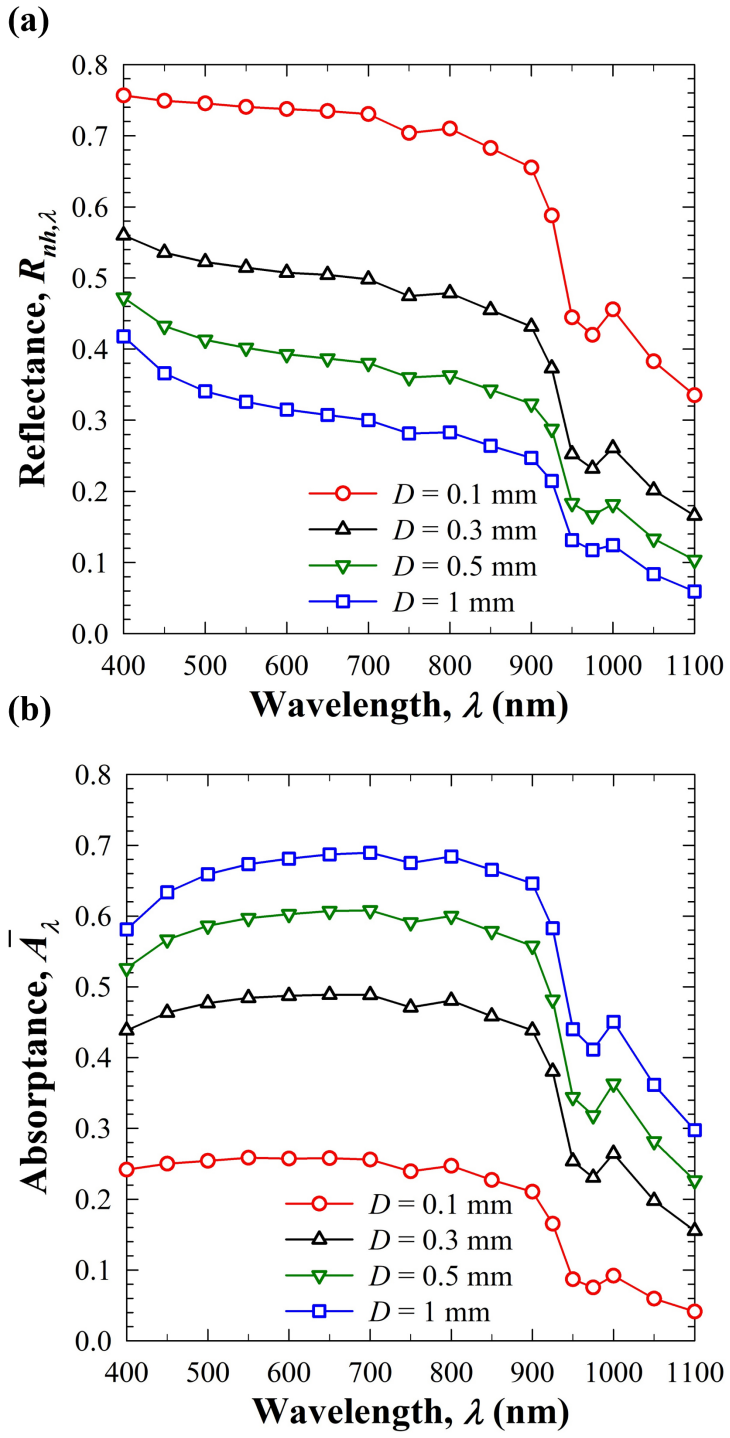

Figure A.7: (a) Normal-hemispherical reflectance $R_{nh,\lambda}$ and (b) area-averaged photoelectrode absorptance $\bar{A}_\lambda$ as functions of wavelength λ for different bubble diameters D for bubble volume fraction $f_v = 10\%$ and bubble plume thickness $H = 10$ mm.

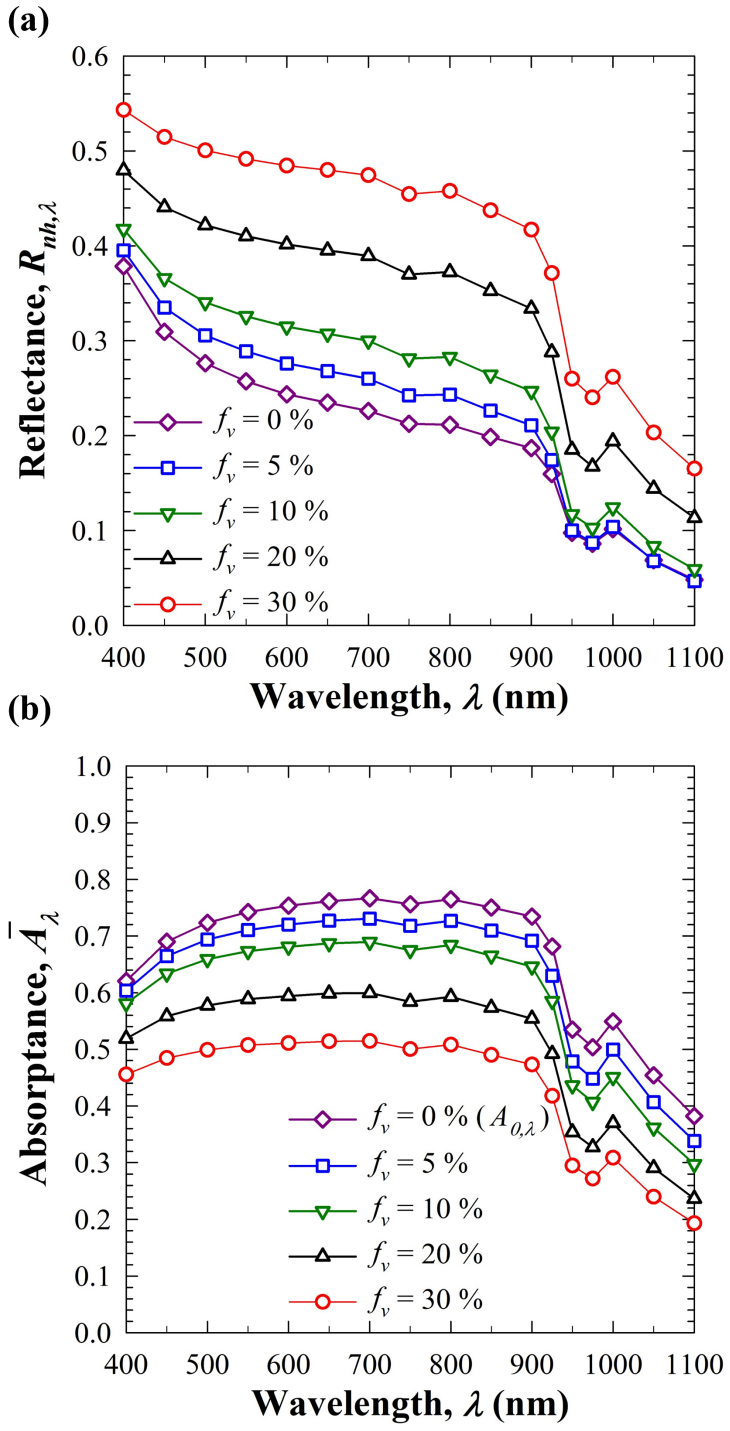

Figure A.8: (a) Normal-hemispherical reflectance $R_{nh,\lambda}$ and (b) area-averaged photoelectrode absorptance $\bar{A}_\lambda$ as functions of wavelength λ for different bubble volume fractions f_v for bubble plume thickness $H = 10$ mm and bubble diameter $D = 1$ mm.

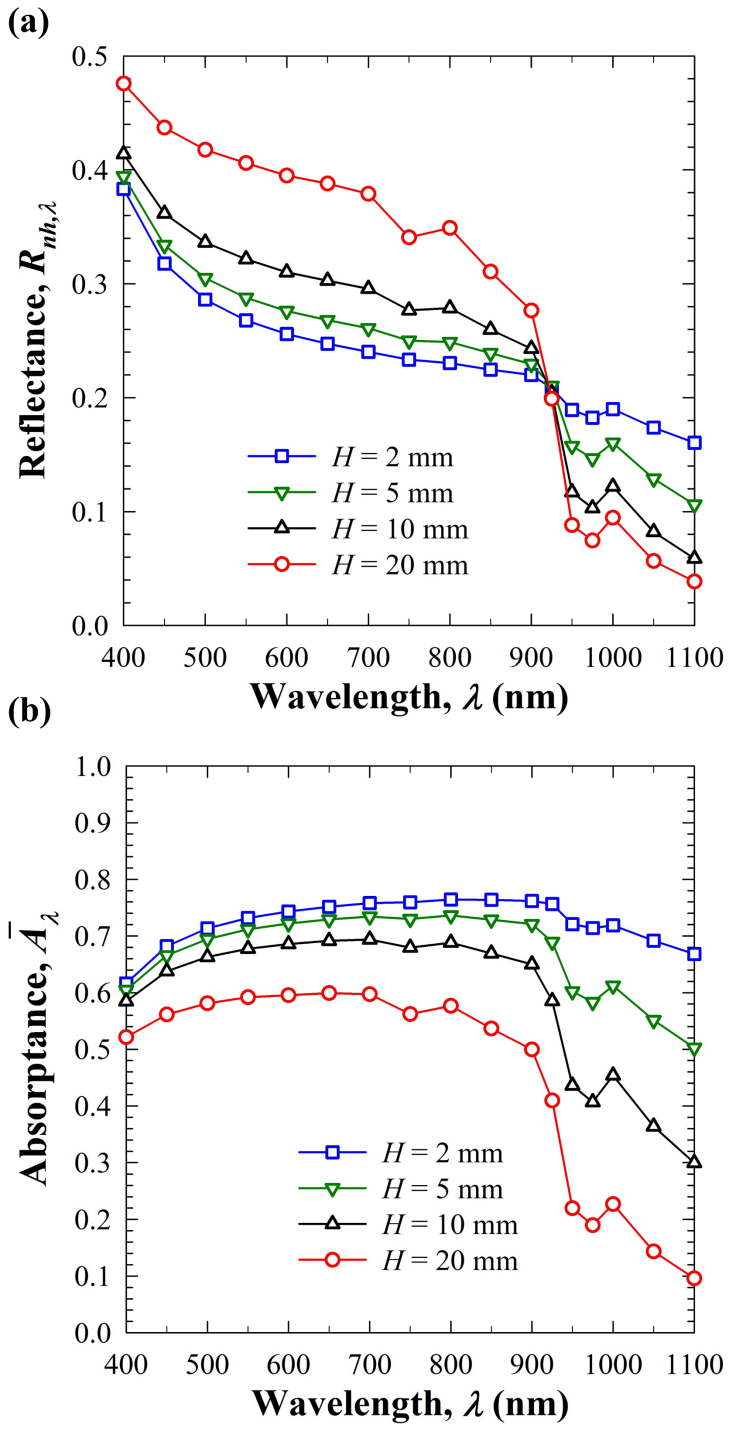

Figure A.9: (a) Normal-hemispherical reflectance $R_{nh,\lambda}$ and (b) area-averaged photoelectrode absorptance $\bar{A}_\lambda$ as functions of wavelength λ for different bubble plume thicknesses H for bubble volume fraction $f_v = 10\%$ and bubble diameter $D = 1$ mm.

References

[1] Nathan S Lewis, "Research opportunities to advance solar energy utilization", *Science*, vol. 351, no. 6271, pp. aad1920, 2016.

[2] Varun Sivaram, *Taming the sun: Innovations to harness solar energy and power the planet*, MIT Press, 2018.

[3] Yu Hou, Ruxandra Vidu, and Pieter Stroeve, "Solar energy storage methods", *Industrial & Engineering Chemistry Research*, vol. 50, no. 15, pp. 8954–8964, 2011.

[4] Peter P Edwards, Vladimir L Kuznetsov, William I F David, and Nigel P Brandon, "Hydrogen and fuel cells: towards a sustainable energy future", *Energy Policy*, vol. 36, no. 12, pp. 4356–4362, 2008.

[5] Reza Soltani, MA Rosen, and Ibrahim Dincer, "Assessment of CO_2 capture options from various points in steam methane reforming for hydrogen production", *International Journal of Hydrogen Energy*, vol. 39, no. 35, pp. 20266–20275, 2014.

[6] Andrea Angulo, Peter van der Linde, Han Gardeniers, Miguel Modestino, and David Fernández Rivas, "Influence of bubbles on the energy conversion efficiency of electrochemical reactors", *Joule*, vol. 4, no. 3, pp. 555–579, 2020.

[7] Jin Hyun Kim, Dharmesh Hansora, Pankaj Sharma, Ji-Wook Jang, and Jae Sung Lee, "Toward practical solar hydrogen production–an artificial photosynthetic leaf-to-farm challenge", *Chemical Society Reviews*, vol. 48, no. 7, pp. 1908–1971, 2019.

[8] Hao Wu, Hui Ling Tan, Cui Ying Toe, Jason Scott, Lianzhou Wang, Rose Amal, and Yun Hau Ng, "Photocatalytic and photoelectrochemical systems: similarities and differences", *Advanced Materials*, vol. 32, no. 18, pp. 1904717, 2020.

[9] Tae Hwa Jeon, Min Seok Koo, Hyejin Kim, and Wonyong Choi, "Dual-functional photocatalytic and photoelectrocatalytic systems for energy-and resource-recovering water treatment", *ACS Catalysis*, vol. 8, no. 12, pp. 11542–11563, 2018.

[10] Brian D James, George N Baum, Julie Perez, and Kevin N Baum, "Technoeconomic analysis of photoelectrochemical (PEC) hydrogen production", *DOE report*, 2009.

[11] Miguel A Modestino, S Mohammad H Hashemi, and Sophia Haussener, "Mass transport aspects of electrochemical solar-hydrogen generation", *Energy & Environmental Science*, vol. 9, no. 5, pp. 1533–1551, 2016.

[12] Anna E Dorfi, Alan C West, and Daniel V Esposito, "Quantifying losses in photoelectrode performance due to single hydrogen bubbles", *The Journal of Physical Chemistry C*, vol. 121, no. 48, pp. 26587–26597, 2017.

[13] Francis Njoka, Shinsuke Mori, Shinichi Ookawara, and Mahmoud Ahmed, "Effects of photo-generated gas bubbles on the performance of tandem photoelectrochemical reactors for hydrogen production", *International Journal of Hydrogen Energy*, vol. 44, no. 21, pp. 10286–10300, 2019.

[14] H Döscher, JF Geisz, TG Deutsch, and JA Turner, "Sunlight absorption in water–efficiency and design implications for photoelectrochemical devices", *Energy & Environmental Science*, vol. 7, no. 9, pp. 2951–2956, 2014.

[15] William Shockley and Hans J Queisser, "Detailed balance limit of efficiency of p-n junction solar cells", *Journal of Applied Physics*, vol. 32, no. 3, pp. 510–519, 1961.

[16] Charles H Henry, "Limiting efficiencies of ideal single and multiple energy gap terrestrial solar cells", *Journal of Applied Physics*, vol. 51, no. 8, pp. 4494–4500, 1980.

[17] Glen P Peters, Robbie M Andrew, Tom Boden, Josep G Canadell, Philippe Ciais, Corinne Le Quéré, Gregg Marland, Michael R Raupach, and Charlie Wilson, "The challenge to keep global warming below 2 °c", *Nature Climate Change*, vol. 3, no. 1, pp. 4–6, 2013.

[18] X. Lan, P. Tans, and K. W. Thoning, "Trends in globally-averaged CO_2 determined from NOAA Global Monitoring Laboratory measurements", 2024.

[19] Greta Magnolia, Marco Gambini, Stefano Mazzoni, and Michela Vellini, "Renewable energy, carbon capture & sequestration and hydrogen solutions as enabling technologies for reduced CO_2 energy transition at a national level: an application to the 2030 Italian national energy scenarios", *Cleaner Energy Systems*, vol. 4, pp. 100049, 2023.

[20] Douglas G MacMartin and Ben Kravitz, "The engineering of climate engineering", *Annual Review of Control, Robotics, and Autonomous Systems*, vol. 2, pp. 445–467, 2019.

[21] Russell Seitz, "Bright water: hydrosols, water conservation and climate change", *Climatic Change*, vol. 105, no. 3-4, pp. 365–381, 2011.

[22] "Wikimedia Commons Images", `https://commons.wikimedia.org/wiki/Category:Images`, Accessed: 2022-12-07.

[23] UNCTAD, *Handbook of Statistics 2023*, 2023, Accessed: January 10, 2024.

[24] Amanda T Nylund, Ida-Maja Hassellöv, Anders Tengberg, Rickard Bensow, Göran Broström, Martin Hassellöv, and Lars Arneborg, "Hydrographical implications of ship-induced turbulence in stratified waters, studied through field observations and cfd modelling", *Frontiers in Marine Science*, vol. 10, 2023.

[25] Julia A Crook, Lawrence S Jackson, and Piers M Forster, "Can increasing albedo of existing ship wakes reduce climate change?", *Journal of Geophysical Research: Atmospheres*, vol. 121, no. 4, pp. 1549–1558, 2016.

[26] IEA, "World Energy Outlook 2022, International Energy Agency (IEA), Paris https://www.iea.org/reports/world-energy-outlook-2022, License: CC BY 4.0 (report); CC BY NC SA 4.0 (Annex A)", 2022.

[27] Dongliang Zhao, Ablimit Aili, Yao Zhai, Shaoyu Xu, Gang Tan, Xiaobo Yin, and Ronggui Yang, "Radiative sky cooling: Fundamental principles, materials, and applications", *Applied Physics Reviews*, vol. 6, no. 2, 2019.

[28] Aaswath P Raman, Marc Abou Anoma, Linxiao Zhu, Eden Rephaeli, and Shanhui Fan, "Passive radiative cooling below ambient air temperature under direct sunlight", *Nature*, vol. 515, no. 7528, pp. 540–544, 2014.

[29] Bin Zhao, Mingke Hu, Xianze Ao, Nuo Chen, and Gang Pei, "Radiative cooling: A review of fundamentals, materials, applications, and prospects", *Applied Energy*, vol. 236, pp. 489–513, 2019.

[30] Qian Zhang, Shuaihao Wang, Xueyang Wang, Yi Jiang, Jinlei Li, Weilin Xu, Bin Zhu, and Jia Zhu, "Recent progress in daytime radiative cooling: Advanced material designs and applications", *Small Methods*, vol. 6, no. 4, pp. 2101379, 2022.

[31] Shanhui Fan and Wei Li, "Photonics and thermodynamics concepts in radiative cooling", *Nature Photonics*, vol. 16, no. 3, pp. 182–190, 2022.

[32] Wei Gao and Yongping Chen, "Emerging materials and strategies for passive daytime radiative cooling", *Small*, vol. 19, no. 18, pp. 2206145, 2023.

[33] Linxiao Zhu, Aaswath Raman, Ken Xingze Wang, Marc Abou Anoma, and Shanhui Fan, "Radiative cooling of solar cells", *Optica*, vol. 1, no. 1, pp. 32–38, 2014.

[34] Elisa Skoplaki and John A Palyvos, "On the temperature dependence of photovoltaic module electrical performance: A review of efficiency/power correlations", *Solar energy*, vol. 83, no. 5, pp. 614–624, 2009.

[35] David H Otth and Ronald G Ross Jr, "Assessing photovoltaic module degradation and lifetime from long term environmental tests", in *Institute of Environmental Sciences, Annual Technical Meeting*, 1983.

[36] Etienne Blandre, Refet Ali Yalçin, Karl Joulain, and Jérémie Drévillon, "Microstructured surfaces for colored and non-colored sky radiative cooling", *Optics Express*, vol. 28, no. 20, pp. 29703–29713, 2020.

[37] Michael F Modest and Sandip Mazumder, *Radiative Heat Transfer*, Academic Press, New York, NY, 4^{th} edition, 2021.

[38] Daniel W Mackowski and Michael I Mishchenko, "A multiple sphere T-matrix Fortran code for use on parallel computer clusters", *Journal of Quantitative Spectroscopy and Radiative Transfer*, vol. 112, no. 13, pp. 2182–2192, 2011.

[39] Dennis M Sullivan, *Electromagnetic simulation using the FDTD method*, John Wiley & Sons, Hoboken, NJ, 2013.

[40] Bruce T Draine and Piotr J Flatau, "Discrete-dipole approximation for scattering calculations", *Journal of Optical Society of America A*, vol. 11, no. 4, pp. 1491–1499, 1994.

[41] Refet Ali Yalcin, Thomas Lee, Glareh Natalie Kashanchi, Johannes Markkanen, Ricardo Martinez, Sarah H Tolbert, and Laurent Pilon, "Dependent scattering in thick and concentrated colloidal suspensions", *ACS Photonics*, vol. 9, no. 10, pp. 3318–3332, 2022.

[42] John R Howell, M Pinar Mengüç, Kyle Daun, and Robert Siegel, *Thermal Radiation Heat Transfer*, 7th ed., CRC Press, Boca Raton, FL, 2020.

[43] Keyong Zhu, Yong Huang, Jeremy Pruvost, Jack Legrand, and Laurent Pilon, "Transmittance of transparent windows with non-absorbing cap-shaped droplets condensed on their backside", *Journal of Quantitative Spectroscopy and Radiative Transfer*, vol. 194, pp. 98–107, 2017.

[44] Keyong Zhu and Laurent Pilon, "Transmittance of semitransparent windows with absorbing cap-shaped droplets condensed on their backside", *Journal of Quantitative Spectroscopy and Radiative Transfer*, vol. 201, pp. 53–63, 2017.

[45] M Abdelrahman, P Fumeaux, and P Suter, "Study of solid-gas-suspensions used for direct absorption of concentrated solar radiation", *Solar Energy*, vol. 22, no. 1, pp. 45–48, 1979.

[46] Fletcher J Miller and Roland W Koenigsdorff, "Thermal modeling of a small-particle solar central receiver", *Journal of Solar Energy Engineering*, vol. 122, no. 1, pp. 23–29, 2000.

[47] Himanshu Tyagi, Patrick Phelan, and Ravi Prasher, "Predicted efficiency of a low-temperature nanofluid-based direct absorption solar collector", *Journal of Solar Energy Engineering*, vol. 131, no. 4, pp. 041004, 2009.

[48] Keyong Zhu, Shaoling Li, and Laurent Pilon, "Light transfer through windows with external condensation", *Journal of Quantitative Spectroscopy and Radiative Transfer*, vol. 208, pp. 164–171, 2018.

[49] Abhinav Bhanawat, Keyong Zhu, and Laurent Pilon, "How do bubbles affect light absorption in photoelectrodes for solar water splitting?", *Sustainable Energy & Fuels*, vol. 6, no. 3, pp. 910–924, 2022.

[50] JC Maxwell Garnett, "XII. Colours in metal glasses and in metallic films", *Philosophical Transactions of the Royal Society of London. Series A, Containing Papers of a Mathematical or Physical Character*, vol. 203, no. 359-371, pp. 385–420, 1904.

[51] Max Born, Emil Wolf, A. B. Bhatia, P. C. Clemmow, D. Gabor, A. R. Stokes, A. M. Taylor, P. A. Wayman, and W. L. Wilcock, *Principles of Optics: Electromagnetic Theory of Propagation, Interference and Diffraction of Light*, Cambridge University Press, Cambridge, UK, 7th edition, 1999.

[52] Isaac Holmes-Gentle, Franky Bedoya-Lora, Faye Alhersh, and Klaus Hellgardt, "Optical losses at gas evolving photoelectrodes: implications for photoelectrochemical water splitting", *The Journal of Physical Chemistry C*, vol. 123, no. 1, pp. 17–28, 2018.

[53] Paul A Kempler, Zachary P Ifkovits, Weilai Yu, Azhar I Carim, and Nathan S Lewis, "Optical and electrochemical effects of H_2 and O_2 bubbles at upward-facing Si photoelectrodes", *Energy & Environmental Science*, vol. 14, no. 1, pp. 414–423, 2021.

[54] Gyoko Nagayama, Sei-Ichi Shi-Iki, and Takaharu Tsuruta, "Effects of nanostructures on surface wettability: a molecular dynamics study", *Nippon Kikai Gakkai Ronbunshu B Hen(Transactions of the Japan Society of Mechanical Engineers Part B)(Japan)*, vol. 19, no. 4, pp. 1084–1091, 2007.

[55] Kazuhito Hashimoto, Hiroshi Irie, and Akira Fujishima, "Tio_2 photocatalysis: a historical overview and future prospects", *Japanese journal of applied physics*, vol. 44, no. 12R, pp. 8269, 2005.

[56] Steven Lubetkin, "Thermal marangoni effects on gas bubbles are generally accompanied by solutal marangoni effects", *Langmuir*, vol. 19, no. 26, pp. 10774–10778, 2003.

[57] Halil Berberoglu, Juan Yin, and Laurent Pilon, "Light transfer in bubble sparged photobioreactors for H_2 production and CO_2 mitigation", *International Journal of Hydrogen Energy*, vol. 32, no. 13, pp. 2273–2285, 2007.

[58] Keisuke Obata and Fatwa Abdi, "Bubble-induced convection stabilizes local pH during solar water splitting in neutral pH electrolytes", *Sustainable Energy & Fuels*, vol. 5, no. 15, pp. 3791–3801, 2021.

[59] Antonio Vilanova, Tania Lopes, Carsten Spenke, Michael Wullenkord, and Adélio Mendes, "Optimized photoelectrochemical tandem cell for solar water splitting", *Energy Storage Materials*, vol. 13, pp. 175–188, 2018.

[60] Oscar Khaselev and John A Turner, "A monolithic photovoltaic-photoelectrochemical device for hydrogen production via water splitting", *Science*, vol. 280, no. 5362, pp. 425–427, 1998.

[61] Shyam S Kocha, Don Montgomery, Mark W Peterson, and John A Turner, "Photoelectrochemical decomposition of water utilizing monolithic tandem cells", *Solar energy materials and solar cells*, vol. 52, no. 3-4, pp. 389–397, 1998.

[62] Wen-Hui Cheng, Matthias H Richter, Matthias M May, Jens Ohlmann, David Lackner, Frank Dimroth, Thomas Hannappel, Harry A Atwater, and Hans-Joachim Lewerenz, "Monolithic photoelectrochemical device for direct water splitting with 19% efficiency", *ACS Energy Letters*, vol. 3, no. 8, pp. 1795–1800, 2018.

[63] Brian Seger, Thomas Pedersen, Anders B Laursen, Peter CK Vesborg, Ole Hansen, and Ib Chorkendorff, "Using TiO_2 as a conductive protective layer for photocathodic H_2

evolution", *Journal of the American Chemical Society*, vol. 135, no. 3, pp. 1057–1064, 2013.

[64] Xiaowei Hu, Zhenshan Cao, Yechun Wang, Shaohua Shen, Liejin Guo, and Juanwen Chen, "Single photogenerated bubble at gas-evolving TiO_2 nanorod-array electrode", *Electrochimica Acta*, vol. 202, pp. 175–185, 2016.

[65] George M Hale and Marvin R Querry, "Optical constants of water in the 200-nm to 200-μm wavelength region", *Applied Optics*, vol. 12, no. 3, pp. 555–563, 1973.

[66] Martin A Green, "Self-consistent optical parameters of intrinsic silicon at 300 K including temperature coefficients", *Solar Energy Materials and Solar Cells*, vol. 92, no. 11, pp. 1305–1310, 2008.

[67] Van P Carey, *Liquid-Vapor Phase-Change Phenomena*, 3rd ed., CRC Press, Boca Raton, FL, 2020.

[68] Hen Dotan, Nripan Mathews, Takashi Hisatomi, Michael Grätzel, and Avner Rothschild, "On the solar to hydrogen conversion efficiency of photoelectrodes for water splitting", *The Journal of Physical Chemistry Letters*, vol. 5, no. 19, pp. 3330–3334, 2014.

[69] Wooseok Yang, Rajiv Ramanujam Prabhakar, Jeiwan Tan, S David Tilley, and Jooho Moon, "Strategies for enhancing the photocurrent, photovoltage, and stability of photoelectrodes for photoelectrochemical water splitting", *Chemical Society Reviews*, vol. 48, no. 19, pp. 4979–5015, 2019.

[70] Isaac Holmes-Gentle and Klaus Hellgardt, "A versatile open-source analysis of the limiting efficiency of photo electrochemical water-splitting", *Scientific Reports*, vol. 8, no. 1, pp. 1–9, 2018.

[71] Khurshid Ali, Anwar Ali Shah, Salma Bilal, and Azhar Ali Shah, "Surface tensions and thermodynamic parameters of surface formation of aqueous salt solutions: III. Aqueous solution of KCl, KBr and KI", *Colloids and Surfaces A: Physicochemical and Engineering Aspects*, vol. 337, no. 1, pp. 194–199, 2009.

[72] Masoud Sadeghi, Vahid Taghikhani, and Cyrus Ghotbi, "Measurement and correlation of surface tension for single aqueous electrolyte solutions", *International Journal of Thermophysics*, vol. 31, no. 4, pp. 852–859, 2010.

[73] Hiroshi Nishiyama, Taro Yamada, Mamiko Nakabayashi, Yoshiki Maehara, Masaharu Yamaguchi, Yasuko Kuromiya, Yoshie Nagatsuma, Hiromasa Tokudome, Seiji Akiyama, Tomoaki Watanabe, et al., "Photocatalytic solar hydrogen production from water on a 100-m^2 scale", *Nature*, vol. 598, no. 7880, pp. 304–307, 2021.

[74] Laurent Pilon and Raymond Viskanta, "Radiation characteristics of glass containing gas bubbles", *Journal of the American Ceramic Society*, vol. 86, no. 8, pp. 1313–1320, 2003.

[75] LA Dombrovsky, "The propagation of infrared radiation in a semitransparent liquid containing gas bubbles", *High Temperature*, vol. 42, no. 1, pp. 133–139, 2004.

[76] JRG Evans, EPJ Stride, MJ Edirisinghe, DJ Andrews, and RR Simons, "Can oceanic foams limit global warming?", *Climate Research*, vol. 42, no. 2, pp. 155–160, 2010.

[77] Alex Aziz, Helen C Hailes, John M Ward, and Julian RG Evans, "Long-term stabilization of reflective foams in sea water", *RSC Advances*, vol. 4, no. 95, pp. 53028–53036, 2014.

[78] Ben Kravitz, Philip J. Rasch, Hailong Wang, Alan Robock, Corey Gabriel, Olivier Boucher, Jason N. S. Cole, James Haywood, Duoying Ji, Andy Jones, Andrew Lenton, John C. Moore, Helene Muri, Ulrike Niemeier, Steven Phipps, Hauke Schmidt, Shingo Watanabe, Shuting Yang, and Jin-Ho Yoon, "The climate effects of increasing ocean albedo: an idealized representation of solar geoengineering", *Atmospheric Chemistry and Physics*, vol. 18, no. 17, pp. 13097–13113, 2018.

[79] Leonid A Dombrovsky and Alexander A Kokhanovsky, "Solar heating of ice sheets containing gas bubbles", *Journal of Quantitative Spectroscopy and Radiative Transfer*, vol. 250, pp. 106991, 2020.

[80] Abhinav Bhanawat and Laurent Pilon, "Light transfer through bubble-filled electrolyte for solar water splitting", *Sustainable Energy & Fuels*, vol. 7, no. 2, pp. 448–460, 2023.

[81] R Viskanta and M P Mengüç, "Radiative transfer in dispersed media", *Applied Mechanics Reviews*, vol. 42, no. 9, pp. 241–259, 1989.

[82] R Viskanta, "Review of three-dimensional mathematical modeling of glass melting", *Journal of Non-Crystalline Solids*, vol. 177, pp. 347–362, 1994.

[83] Andrei G Fedorov and Laurent Pilon, "Glass foams: formation, transport properties, and heat, mass, and radiation transfer", *Journal of Non-Crystalline Solids*, vol. 311, no. 2, pp. 154–173, 2002.

[84] Qian Wang and Kazunari Domen, "Particulate photocatalysts for light-driven water splitting: mechanisms, challenges, and design strategies", *Chemical Reviews*, vol. 120, no. 2, pp. 919–985, 2019.

[85] "What Is "Bubble" Glass?", `https://glassdesigns.com/what-is-bubble-glass/`, Accessed: 2022-12-07.

[86] Abhinav Bhanawat, Refet Ali Yalcin, Ricardo Martinez, and Laurent Pilon, "Critical review and experimental validation of radiative transfer models for semitransparent media containing large gas bubbles", *Journal of Quantitative Spectroscopy and Radiative Transfer*, vol. 311, pp. 108781, 2023.

[87] Tiphaine Galy, Daniel Huang, and Laurent Pilon, "Revisiting independent versus dependent scattering regimes in suspensions or aggregates of spherical particles", *Journal of Quantitative Spectroscopy and Radiative Transfer*, vol. 246, pp. 106924, 2020.

[88] WC Mundy, JA Roux, and AM Smith, "Mie scattering by spheres in an absorbing medium", *Journal of the Optical Society of America*, vol. 64, no. 12, pp. 1593–1597, 1974.

[89] Petr Chylek, "Light scattering by small particles in an absorbing medium", *Journal of the Optical Society of America*, vol. 67, no. 4, pp. 561–563, 1977.

[90] I Wayan Sudiarta and Petr Chylek, "Mie scattering efficiency of a large spherical particle embedded in an absorbing medium", *Journal of Quantitative Spectroscopy and Radiative Transfer*, vol. 70, no. 4-6, pp. 709–714, 2001.

[91] Qiang Fu and Wenbo Sun, "Mie theory for light scattering by a spherical particle in an absorbing medium", *Applied Optics*, vol. 40, no. 9, pp. 1354–1361, 2001.

[92] Wenbo Sun, Norman G Loeb, and Qiang Fu, "Light scattering by coated sphere immersed in absorbing medium: a comparison between the FDTD and analytic solutions", *Journal of Quantitative Spectroscopy and Radiative Transfer*, vol. 83, no. 3-4, pp. 483–492, 2004.

[93] AG Fedorov and R Viskanta, "Radiative transfer in a semitransparent glass foam blanket", *Physics and Chemistry of Glasses*, vol. 41, no. 3, pp. 127–135, 2000.

[94] Andrei G Fedorov and Raymond Viskanta, "Radiation characteristics of glass foams", *Journal of the American Ceramic Society*, vol. 83, no. 11, pp. 2769–2776, 2000.

[95] Leonid Dombrovsky, Jaona Randrianalisoa, Dominique Baillis, and Laurent Pilon, "Use of Mie theory to analyze experimental data to identify infrared properties of fused quartz containing bubbles", *Applied Optics*, vol. 44, no. 33, pp. 7021–7031, 2005.

[96] Leonid Dombrovsky and Dominique Baillis, *Thermal Radiation in Disperse Systems: An Engineering Approach*, Begell House, New York, NY, 2010.

[97] Ping Yang, Bo-Cai Gao, Warren J. Wiscombe, Michael I. Mishchenko, Steven E. Platnick, Hung-Lung Huang, Bryan A. Baum, Yong X. Hu, Dave M. Winker, Si-Chee Tsay, and Seon K. Park, "Inherent and apparent scattering properties of coated or uncoated spheres embedded in an absorbing host medium", *Applied Optics*, vol. 41, no. 15, pp. 2740–2759, 2002.

[98] Lei Wu, Hongru Yang, Xudong Li, Bin Yang, and Gaoping Li, "Scattering by large bubbles: Comparisons between geometrical-optics theory and debye series", *Journal of Quantitative Spectroscopy and Radiative Transfer*, vol. 108, no. 1, pp. 54–64, 2007.

[99] Hendrik C Van de Hulst, *Light Scattering by Small Particles*, Dover Publications, Mineola, NY, 1981.

[100] S E Orchard, "Reflection and transmission of light by diffusing suspensions", *Journal of the Optical Society of America*, vol. 59, no. 12, pp. 1584–1597, 1969.

[101] W G Egan and T W Hilgeman, *Optical Properties of Inhomogeneous Materials: Applications to Geology, Astronomy, Chemistry and Engineering*, Academic Press, New York, NY, 1979.

[102] B Davison and JB Sykes, *Neutron Transport Theory*, Oxford University Press, London, 1957.

[103] Bruce HJ McKellar and Michael A Box, "The scaling group of the radiative transfer equation", *Journal of Atmospheric Sciences*, vol. 38, no. 5, pp. 1063–1068, 1981.

[104] N Etherden, Tuquabo Tesfamichael, GA Niklasson, and Ewa Wäckelgård, "A theoretical feasibility study of pigments for thickness-sensitive spectrally selective paints", *Journal of Physics D: Applied Physics*, vol. 37, no. 7, pp. 1115, 2004.

[105] Refet Ali Yalçın, Etienne Blandre, Karl Joulain, and Jérémie Drévillon, "Colored radiative cooling coatings with nanoparticles", *ACS Photonics*, vol. 7, no. 5, pp. 1312–1322, 2020.

[106] Refet Ali Yalçın, "Monte Carlo Mie scattering code", `https://github.com/refetaliyalcin/monte-carlo-mie-scattering`, 2020, [Online; accessed 18-January-2022].

[107] Dominique Baillis, Laurent Pilon, Harifidy Randrianalisoa, Rafael Gomez, and Raymond Viskanta, "Measurements of radiation characteristics of fused quartz containing bubbles", *Journal of the Optical Society of America A*, vol. 21, no. 1, pp. 149–159, 2004.

[108] Rei Kitamura, Laurent Pilon, and Miroslaw Jonasz, "Optical constants of silica glass from extreme ultraviolet to far infrared at near room temperature", *Applied Optics*, vol. 46, no. 33, pp. 8118–8133, 2007.

[109] Ian H Malitson, "Interspecimen comparison of the refractive index of fused silica", *Journal of the Optical Society of America*, vol. 55, no. 10, pp. 1205–1209, 1965.

[110] Andreas Markus Loening and Sanjiv Sam Gambhir, "AMIDE: a free software tool for multimodality medical image analysis", *Molecular Imaging*, vol. 2, no. 3, pp. 15353500200303133, 2003.

[111] National Oceanic and Atmospheric Administration (NOAA), "NOAA Solar Calculator", 2024, Accessed: 2024-02-22.

[112] Stephen A Montzka, "The NOAA annual greenhouse gas index (aggi)", *NOAA Global Monitoring Laboratory GML*, 2022.

[113] Javier Arrés Chillón, Bruno Paulillo, Prantik Mazumder, and Valerio Pruneri, "Transparent glass surfaces with silica nanopillars for radiative cooling", *ACS Applied Nano Materials*, vol. 5, no. 12, pp. 17606–17612, 2022.

[114] Evelijn Akerboom, Tom Veeken, Christoph Hecker, Jorik Van De Groep, and Albert Polman, "Passive radiative cooling of silicon solar modules with photonic silica microcylinders", *ACS Photonics*, vol. 9, no. 12, pp. 3831–3840, 2022.

[115] Nir Dahan, Avi Niv, Gabriel Biener, Vladimir Kleiner, and Erez Hasman, "Space-variant polarization manipulation of a thermal emission by a SiO_2 subwavelength grating supporting surface phonon-polaritons", *Applied Physics Letters*, vol. 86, no. 19, 2005.

[116] Juliana Jaramillo-Fernandez, Guy L Whitworth, Jose Angel Pariente, Alvaro Blanco, Pedro D Garcia, Cefe Lopez, and Clivia M Sotomayor-Torres, "A self-assembled 2D thermofunctional material for radiative cooling", *Small*, vol. 15, no. 52, pp. 1905290, 2019.

[117] Danielle M Butts, Patricia E McNeil, Michal Marszewski, Esther Lan, Tiphaine Galy, Man Li, Joon Sang Kang, David Ashby, Sophia King, Sarah H Tolbert, Yongjie Hu, Laurent Pilon, and Bruce S. Dunn, "Engineering mesoporous silica for superior optical and thermal properties", *MRS Energy & Sustainability*, vol. 7, 2020.

[118] Theodore L Bergman, Adrienne S Lavine, Frank P Incropera, and David P DeWitt, *Introduction to Heat Transfer*, John Wiley & Sons, Hoboken, NJ, 6$^{\text{th}}$ edition, 2011.

[119] Theodore L Bergman, Adrienne S Lavine, Frank P Incropera, and David P DeWitt, *Fundamentals of Heat and Mass Transfer*, John Wiley & Sons, Hoboken, NJ, 7$^{\text{th}}$ edition, 2011.

[120] Xingshu Sun, Yubo Sun, Zhiguang Zhou, Muhammad Ashraful Alam, and Peter Bermel, "Radiative sky cooling: fundamental physics, materials, structures, and applications", *Nanophotonics*, vol. 6, no. 5, pp. 997–1015, 2017.

[121] "Gemini Obervatory IR Transmission Spectra", `https://www.gemini.edu/observing/telescopes-and-sites/sites#Transmission`, Accessed: 2023-09-05.

[122] Refet Ali Yalçın, Etienne Blandre, Karl Joulain, and Jérémie Drévillon, "Daytime radiative cooling with silica fiber network", *Solar Energy Materials and Solar Cells*, vol. 206, pp. 110320, 2020.

[123] Zhifeng Huang and Xiulin Ruan, "Nanoparticle embedded double-layer coating for daytime radiative cooling", *International Journal of Heat and Mass Transfer*, vol. 104, pp. 890–896, 2017.

[124] S Siedel, S Cioulachtjian, and J Bonjour, "Experimental analysis of bubble growth, departure and interactions during pool boiling on artificial nucleation sites", *Experimental Thermal and Fluid Science*, vol. 32, no. 8, pp. 1504–1511, 2008.

[125] Gokhan Danabasoglu, J-F Lamarque, J Bacmeister, DA Bailey, AK DuVivier, Jim Edwards, LK Emmons, John Fasullo, R Garcia, Andrew Gettelman, et al., "The community earth system model version 2 (CESM2)", *Journal of Advances in Modeling Earth Systems*, vol. 12, no. 2, pp. e2019MS001916, 2020.

[126] "Global Maritime Traffic maintained by MapLarge (funded by NGA)", https://globalmaritimetraffic.org/, Accessed: 2024-01-15.

[127] QGIS Development Team, "QGIS Geographic Information System", https://www.qgis.org, 2024, Accessed: 2024-02-02.